Thermal Modelling of Oblique Cutting Process

by

Coşkun İSLAM

A Thesis Submitted to the

Graduate School of Sciences and Engineering

in Partial Fulfilment of the Requirements for

The Degree of

Master of Science

in

Mechanical Engineering

Koc University

July 2011

Koç University

Graduate School of Sciences and Engineering

This is to certify that I have examined this copy of a master's thesis by

Coşkun İSLAM

and have found that it is complete and satisfactory in all respects,

and that any and all revisions required by the final

examining committee have been made.

Committee Members:

_____

İsmail Lazoğlu, Ph.D. (Advisor)

_____

Demircan Canadinc, Ph.D.

_____

Mustafa Bakkal, Ph.D.

Date: _____

Abstract

Machining processes such as turning, milling, drilling, grinding etc. are the most widespread processes for producing final shapes of the discrete parts. In today's competitive manufacturing environment, increasing productivity without sacrificing from part quality is an obligation. Considering machining from this point of view, physics based modelling of machining process and optimization of process parameters gain importance.

The aim of this thesis is to develop a novel temperature prediction model that is applicable to oblique cutting processes in variable cutting conditions. Thesis consists of two main parts. In first part mechanics of oblique cutting and mechanics of turning process is presented. Orthogonal to oblique transformation procedure is used in mechanical analysis. Mechanical and geometric outputs of first part are utilized in thermal model as simulation inputs. In second part of the thesis, thermal modelling approach is introduced. A finite difference method based approach is followed in modelling of cutting temperatures. Oblique cutting process model is applied to prediction of turning temperatures by splitting turning geometry in to oblique cutting segments. This block by block modelling approach allows representing a complex problem with simpler subparts. Then, tool, chip and workpiece temperatures are calculated.

Predicted temperature values are validated by using the data available in literature. Simulation results showed that average temperatures on rake face are in acceptable agreement with experimental results. Proposed solution method can be utilized in selecting optimum processing parameters, tool geometry and tool material in order to avoid excessive tool temperatures.

Özet

Talaşlı imalat (tornalama, frezeleme, taşlama ve delme vb.) en son parça geometrilerinin oluşturulmasında en yaygın olarak kullanılan üretim tekniğidir. Parça kalitesinden ödün vermeyecek şekilde birim zamanda üretilen ürün adedinin ve üretim sürecinin veriminin arttırılması günümüzün rekabetçi üretim koşullarında bir gereklilik haline gelmiştir. Talaşlı imalat bir üretim süreci olarak bu bağlamda ele alındığında, fizik temelli süreç modelleme ve talaşlı imalat parametrelerinin eniyilenmesi meseleleri oludkça önemli hale gelmiştir.

Yapılan yüksek lisans tez çalışmasında, oblik metal kesme süreci için yeni bir sıcaklık modelleme yaklaşımının geliştirilmesi amaçlanmıştır. Geliştirilen model değişik kesme koşulları, kesici takım geometrilerine uygulanabilmektedir. Tez çalışması iki temel kısımdan oluşmaktadır. İlk kısımda oblik kesme ve tornalama mekaniği ele alınmıştır. Bu kısımdaki mekanik analizlerde ortogonal kesme mekaniğini oblik kesme mekaniğine dönüştürme yaklaşımı kullanılmıştır. İlk kısımın çıktıları sıcaklık anazlilerinin yapılması için gereken mekanik ve geometrik bilgileri sağlamıştır. İkinci kısımda, sıcaklık analizleri anlatılmıştır. Sıcaklık hesaplamaları sonlu fark yöntemi kullanılarak yapılmıştır. Ayrıca bu kısımda, geliştirilmiş olan oblik metal kesme sıcaklık modelinin tornalama işlemine uygulanması anlatılmıştır. Torna kesme geometrisi bir çok basit oblik kesme geometrisine bölünerek takım, talaş ve parça için hesaplamalar yapılmışıtır.

Hesaplama sonuçları literatürdeki deneysel verilerle doğrulanmış ve sonuçlar deneysel verilerle kabul edilebilir miktarda örtüşmüştür. Geliştirilmiş yaklaşım metal kesmedeki yüksek sıcaklıkları önlemek için eniyi keseme parametrelerinin, takım geometrisinin ve malzemesinin seçilmesi sürecinde kullanılabilecek bir araçtır.

Acknowledgements

Firstly, I would like to express my gratitude to my supervisor Assoc. Prof. Dr. İsmail Lazoğlu for, his guidance, insight, encouragement and patience throughout my time in Koç University. I am also grateful to him for giving me this opportunity.

I also would like to thank Assist. Prof. Dr. Demircan Canadinç and Assist. Prof. Dr. Mustafa Bakkal for involving in my thesis committee and for review of the thesis.

I am thankful to The Scientific and Technological Research Council of Turkey (TÜBİTAK) for supporting me with National Scholarship Program for M.Sc. Studies (Program no: BİDEB 2210).

I deeply appreciate my friends at Manufacturing and Automation Research Center (MARC); Fatih Şenbabaoğlu, Enis Akgün, Hasan Sinan Bank, Yaman Boz, Daulet Izbassarov, Abdullah Can Altunlu, Emre Ayaroğlu, Deniz Erbulut, Onur Demir, Emre Bıyıklı, Özgün Günay, for all the things and time we shared together.

I would like to thank Mechanical Engineering Department of Koç University and Koç University Manufacturing and Automation Research Center (MARC) for the provided infrastructure throughout my study.

I am thankful to Manufacturing Automation Laboratory at University of British Columbia for providing the AISI 4140 orthogonal cutting database.

Last but not the least; I am grateful to my mother Hatice, my father Hasan and my brother Emre for their endless love, support and encouragement.

Table of Contents

List of Tables

List of Figures

Nomenclature

η_c : Chip flow angle (rad)

α_n : Normal rake angle (rad)

b : Width of cut (mm)

h : Depth of cut (mm)

λ_s : Inclination angle (rad)

ϕ_i: Shearing direction angle (rad)

ϕ_n: Normal shear angle (rad)

θ_n: Resultant cutting force orientation angle with respect to cut surface (rad)

θ_i: Resultant cutting force orientation angle with respect to cutting edge normal plane (rad)

β_a: Friction angle (rad)

μ : Friction coefficient

V: Cutting velocity (m/s)

V_n: Velocity component normal to shear plane (m/s)

V_c: Chip flow velocity (m/s)

V_s: Shear velocity (m/s)

τ_s: Average shear flow stress (N/mm^2)

A_s: Shear plane area (mm^2)

$\overrightarrow{F_R}$: Resultant cutting force (N)

$\overrightarrow{F_s}$: Shear force (N)

$\overrightarrow{F_n}$: Shear normal force (N)

$\overrightarrow{F_u}$: Friction force (N)

$\overrightarrow{F_v}$: Normal friction force (N)

K_{tc}: Tangential cutting force coefficient (N/mm^2)

K_{fc}: Feed cutting force coefficient (N/mm^2)

K_{rc}: Radial cutting force coefficient (N/mm^2)

K_{te}: Tangential edge force coefficient (N/mm)

K_{fe}: Feed edge force coefficient (N/mm)

K_{re}: Radial edge force coefficient (N/mm)

$\overrightarrow{F_{tc}}$: Tangential cutting force (N)

$\overrightarrow{F_{fc}}$: Feed cutting force (N)

$\overrightarrow{F_{rc}}$: Radial cutting force (N)

$\overrightarrow{F_{te}}$: Tangential edge force (N)

$\overrightarrow{F_{fe}}$: Feed edge force (N)

$\overrightarrow{F_{re}}$: Radial edge force (N)

$P_{cutting}$: Cutting power (W)

$P'_{cutting}$: Dimensionless cutting power

P_{shear}: Shearing power (W)

$P_{friction}$: Friction power (W)

$l_{contact}$: Tool chip contact length (mm)

α_f: Side rake angle (rad)

α_p: Back rake angle (rad)

a : Radial depth of cut (mm)

c : feed rate (mm/rev)

r : Nose radius of the tool (mm)

ξ_r: Angle between main cutting edge and differential cutting edge measured on P_r (rad)

ξ_c: Angle between main cutting edge and differential cutting edge measured on rake face (rad)

η_{global}: Global chip flow direction (rad)

T_c: Chip temperature array (K)

A: Square coefficient matrix for chip heat balance equations

C: Heat generation array for chip heat balance equations

T_t: Tool temperature array (K)

D: Square coefficient matrix for tool heat balance equations

E: Heat generation array for tool heat balance equations

T_w: Workpiece temperature array (K)

R: Square coefficient matrix for workpiece heat balance equations

S: Heat generation array for workpiece heat balance equations

k_{tool}: Tool thermal conductivity (W/m.K)

k_{chip}: Chip thermal conductivity (W/m.K)

$A_{contact}$: Tool chip contact area (m^2)

α : Thermal diffusivity (m^2/s)

Chapter 1: Introduction

Machining processes such as turning, milling, drilling, grinding etc. are the most widespread processes for producing final shapes of the discrete parts. In today's competitive manufacturing environment, increasing productivity without sacrificing from part quality is a requirement. In machining, increasing material removal rates is one of the common ways for improving productivity. High material removal rates are achieved through increasing cutting speed, depth of cut and feed rates. However, increasing material removal rates results in high cutting temperatures which affects tool life and part surface integrity. Therefore, physics based modelling of metal cutting temperatures and optimization of process variables comes into prominence. Since it avoids costly trial and error procedures, predictive modelling of metal cutting temperatures is a more efficient way of process optimization compared to trial and error.

The aim of this thesis is to develop a novel temperature prediction model that is applicable to oblique cutting processes in variable cutting conditions. A finite difference method based approach is followed in modelling of cutting temperatures. Oblique cutting process model is applied to prediction of turning temperatures by splitting turning geometry in to oblique cutting segments. This block by block modelling approach allows representing a complex problem with simpler subparts. Developed model only needs mechanical input from orthogonal calibration tests. Predicted temperature values are validated by using the data available in literature.

The thesis is organized as follows;

Chapter 2 covers the background information about thermal modelling of metal cutting in order to show current and past trends in modelling. Two main common approaches, analytical and numerical approaches, in modelling of cutting temperatures are briefly introduced in chronological manner.

In Chapter 3, mechanics of turning process is explained. First, basic oblique cutting process mechanics is introduced. Primary and secondary deformation zone analyses are presented in this first part with detailed explanation of cutting geometry. Then, application of oblique cutting principles to turning process is presented. In that second part, turning tool geometry and identification of cutting forces are introduced.

Thermal modelling of oblique process is introduced in Chapter 4. First, heat balance equation in generalized coordinates is presented. Then, discretization of the solution domain and followed solution approach are explained in detail.

In Chapter 5, validation simulations based on the data in reference [1] are presented. Simulations were carried out for nine cases. Chapter is concluded with comparisons of simulation results with experimental data.

Thesis is concluded in Chapter 6 with brief summary of thesis and future recommendations.

Chapter 2: Literature Review

Excessive amount heat generation and resulting high temperature gradients is one of the most important problems in machining. Those high temperature values put constraints on process parameter selection. Particularly, surface integrity and tool life are affected negatively. Even though there are many wear mechanisms; temperature has an important role in developing of wear. High temperature gradients results in severe thermal stresses which causes fatigue and eventually tool failure. In addition, tool wear can be accelerated if those gradients exceed crystal binding limits of tool material [2]. As a result of its significance, thermal effects in machining of materials have been broadly researched for more than one century. In this chapter, predictive temperature modelling approaches is grouped under two main groups which are analytical and numerical approaches. In following sub sections, some significant studies are briefly introduced in chronological manner.

2.1 Analytical Models

Analytical modelling approach is the oldest one among the available techniques. It is computationally less intensive when compared to numerical methods. On the other hand, complex machining geometries cannot be treated using it. Generally, solutions are for semi-infinite mediums and elementary geometries like rectangular shapes.

Machining temperature research can be traced back to Taylor's studies. He concluded that cutting temperatures affects tool life, energy consumption and surface integrity [3]. One of the first analytical temperature model for machining was developed by Trigger and Chao. In their work, they determined the average tool and chip interface temperature for orthogonal cutting. They assumed that tool and chip interface temperature is affected by shearing and frictional effects between tool and chip. They considered workpiece surfaces as adiabatic. Furthermore, shear plane was assumed as an oblique moving heat source that moves with cutting velocity in a semi-infinite

medium. They did not analyse temperature distribution around shear plane in their work [4] [5].

Loewen and Shaw modelled cutting temperatures by assuming shear plane as a moving heat source that moves with shear velocity. In their analysis, they postulated that all of the shearing power is converted in to heat. They derived useful expression for average shear plane and tool-chip interface temperatures [6]. Their modelling approach was an important one; since it gave a practical insight about process parameters and their effects on temperatures.

In 1954, Weiner proposed an analytical method in order to calculate temperature distributions along shear plane in orthogonal cutting. In that work, conduction heat transfer in directions of chip and workpiece motion is neglected in order to simplify the solution procedure and it was assumed that shear plane heat source velocity is equal to cutting velocity [7]. In that work, heat partition ratios for shear plane are also determined in a more detailed way compared to Loewen and Shaw' s [6] study.

Venuvinod and Lau presented a model for free oblique cutting [8]. They assumed tool and workpiece as semi-infinite mediums. A moving heat source solution was applied which considers source movement with an inclination. They introduced multiple discrete rectangular sources in order to account for the chip flow direction. Shear plane effect was modelled by extending Loewen and Shaw's [6] analysis. Furthermore, Blok's partition principle was employed on rake face in order to estimate heat flux inputs to tool and chip [9].

Berliner and Krainov built a model in order to determine tool and chip temperatures. They applied a parabolic form heat source on tool-chip interface. In addition, cooling effects were considered in their analysis. Deformation energy was considered in analysis by using a power law for material behaviour. They also included flank face friction in the analysis [10].

Stephenson and Ali developed an analysis technique that determines tool temperatures in interrupted cutting. Tool was assumed to be a semi-infinite body with

insulated boundaries and time varying heat flux was applied to corner of it. The resulting system was solved by using Green's function approach. They proposed solutions for different time dependent heat source types [11].

Young and Chou determined steady state tool-chip interface temperatures in orthogonal cutting. In their model, they assumed uniform heat flux distribution both on shear plane and rake face. Moreover, they neglected heat conduction in the direction of motion [12].

Radulescu and Kapoor determined three dimensional temperature distributions in continuous and interrupted machining. Their model consists of three parts. First, heat flux values for tool and workpiece were identified by doing chip formation zone analysis. This analysis was carried out for quasi steady state conditions. Then, temperature values for tool and chip were determined by utilizing the computed heat fluxes from the previous step. They included heat loss due to convection in their analytical solutions for tool and chip formation zone. An iterative solution was carried out to determine time dependent temperature values in tool [13]. Their model was important in terms of giving a physical understanding about the time dependent behaviour of the heating and cooling cycles in milling.

Stephenson et al. proposed a model in order to determine transient tool temperatures. Heat transfer problem for the tool was solved by employing separation of variables technique. Heat flux was applied to tool by using experimental tool chip contact area data. Moreover, piecewise constant heat flux was imposed to tool rake face [14]. After Stephenson et al. Jen and Anagoye extended that work. They included transient response and non-uniform heat flux distribution on rake face [15].

Ostafiev et al. determined tool temperatures in orthogonal cutting for steady state by assuming tool as a semi-infinite medium. They assumed multiple rectangular heat sources with uniform flux distribution on the rake face and calculated the tool temperatures by superposing the effects of those sources. In addition, mirror image

sources were defined for realistic analysis and they considered heat flux reflections [16].

Komanduri and Hou developed a model for orthogonal cutting that considers frictional and shear plane heat sources. They modelled the shear plane heat source as moving oblique heat source in semi-infinite medium by introducing a modified version of the Hahn's oblique band heat source model for infinite medium. Temperature rise in chip and workpiece near shear plane ,due to primary zone heat generation, was determined in the first part of their work [17]. In second part of their study, temperature rise, due to frictional heat source, in tool and chip was determined. Frictional heat source was modelled by modifying Jaeger's moving band and stationary source solutions. Non-uniform heat partition distribution between tool and chip was assumed in the analysis [18]. In the last part of their study, combined effect of shear plane and frictional heat sources was considered in order to determine tool-chip interface temperatures [19].

Komanduri and Hou's approach inspired many other researchers and their approach was extended. Chou and Song modelled the finish hard turning. They introduced multiple rectangular heat sources in order to represent the complex geometry in turning. They also included wear land heat source in their model. Furthermore, they assumed constant thermal properties [20]. Huang and Liang modelled the orthogonal cutting temperatures. They included wear land heat generation and non-uniform heat flux distribution on rake face in their study [21]. After that work, Li and Liang extended that work by adding cooling effects [22].

Richardson et al. simulated peripheral milling process by using method of moving heat sources. They adopted an angular integration procedure in order to calculate multiple heat source effect. In their study, heat flux value for workpiece was determined by conducting experiments. Furthermore, heat flux assumed to be proportional to chip thickness and local heat fluxes were determined according to that principle [23].

2.2 Numerical Models

Numerical modelling of cutting temperatures became popular after 1970s parallel to advancements in computers. The main advantage of numerical modelling is that complex geometries and boundary conditions in metal cutting can easily be treated by using it. Finite difference and finite element methods are the most common ones among that group. Therefore, only those two methods are introduced in this section.

2.2.1 Finite Difference Method Based Models

Besides early analytical modelling efforts that only regard temperatures on shear plane and tool-chip interface, Rapier was one of the first who attempted to model temperature distributions by using finite differences and analytical methods. He assumed tool, chip and workpiece as separate bodies. Shear plane heat source was modelled as constant temperature uniform strength line source. In addition, frictional heat source was also assumed to have uniform strength and it was assumed that all frictional heat enters in to chip. In the analysis, chip temperatures were modelled analytically by omitting the heat conduction along chip velocity direction. Finite difference method was employed to calculate workpiece and tool temperature distributions. [24].

Dutt and Brewer determined temperature distributions using finite difference method. They assumed tool, chip and workpiece as separate bodies with interactions at interfaces. In their approach, series of linear equations were written in finite difference form for shear plane and rake face boundaries by considering heat balance. Therefore, heat partition between bodies was figured out. In contrast to Rapier [24], they considered frictional heat that enters into tool [25].

Levy et al. proposed a two dimensional transient thermal model that considers only tool and chip temperature distributions in orthogonal cutting. Frictional heat source was introduced as a heat flux on boundary and it was assumed non-uniform along contact. In addition, shear plane heat source was included in model as internal heat generation [26].

Another modelling effort, based on finite difference approach, was proposed by Usui and Shirakashi. They applied Bishop's [27] "jerk" method in order to calculate temperature fields in turning. In their work, it was assumed that heat generation and transport occurs instantaneously followed by discrete time interval where conduction occurs. Furthermore, temperature rises due to shear plane and rake face heat sources were incorporated in analysis by using mechanical equivalent of heat [28].

Smith and Armarego [29] used finite difference method to model tool and chip temperatures for orthogonal cutting in three dimensions. Their model was based on thin shear zone analysis. They assumed uniform temperature on shear plane which is identified from Chao and Trigger's [30] average temperature rise relationship. Moreover, frictional heat source between tool and chip interface was assumed to be uniform along contact area. In solutions, they gave constant temperature to back of the tool and they showed that interfacial temperatures are not very sensitive to tool back face temperature value.

Lazoglu and Altintas [2] proposed a two dimensional temperature model in order to determine temperature fields in continuous orthogonal cutting and interrupted machining. Tool and chip temperature distributions were included in the analysis. Shear plane heat source was incorporated in analysis by introducing Oxley's [31] energy partition function. It was assumed that frictional heat source has uniform strength. In that study, transient temperature modelling of interrupted machining was carried out by making first order system approximation in solutions. Later on, Ulutan et al. [32] extended that model to three dimensional analysis of orthogonal cutting. In addition, they considered the convectional heat losses during the analyses.

In 2004 Grzesik et al. presented a numerical model that uses finite difference approach. Their model was capable of modelling coated and uncoated tools in orthogonal cutting. Before their work, all of the major finite difference approximation based studies only considered uncoated tools. In their study, temperature distributions along tool-chip interface and temperature distributions in tool were modelled. In the

analyses, they included thermal property changes with temperatures. Thermal behaviour of coating layers on tool was treated by introducing equivalent conductivity. Heat conduction along chip flow direction was neglected in their model [33].

2.2.2 Finite Element Method Based Models

Finite element method is another tool for modelling metal cutting temperatures. Modern finite element method allows fully predictive modelling and it can be easily adapted to different cutting processes (drilling, milling, grinding etc.). Therefore, there are numerous works that are available in literature.

Tay et al. was one of the first who modelled the tool, chip and workpiece temperatures in orthogonal cutting by using finite element method [34]. Formulations were made for two dimensional analyses. Strain, strain rate and velocity distributions were determined from quick stop experiments for primary shear zone that were done by Stevenson and Oxley [35]. Moreover, that experimental data was used to determine velocity distribution in secondary shear zone. A modified empirical power law approximation was made in order to represent constitutive behaviour in primary zone. Measured force data was used to determine frictional stress in secondary zone. According to their analyses, average shear flow stress assumption is not an inaccurate one. Although their temperature distributions were fairly well, extensive experimental work was needed to make temperature predictions. After this study, Tay et al. modified the model in order to reduce experimental dependency. In that model, primary zone heat source expression was simplified. In addition, elastic contact between tool and chip was neglected [36].

Muraka et al. proposed an improved model ,compared to [34], which considers tool flank heat source. Moreover, they tried to analyse effects of coolant on the temperature distributions. The main drawback of their approach is substantial amount of experimental data dependency in order to determine strain in primary and secondary zones [37].

Stevenson et al. presented a finite element model that is an updated version of their previous studies. In their study, shear flow stress determination method was changed to shear plane analysis based approach and mesh generation procedures were modified in order to consider different scenarios. Their updated model was able to work without experimental flow field input. In addition, that model was capable of accounting various contact lengths and shear angles [38].

Dawson and Malkin applied finite element method in order to model inclined moving heat source over semi-infinite solid. They applied their approach to predict shear plane temperatures in orthogonal cutting by assuming that all of the generated heat goes in to workpiece. They also considered heat losses due to material removal and convection in their formulations. In their study, effects of different inclination angles and cutting speeds were investigated for various conditions. Furthermore, they benchmarked their results with Jaeger's solution and found that numerical results are close to analytical ones at same conditions [39].

Strenkowski and Moon developed an Eulerian finite element model for orthogonal cutting process. Compared to previous works, their model did not require extensive experimental data which is an important advantage. Workpiece material was assumed to be viscoplastic material and they neglected elastic effects in their model. In addition, sliding friction was assumed between tool and chip. Temperature fields are modelled using a two dimensional conduction model with incorporating primary and secondary zone heat sources. In solution procedure, they approximated the initial chip geometry in order to start the solution [40].

Lin and Lin proposed a hybrid model in order to model orthogonal cutting process. In their model, temperature distributions were modelled by employing finite difference approach and chip formation process was simulated by using finite element method [41]. A thermo elastic plastic material model was used in the analysis. Sticking and sliding regions on tool -chip interface was considered when modelling the friction behaviour between tool and chip. They considered convectional heat losses in heat

transfer analysis. In their heat transfer analysis, they used an approach that is similar to Usui et al. [28].

Shih used finite element method to model orthogonal cutting process. In that study, he modelled the material as elastic viscoplastic. He developed a new sticking sliding friction model in order to estimate tool-chip interaction on rake face. Local calculations were made for each node in sticking region friction modelling and coulomb's friction law was employed for sliding region. Unbalanced force reduction was developed in order to simulate incremental movement of the tool. Temperatures were determined through iterative solution procedure [42].

Wu et al. simulated orthogonal cutting process by using a thermo-viscoplastic material behaviour model. In contrast to Zorev's idealized friction modelling, authors employed a sticking sliding friction model that uses local effective stresses in calculations. In temperature simulations, thermal properties were assumed to be constant. In addition, tool chip contact was assumed to be perfect. Therefore, temperature distributions at there was considered as continuous [43].

Ng et al. modelled orthogonal machining using FORGE2® finite element code in the analysis. Material was assumed to behave as elastic viscoplastic and von-misses yield criterion was used by authors. Furthermore, sticking and sliding regions were considered between tool-chip interface. In thermal analysis part, two dimensional heat transfer calculations were carried out. Heat partition between tool and chip was taken constant along contact and partition values were calculated according to thermal effusivities. Their results were in good agreement with the experimental ones [44].

Ceretti et al. applied the commercial finite element code DEFORM2D to orthogonal cutting process with modifications [45]. After that work, Ozel et al. simulated end milling process by using DEFORM2D. They used Zorev's friction model in the analysis. Moreover, temperature values for tool, chip and workpiece were predicted [46]. Pittala and Monno modelled the temperatures in milling by employing two dimensional analyses by using DEFORM2D and 3D. First, they calculated the

cutting temperatures using two dimensional calculations. Then, they used that results as inputs to three dimensional workpiece temperature simulations [47].

Chapter 3: Modelling Mechanics of Turning Process

Mechanical modelling of the turning process is the first step in thermal modelling procedure. Therefore, thermal model inputs are determined by using output of mechanical analysis. Details about temperature model are given in the related chapter. In this chapter, modelling of cutting forces is presented. Firstly, oblique cutting mechanics is explained. Afterwards, turning tool geometry and force prediction model based on oblique cutting mechanics is presented.

3.1 Oblique Cutting Mechanics

The geometry of oblique cutting is demonstrated in Figure 3-1. Oblique cutting is the fundamental process to analyse common machining processes. Thus, first this basic process is explained. In oblique cutting process, cutting velocity component makes an angle with the cutting edge normal plane. This angle is called inclination angle (λ_s). This orientation creates force components in tangential, radial and feed directions with respect to tool. Therefore, analyses are carried out accordingly.

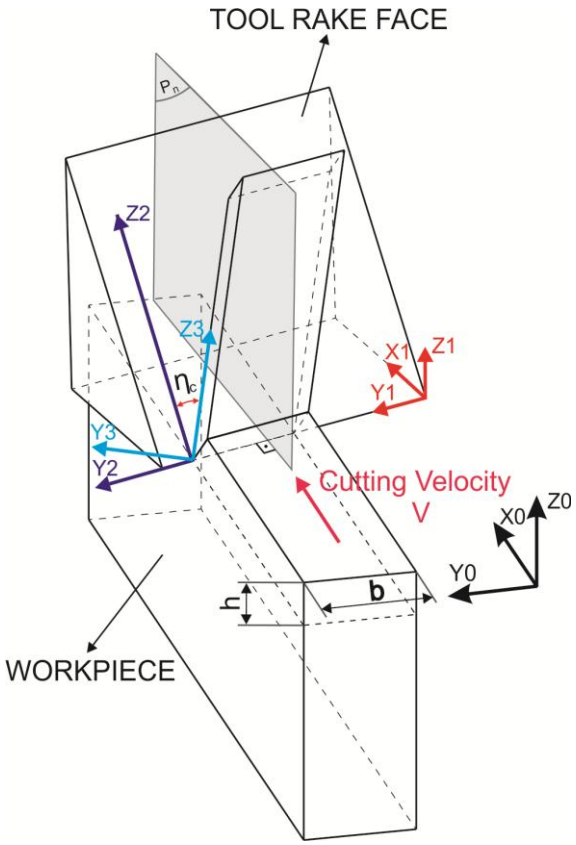

Figure 3-1 Oblique Cutting Geometry

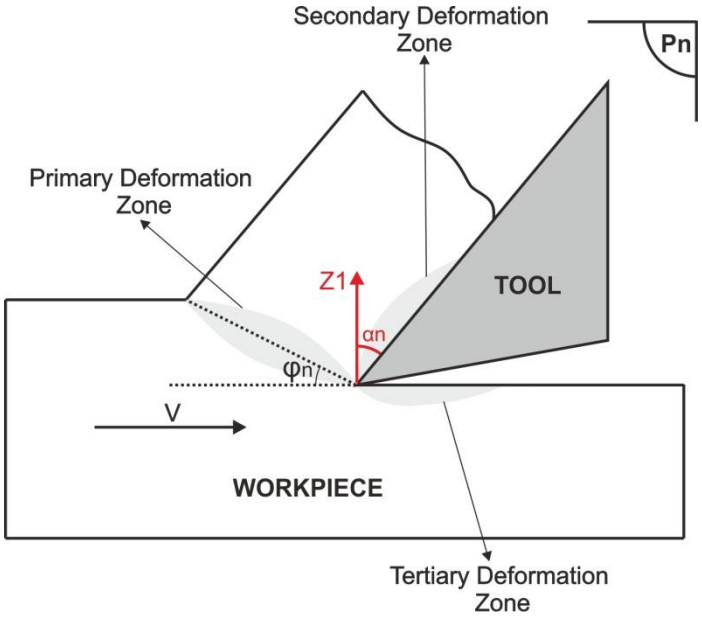

Figure 3-2 Deformation Zones

Metal cutting is a high strain rate deformation process. Penetration of the tool into workpiece leads to material removal due to high amount of plastic deformation that takes place in shear zone. In order to make analysis easier, shear zone is assumed to have a constant thickness in analysis [48]. Its angular position with respect to workpiece surface is defined by normal shear angle (φ_n) which is defined on the cutting edge normal plane (P_n). Removed material moves over the rake face of cutting tool and slightly deforms during this movement due to frictional effects. This deformation area between tool and chip (removed material) is called secondary deformation zone. In addition, there is a third deformation zone called tertiary zone. This zone is created due to rubbing between tool flank and machined surface. In this thesis, tool assumed perfectly sharp and tertiary zone deformation is neglected; this assumption is valid for unworn tools without a flank wear land [49].

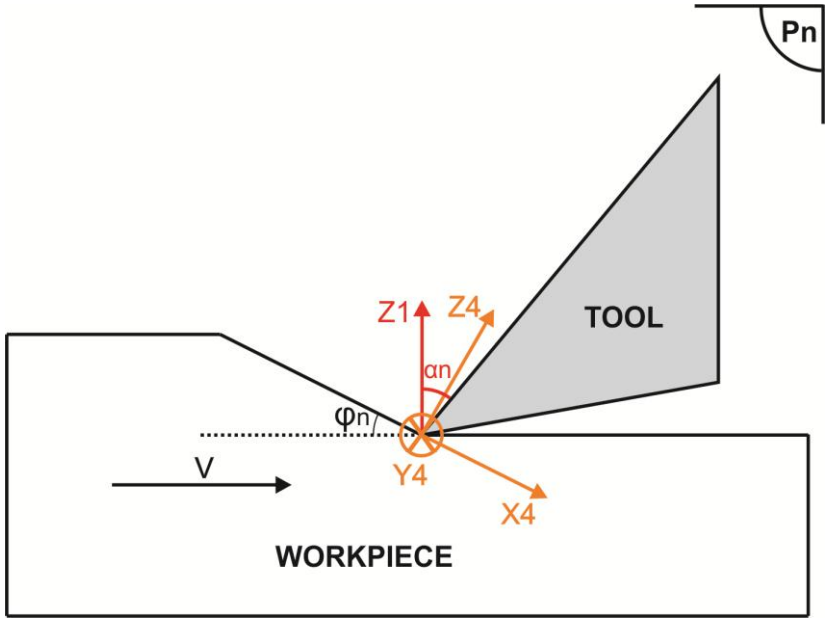

Figure 3-3 View from Cutting Edge Normal Plane

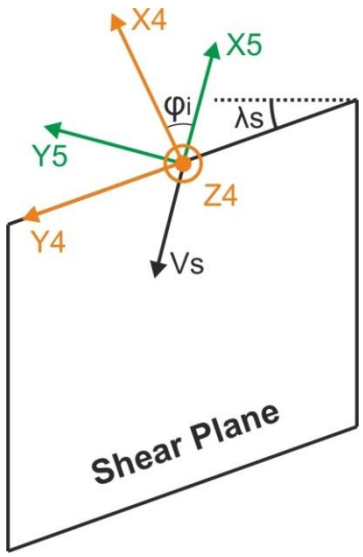

Figure 3-4 Shear Plane View from Z4 Direction

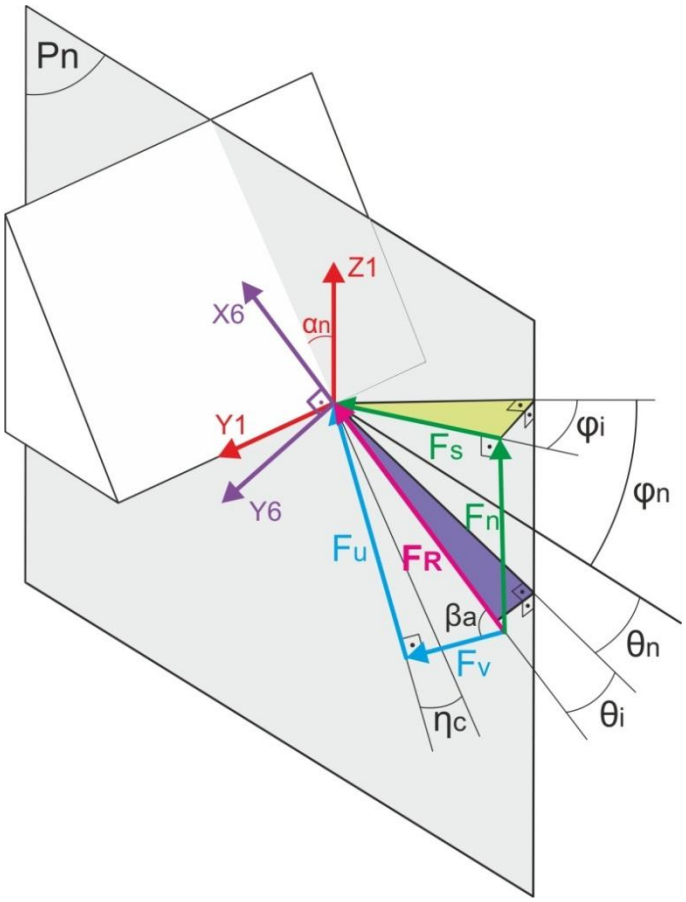

Figure 3-5 Oblique Cutting Forces and Geometry

Mechanical analyses are carried out by considering primary and secondary deformation zones. In primary deformation zone, shearing force (F_s) and shear normal force (F_n) components are created at the outflow of the shear zone due to shearing action. Moreover in secondary deformation zone, friction force on rake face (F_u) and normal force on rake face (F_v) are created in secondary deformation zone. Relationship between those force components and resultant cutting force is expressed as;

$$\overrightarrow{F_R} = \overrightarrow{F_s} + \overrightarrow{F_n} \tag{3.1}$$

$$\overrightarrow{F_R} = \overrightarrow{F_u} + \overrightarrow{F_v} \tag{3.2}$$

In the analyses, forces on rake face and shear plane are associated with resultant cutting force using the appropriate vector transformations. Coordinate frames are introduced in order to ease the analysis. All coordinate frames are demonstrated in Figure 3-1, Figure 3-3, Figure 3-4 and Figure 3-5

[X_0, Y_0, Z_0] is main coordinate frame. X_0 direction is collinear with cutting velocity component and Z_0 direction is opposite to feed direction. [X_1, Y_1, Z_1] is cutting edge coordinate frame. Y_1 direction is collinear with cutting edge, Z_1 direction is opposite to feed direction and parallel to P_n. [X_2, Y_2, Z_2] is rake face coordinate frame. Y_2 direction is collinear with cutting edge, Z_2 direction lies on rake face and parallel to P_n. [X_3, Y_3, Z_3] is chip flow coordinate frame. Z_3 is on rake face and it is in same direction with chip flow motion. [X_4, Y_4, Z_4] is shear plane coordinate frame. Y_4 is collinear with cutting edge. X_4 is on shear plane and it is directed perpendicular to cutting edge. [X_5, Y_5, Z_5] is shearing coordinate frame. X_5 is parallel to shearing velocity and directed to cutting edge. [X_6, Y_6, Z_6] is resultant cutting force coordinate frame. X_6 axis defines the direction of resultant cutting force. Coordinate frames are defined with respect to each other suing the following rotation matrixes.

$$R_{01} = \begin{bmatrix} \cos(\lambda_s) & -\sin(\lambda_s) & 0 \\ \sin(\lambda_s) & \cos(\lambda_s) & 0 \\ 0 & 0 & 1 \end{bmatrix} \tag{3.3}$$

$$R_{12} = \begin{bmatrix} \cos(\alpha_n) & 0 & \sin(\alpha_n) \\ 0 & 1 & 0 \\ -\sin(\alpha_n) & 0 & \cos(\alpha_n) \end{bmatrix} \tag{3.4}$$

$$R_{23} = \begin{bmatrix} 1 & 0 & 0 \\ 0 & \cos(\eta_c) & -\sin(\eta_c) \\ 0 & \sin(\eta_c) & \cos(\eta_c) \end{bmatrix} \tag{3.5}$$

$$R_{14} = \begin{bmatrix} \cos(\phi_n) & 0 & \sin(\phi_n) \\ 0 & 1 & 0 \\ -\sin(\phi_n) & 0 & \cos(\phi_n) \end{bmatrix} \tag{3.6}$$

$$R_{45} = \begin{bmatrix} \cos(\phi_i) & \sin(\phi_i) & 0 \\ -\sin(\phi_i) & \cos(\phi_i) & 0 \\ 0 & 0 & 1 \end{bmatrix} \tag{3.7}$$

$$R_{16} = \begin{bmatrix} \cos(\theta_n) & 0 & -\sin(\theta_n) \\ 0 & 1 & 0 \\ \sin(\theta_n) & 0 & \cos(\theta_n) \end{bmatrix} . \begin{bmatrix} \cos(\theta_i) & \sin(\theta_i) & 0 \\ -\sin(\theta_i) & \cos(\theta_i) & 0 \\ 0 & 0 & 1 \end{bmatrix} \tag{3.8}$$

Note that rotation angles are defined through the text.

First primary deformation zone is examined: Shear force (F_s) lies on shear plane and it can be calculated by multiplying the average shear flow stress (τ_s) and shear area (A_s).

$$F_s = \tau_s . A_s \tag{3.9}$$

In oblique cutting, shear plane is assumed as a parallelogram. Its area can be calculated by equating the volumetric material flow through primary zone and undeformed chip area [50];

$$b.h.V = A_s . V_n \tag{3.10}$$

Where b is width of cut and h is depth of cut. V_n is the material velocity component normal to shear plane. According to geometry in Figure 3-3, this velocity component can be written as;

$$V_n = V.\cos(\lambda_s).\sin(\phi_n) \tag{3.11}$$

Equations (3.10) and (3.11) yield following relationship,

$$A_s = \frac{b.h}{\sin(\phi_n).\cos(\lambda_s)} \tag{3.12}$$

Shearing force is collinear with the shear velocity direction and its orientation with respect to cutting edge normal plane (P_n) is defined by ϕ_i. Resultant cutting force (F_R) can be associated with shearing force by defining vector transformations which results in the equation (3.13). Note that resultant cutting force component along the direction of shear assumed as shearing force.

$$F_s = F_R.\left(\cos(\theta_i).\cos(\phi_i).\cos(\theta_n + \phi_n) + \sin(\theta_i).\sin(\phi_i)\right) \tag{3.13}$$

, or alternatively,

$$F_R = \frac{\tau_s.b.h}{\left(\cos(\theta_i).\cos(\phi_i).\cos(\theta_n + \phi_n) + \sin(\theta_i).\sin(\phi_i)\right).\sin(\phi_n).\cos(\lambda_s)} \tag{3.14}$$

θ_i is projection angle between resultant cutting force and cutting edge normal plane. θ_n is angle between newly generated surface and projection of resultant cutting force on cutting edge normal plane.

Secondary zone force components can also be associated with the resultant cutting force using the mean friction angle (β_a) [51]. From Figure 3-5 following relationships are deduced;

$$F_u = F_R.sin(\beta_a) = F_R.\frac{\sin(\theta_i)}{\sin(\eta_c)} \tag{3.15}$$

$$F_v = F_R.\cos(\beta_a) \tag{3.16}$$

$$F_u = F_v.\mu = F_v.\tan(\beta_a) = F_v.\frac{\tan(\alpha_n + \theta_n)}{\cos(\eta_c)} \tag{3.17}$$

$$\overset{results\ in}{\Rightarrow} \quad \theta_i = \sin^{-1}\left(\sin(\beta_a).\sin(\eta_c)\right) \tag{3.18}$$

$$\alpha_n + \theta_n = \tan^{-1}\left(\cos(\eta_c).\tan(\beta_a)\right) \tag{3.19}$$

Where η_c is chip flow angle measured from cutting edge normal plane on rake face. It describes the chip flow direction on rake face. α_n is normal rake angle which is angle measured on cutting edge normal plane between rake face and plane perpendicular to cutting velocity. μ is mean friction coefficient. Note that above mentioned shear stress, friction angle and shear angle values are identified for specific workpiece and tool material combination by conducting series of orthogonal cutting experiments.

Identification velocity components in oblique cutting are important in order to calculate power inputs in thermal model. Shear velocity direction can be identified using the velocity relation between chip, cutting and shearing velocities.

$$\vec{V} + \vec{V_s} = \vec{V_c} \tag{3.20}$$

Where $\vec{V}$, $\vec{V_s}$ and $\vec{V_c}$ are cutting, shearing and chip velocities respectively. First, chip and cutting velocities transformed on to shear plane in order to do vector summation in equation (3.20).

$$\mathrm{R}_{14}^{\mathrm{T}}.\mathrm{R}_{01}^{\mathrm{T}}.\begin{bmatrix} \mathrm{V} \\ 0 \\ 0 \end{bmatrix} = \begin{bmatrix} \mathrm{V}.\cos(\lambda_s).\cos(\phi_n) \\ -\mathrm{V}.\sin(\lambda_s) \\ \mathrm{V}.\cos(\lambda_s).\sin(\phi_n) \end{bmatrix} \tag{3.21}$$

$$\mathrm{R}_{14}^{\mathrm{T}}.R_{12}.\mathrm{R}_{23}.\begin{bmatrix} 0 \\ 0 \\ \mathrm{V_c} \end{bmatrix} = \begin{bmatrix} \mathrm{V_c}.\cos(\eta_c).(\cos(\phi_n).\sin(\alpha_n) - \cos(\alpha_n).\sin(\phi_n)) \\ -\sin(\eta_c).\mathrm{V_c} \\ \mathrm{V_c}.\cos(\eta_c).(\cos(\alpha_n).\cos(\phi_n) + \sin(\alpha_n).\sin(\phi_n)) \end{bmatrix} \tag{3.22}$$

According to one dimensional material flow assumption in shear zone, velocity components perpendicular to shear plane at entrance and exit of the shear zone should

be equal to each other [50]. Using this principle chip velocity magnitude can be identified.

$$V_c = \frac{V.\cos(\lambda_s).\sin(\phi_n)}{\cos(\eta_c).\cos(\phi_n - \alpha_n)} \tag{3.23}$$

$$\overset{results\ in}{\Rightarrow} \vec{V_s} = \begin{bmatrix} -V.\cos(\lambda_s).\cos(\alpha_n).\sec(\alpha_n - \phi_n) \\ V.(\sin(\lambda_s) - \cos(\lambda_s).\sec(\alpha_n - \phi_n).\sin(\phi_n).\tan(\eta_c)) \\ 0 \end{bmatrix} \tag{3.24}$$

Shearing velocity direction on shear plane is figured out using equation (3.24) which yields expression in equation (3.25) for ϕ_i.

$$\begin{aligned} \tan(\phi_i) &= \frac{(\sin(\lambda_s) - \cos(\lambda_s).\sec(\alpha_n - \phi_n).\sin(\phi_n).\tan(\eta_c))}{-\cos(\lambda_s).\cos(\alpha_n).\sec(\alpha_n - \phi_n)} \\ &= \sec(\alpha_n).(\tan(\eta_c).\sin(\phi_n) - \tan(\lambda_s).\cos(\alpha_n - \phi_n)) \end{aligned} \tag{3.25}$$

After defining oblique cutting geometry, cutting force expressions are written in linear form. K_{tc} ,K_{rc}, K_{fc} are cutting force coefficients and they represent the shearing effect in force expression. K_{te} ,K_{re}, K_{fe} are edge force coefficients; they represent ploughing effect in force expression. It should be noticed that ploughing effect does not contribute to shearing mechanism. Those coefficients are identified for different workpiece material and tool combinations by conducting orthogonal calibration experiments.

$$F_{X0} = F_{tc} + F_{te} = K_{tc}.b.h + K_{te}.b \tag{3.26}$$

$$F_{Y0} = F_{rc} + F_{re} = K_{rc}.b.h + K_{re}.b \tag{3.27}$$

$$F_{Z0} = F_{fc} + F_{fe} = K_{fc}.b.h + K_{fe}.b \tag{3.28}$$

Using the transformations (3.3) between (3.8) and equation (3.13) cutting part of the forces is written as follows;

$$F_{tc} = F_R.(\cos(\lambda_s).\cos(\theta_i).\cos(\theta_n) + \sin(\lambda_s).\sin(\theta_i)) = \frac{b.h.\tau_s.\csc(\phi_n)(\cos(\theta_i)\cos(\theta_n) + \tan(\lambda_s)\sin(\theta_i))}{\cos(\theta_i).\cos(\phi_i).\cos(\theta_n + \phi_n) + \sin(\theta_i).\sin(\phi_i)} \quad (3.29)$$

$$F_{rc} = F_R.(\cos(\theta_i).\cos(\theta_n).\sin(\lambda_s) - \cos(\lambda_s).\sin(\theta_i)) = \frac{b.h.\tau_s.\csc(\phi_n).(\tan(\lambda_s).\cos(\theta_i).\cos(\theta_n) - \sin(\theta_i))}{\cos(\theta_i).\cos(\phi_i).\cos(\theta_n + \phi_n) + \sin(\theta_i).\sin(\phi_i)} \quad (3.30)$$

$$F_{fc} = F_R.\cos(\theta_i).\sin(\theta_n) = \frac{b.h.\tau_s.\sec(\lambda_s).\cos(\theta_i).\sin(\theta_n).\csc(\phi_n)}{\cos(\theta_i).\cos(\phi_i).\cos(\theta_n + \phi_n) + \sin(\theta_i).\sin(\phi_i)} \quad (3.31)$$

$$K_{tc} = \frac{\tau_s.\csc(\phi_n).(\cos(\theta_i).\cos(\theta_n) + \tan(\lambda_s).\sin(\theta_i))}{\cos(\theta_i).\cos(\phi_i).\cos(\theta_n + \phi_n) + \sin(\theta_i).\sin(\phi_i)} \quad (3.32)$$

$$K_{rc} = \frac{\tau_s.\csc(\phi_n).(\tan(\lambda_s).\cos(\theta_i).\cos(\theta_n) - \sin(\theta_i))}{\cos(\theta_i).\cos(\phi_i).\cos(\theta_n + \phi_n) + \sin(\theta_i).\sin(\phi_i)} \quad (3.33)$$

$$K_{fc} = \frac{\tau_s.\sec(\lambda_s).\cos(\theta_i).\sin(\theta_n).\csc(\phi_n)}{\cos(\theta_i).\cos(\phi_i).\cos(\theta_n + \phi_n) + \sin(\theta_i).\sin(\phi_i)} \quad (3.34)$$

By using the equations (3.26) to (3.28) oblique cutting forces can be calculated.

Determination of chip flow direction is important for accurate predictions. Therefore, minimum energy principle is employed; in order to identify chip flow direction, normal shear angle and shearing direction [51]. Normally chip flow angle is assumed equal to inclination angle for practical purposes according to Stabler rule [52]. However, Brown and Armarego showed that this assumption is not valid for different inclination and rake angles [53]. Minimum energy principle states that cutting power must be minimal for unique shear angle solution. First, cutting power expression is written.

$$P_{cutting} = F_{tc}.V = \frac{b.h.\tau_s.\csc(\phi_n).(\cos(\theta_i).\cos(\theta_n) + \tan(\lambda_s).\sin(\theta_i))}{\cos(\theta_i).\cos(\phi_i).\cos(\theta_n + \phi_n) + \sin(\theta_i).\sin(\phi_i)}.V \quad (3.35)$$

Then, cutting power expression is nondimensionalized by dividing the equation (3.35) to "$V.b.h.\tau_s$" .

$$P'_{cutting} = \frac{P_{cutting}}{V.b.h.\tau_s} = \frac{\csc(\phi_n).(\cos(\theta_i).\cos(\theta_n) + \tan(\lambda_s).\sin(\theta_i))}{\cos(\theta_i).\cos(\phi_i).\cos(\theta_n + \phi_n) + \sin(\theta_i).\sin(\phi_i)} \tag{3.36}$$

In order to minimize the cutting power, conditions in equations (3.37) and (3.38) should be satisfied.

$$\frac{\partial P'_{cutting}}{\partial \phi_n} = 0 \tag{3.37}$$

$$\frac{\partial P'_{cutting}}{\partial \phi_i} = 0 \tag{3.38}$$

Shear angle solutions are found by iterating φ_n and φ_i. At the beginning of the solution procedure, Stabler's rule and orthogonal data base can be used for initial guess of chip flow and shear angle values. Iterations are continued until the nondimensional cutting power reaches a minimum value.

$$\phi_n(k) = \phi_n(s-1) - SS.(\frac{\Delta P'_{cutting}}{\Delta \phi_n}) \tag{3.39}$$

$$\phi_i(k) = \phi_i(s-1) - SS.(\frac{\Delta P'_{cutting}}{\Delta \phi_i}) \tag{3.40}$$

s in the equations (3.39) and (3.40) represents iteration counter. SS represents the step size for shear angle change. Throughout the iterations chip flow angle can be calculated using the shearing direction equation (3.25). As stated previously, shear stress and friction angle values are taken from orthogonal cutting database.

Identification of tool chip contact length is important in order to determine contact area between tool and chip. Therefore, this quantity is evaluated by taking moments of shear normal force and frictional normal force with respect to cutting edge.

Note that uniform pressure distribution is assumed on shear plane and on tool chip interface (in real case there is a pressure distribution).

$$F_v = F_R.\cos(\beta_a) = F_R.\left(\cos(\theta_i).\left(\cos(\alpha_n).\cos(\theta_n) - \sin(\alpha_n).\sin(\theta_n)\right)\right) \tag{3.41}$$

$$F_n = F_R.\cos(\theta_i).sin(\theta_n + \phi_n) \tag{3.42}$$

$$\begin{aligned} & F_v.\frac{l_{contact}}{2}.\cos(\eta_c) = F_n.\frac{\left(\frac{h}{sin(\phi_n)}\right)}{2} \\ \overset{yields}{\Rightarrow} \quad & l_{contact} = \frac{h.\sec(\eta_c).sin(\theta_n + \phi_n)}{sin(\phi_n).(\cos(\alpha_n).\cos(\theta_n) - \sin(\alpha_n).sin(\theta_n))} \end{aligned} \tag{3.43}$$

In above equations h corresponds to uncut chip thickness, $l_{contact}$ corresponds to tool chip contact length. Shearing power and friction power can be figured out by multiplying force components with the related velocity components.

$$P_{shear} = F_s.V_s \tag{3.44}$$

$$P_{friction} = F_u.V_c \tag{3.45}$$

3.2 Turning Process

Turning is a fundamental metal cutting operation in which workpiece is revolved and unwanted material is removed by movement of cutting tool. A CNC turning machine can be seen in Figure 3-6. In this section necessary analysis procedure is presented for turning force prediction.

Figure 3-6 CNC Turning Machine

Turning mechanics is modelled by discretizing the engaged part of the cutting tool. Thus, complex tool geometry is divided to easier to analyse subparts when compared to whole geometry. Each discretized element is assumed to make an oblique cutting operation. First step in the analysis is calculation of local inclination and normal rake angle values depending on the tool geometry. After that, local oblique cutting mechanics can be analysed by using the expressions that are explained former section in the text.

3.2.1 Tool geometry

First, local tool geometry for each discretized element should be determined in order to analyse local oblique cutting operations. Turning tool geometry can be defined by introducing reference planes. P_r (X_mZ_m plane in Figure 3-7) is tool reference plane and it is perpendicular to cutting velocity (V). P_n (Y_eZ_e plane in in Figure 3-7) is cutting edge normal plane and it is perpendicular to the cutting edge. P_f (Y_mZ_m plane in Figure 3-7) is named as working plane. It is parallel to feed direction and perpendicular to P_r. P_s is cutting edge plane. It is tangential to the cutting edge and perpendicular to P_r. P_p

(X_mY_m plane in Figure 3-7) is back plane and is perpendicular to both P_r and P_f. Note that tool geometry modelling approach was adopted from reference [54].

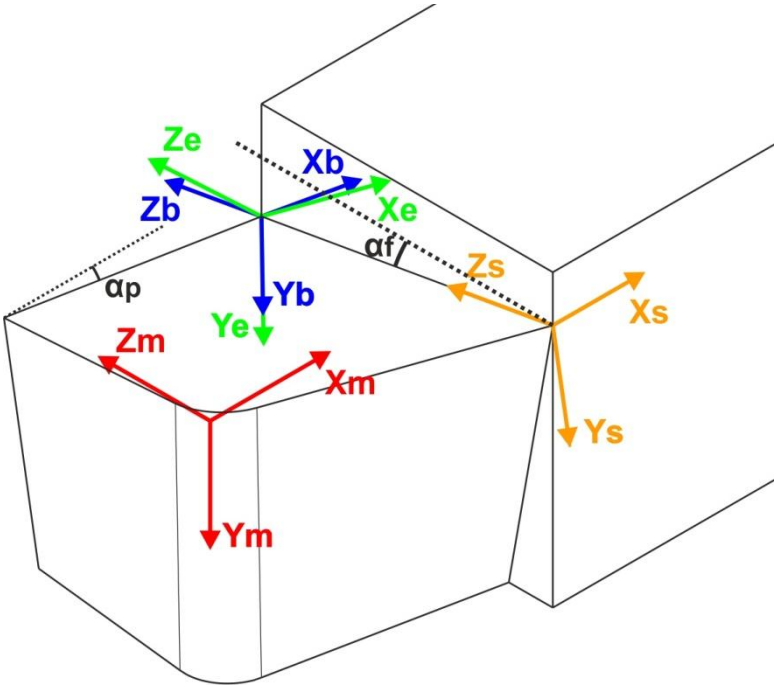

Figure 3-7 Tool Geometry

Local tool angles are defined using the side rake (α_f), back rake angle (α_p) and cutting edge angle (κr). They are shown in Figure 3-7 α_f is defined as projection of angle between P_r and rake face on to P_f. α_p is defined as projection of angle between P_r and rake face on to P_p. κr is angle between P_s and P_f. Series of coordinate frames are introduced in order to make analysis easier. Coordinate frames are presented in Figure 3-7. [X_m, Y_m, Z_m] is machine coordinate frame. Z_m is parallel and coincident with the workpiece rotation axis. X_m is directed outwards in workpiece radial direction. [X_s, Y_s, Z_s] is side rake angle coordinate frame. It is created by rotating the machine coordinate frame around X_m by amount of α_f in clockwise direction. [X_b, Y_b, Z_b] is back rake angle coordinate frame. It is created by rotating the side rake angle coordinate frame around Z_s by amount of α_p in counter-clockwise direction. [X_e, Y_e, Z_e] is edge coordinate frame. It is created by rotating the back rake angle coordinate frame around Y_b by

amount of ψ^* in counter-clockwise direction. ψ^* is described in latter part. Transformation sets are given below;

$$\begin{bmatrix} X_m \\ Y_m \\ Z_m \end{bmatrix} = R_{ms}.\begin{bmatrix} X_s \\ Y_s \\ Z_s \end{bmatrix} = \begin{bmatrix} 1 & 0 & 0 \\ 0 & \cos(\alpha_f) & \sin(\alpha_f) \\ 0 & -\sin(\alpha_f) & \cos(\alpha_f) \end{bmatrix}.\begin{bmatrix} X_s \\ Y_s \\ Z_s \end{bmatrix} \tag{3.46}$$

$$\begin{bmatrix} X_s \\ Y_s \\ Z_s \end{bmatrix} = R_{sb}.\begin{bmatrix} X_b \\ Y_b \\ Z_b \end{bmatrix} = \begin{bmatrix} \cos(\alpha_p) & -\sin(\alpha_p) & 0 \\ \sin(\alpha_p) & \cos(\alpha_p) & 0 \\ 0 & 0 & 1 \end{bmatrix}.\begin{bmatrix} X_b \\ Y_b \\ Z_b \end{bmatrix} \tag{3.47}$$

$$\begin{bmatrix} X_b \\ Y_b \\ Z_b \end{bmatrix} = R_{be}.\begin{bmatrix} X_e \\ Y_e \\ Z_e \end{bmatrix} = \begin{bmatrix} \cos(\psi^*) & 0 & \sin(\psi^*) \\ 0 & 1 & 0 \\ -\sin(\psi^*) & 0 & \cos(\psi^*) \end{bmatrix}.\begin{bmatrix} X_e \\ Y_e \\ Z_e \end{bmatrix} \tag{3.48}$$

Using the above transformations, normal rake angle and inclination angle can be found.

Normal rake angle is projection of angle between P_r and rake face on to P_n. First P_r normal vector is transformed to [X_e, Y_e, Z_e] coordinate frame. Then using unit vectors in Y_e, Z_e directions normal rake angle can be determined.

$$R^T{}_{ms}.R^T{}_{sb}.R^T{}_{be}.\begin{bmatrix} 0 \\ 1 \\ 0 \end{bmatrix} = \begin{bmatrix} -\sin(\alpha_f).\sin(\psi^*)+\cos(\psi^*).\sin(\alpha_p).\cos(\alpha_f) \\ \cos(\alpha_p).\cos(\alpha_f) \\ cos(\psi^*).\sin(\alpha_f)+\sin(\psi^*).\sin(\alpha_p).\cos(\alpha_f) \end{bmatrix}$$

$$\alpha_n = Tan^{-1}\left(\frac{\cos(\psi^*).\sin(\alpha_f)+\sin(\psi^*).\sin(\alpha_p).\cos(\alpha_f)}{\cos(\alpha_p).\cos(\alpha_f)}\right) \tag{3.49}$$

Inclination angle is projection of angle between P_r and cutting edge to P_s. X_e is transformed on to P_s by using following transformation;

$$\begin{bmatrix} \cos(\psi^*) & 0 & -\sin(\psi^*) \\ 0 & 1 & 0 \\ \sin(\psi^*) & 0 & \cos(\psi^*) \end{bmatrix}.R_{ms}.R_{sb}.R_{be}.\begin{bmatrix} 1 \\ 0 \\ 0 \end{bmatrix} =$$

$$\begin{bmatrix} \cos(\alpha_f).\sin^2(\psi^*)+\cos^2(\psi^*).\cos(\alpha_p)+\cos(\psi^*).\sin(\psi^*).\sin(\alpha_p).\sin(\alpha_f) \\ \cos(\psi^*).\cos(\alpha_f).\sin(\alpha_p)-\sin(\psi^*).\sin(\alpha_f) \\ \cos(\psi^*).\sin(\psi^*).\cos(\alpha_p)-\cos(\alpha_f).\sin(\psi^*).\cos(\psi^*)-\cos^2(\psi^*).\sin(\alpha_p).\sin(\alpha_f) \end{bmatrix}$$

$$\lambda_s = Tan^{-1}\left(\frac{\cos(\psi^*).\cos(\alpha_f).\sin(\alpha_p)-\sin(\psi^*).\sin(\alpha_f)}{\cos(\alpha_f).\sin^2(\psi^*)+\cos^2(\psi^*).\cos(\alpha_p)+\cos(\psi^*).\sin(\psi^*).\sin(\alpha_p).\sin(\alpha_f)}\right) \quad (3.50)$$

3.2.2 Cutting Force Prediction

Turning process is modelled using oblique cutting mechanics. First tool geometry is defined using nose radius, back rake angle, side rake angle, included angle and side cutting angle. Then, local oblique cutting geometry is figured out using the previously derived expressions. Tool geometry is analysed in two parts. First part of tool is named main cutting edge where chip thickness is constant; this region is showed on figure Figure 3-8 with dark grey area. Second part of the tool has radius; this region is showed on figure Figure 3-8 with light grey area. Owing to geometry, chip thickness is changing in this part. Depending on depth of cut, these two parts or only nose radius might be engaged with the workpiece. Considering the geometry in Figure 3-8, analyses are made. Depending on the depth of cut, three types of engagement scenario can take place.

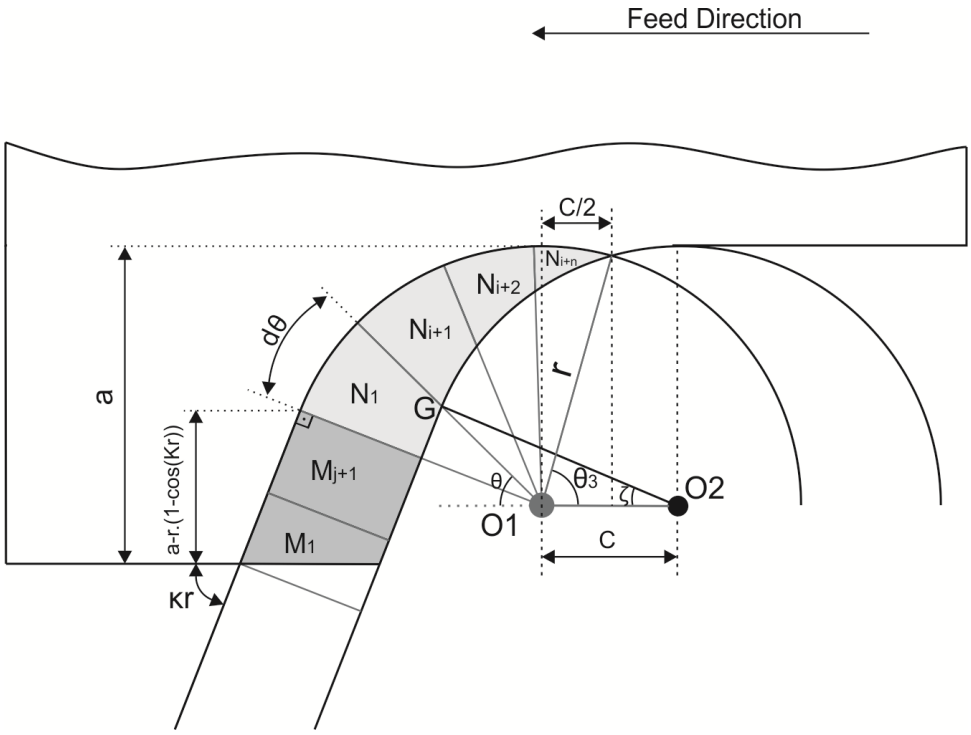

Figure 3-8 Schematic of a Turning Tool Engaged with a Workpiece When $\boldsymbol{a > r.(1 - \cos(kr))}$

First case, $a > r.(1 - \cos(\mathrm{kr}))$:

Main cutting edge and tool nose are engaged in this situation. Forces are calculated separately for nose part and for main cutting edge. For main cutting edge, oblique force components are determined by discretizing the main cutting edge in to smaller parts.

$$dFt_{main} = Ktc.\Delta A_{main} + Kte.\Delta l_{main} \tag{3.51}$$

$$dFf_{main} = Kfc.\Delta A_{main} + Kfe.\Delta l_{main} \tag{3.52}$$

$$dFr_{main} = Krc.\Delta A_{main} + Kre.\Delta l_{main} \tag{3.53}$$

Cutting coefficients (Ktc, Kfc, Krc) are determined using equations (3.32) to (3.34). ΔA_{main}, Δl_{main} represent differential chip area and differential cutting edge length respectively. Edge coefficients (Kte, Kfe, Kre) are determined form orthogonal

cutting tests. Note that radial edge coefficient is theoretically zero when orthogonal to oblique transformation is employed. Corresponding chip area and cutting edge length for main cutting edge is figured out using equations (3.54) to (3.55). Chip area calculation is different for main cutting edge element one (M_1) as can be seen in Figure 3-8.

$$for\ M_1\ element,\ \ \Delta A_{main} = \frac{c + \frac{c}{\sin(\kappa r)}}{2}.\Delta l_{main} \tag{3.54}$$

$$for\ M_{j+1}\ element,\ \ \Delta A_{main} = \frac{c}{\sin(\kappa r)}.\Delta l_{main} \tag{3.55}$$

$$\Delta l_{main} = \frac{a.(1-\cos(\kappa r))}{N_{main}} \tag{3.56}$$

In equations (3.54) to (3.56), c, Δl_{main}, a, N_{main} are feed rate (mm/rev), width of cut for each element, radial depth of cut and number of main cutting edge elements respectively.

ψ^* for main cutting edge is expressed as,

$$\psi^* = \frac{\pi}{2} - \kappa r \tag{3.57}$$

For nose part of the tool forces are calculated by discretizing engaged part of the nose radius to N_{rad} parts; for each segment forces are determined by using equations (3.58) to (3.60).

$$dFt = Ktc.dA + Kte.dl \tag{3.58}$$

$$dFf = Kfc.dA + Kfe.dl \tag{3.59}$$

$$dFr = Krc.dA + Kre.dl \tag{3.60}$$

Since chip thickness varies in this region, a different approach is driven in order to calculate the chip area (dA). Dimensions of the discretized regions are determined

according to desired number of elements in simulations; so that each element discretized to N elements again in order to calculate more accurate chip area and average chip thickness. Engaged part of the nose radius for this case can be figured out from Figure 3-8 by using θ_3 angle.

$$\theta_3 = \cos^{-1}\left(\frac{c}{2.r}\right) \tag{3.61}$$

$$dA = \sum_{i=1}^{i=N} \frac{r^2.\left(\frac{d\theta}{N-1}\right)}{2} - \frac{(GO_1)^2.\left(\frac{d\theta}{N-1}\right)}{2} \tag{3.62}$$

$$dl = r.d\theta \tag{3.63}$$

GO_1 (in Figure 3-8) is identified by applying law of cosines.

$$GO_1 = \sqrt{c^2 + r^2 - 2.c.r.\cos(\zeta)} \tag{3.64}$$

In equation (3.64), ζ angle is figured out using the law of sines.

$$\frac{GO_2}{\sin(\pi-\theta)} = \frac{O_1O_2}{\sin(\theta-\zeta)} \xrightarrow{yields}$$

$$\zeta = \theta + \frac{d\theta}{N-1}.(k-1) - \sin^{-1}\left(\frac{c}{r}.\sin\left(\pi - \theta - \frac{d\theta}{N-1}.(k-1)\right)\right) \tag{3.65}$$

k represents current discretized region number in an element (e.g. 2nd region in element N_1).

ψ^* for nose radius part is expressed as;

$$\psi^* = \frac{\pi}{2} - \kappa r + \varepsilon_r \tag{3.66}$$

ε_r is defined as angle between main cutting edge and current elements cutting edge on plane perpendicular to cutting velocity [55].

Second case, $a = r.(1 - \cos(\kappa r))$:

The only difference between the second case and the first case is that main cutting edge is not engaged with workpiece. Hence, forces are calculated using tool nose part formulations that are used in first case calculations.

Third case, $a < r.(1-\cos(\kappa r))$:

In this case, main cutting edge is not engaged with the workpiece (Figure 3-9). However, GO_1 calculation for element N_1 differs when compared to other elements.

For the area that is defined between θ_1 and θ_2,

$$\theta_1 = \sin^{-1}\left(\frac{r-a}{r}\right) \tag{3.67}$$

$$\theta_2 = \tan^{-1}\left(\frac{r-a}{r.\cos(\theta_1)-c}\right) \tag{3.68}$$

$$GO_1 = \frac{r-a}{\sin\left(\theta + \frac{d\theta}{N-1}.(k-1)\right)} \tag{3.69}$$

For engaged region that is defined beyond θ_2, nose part formulations of first case can be used.

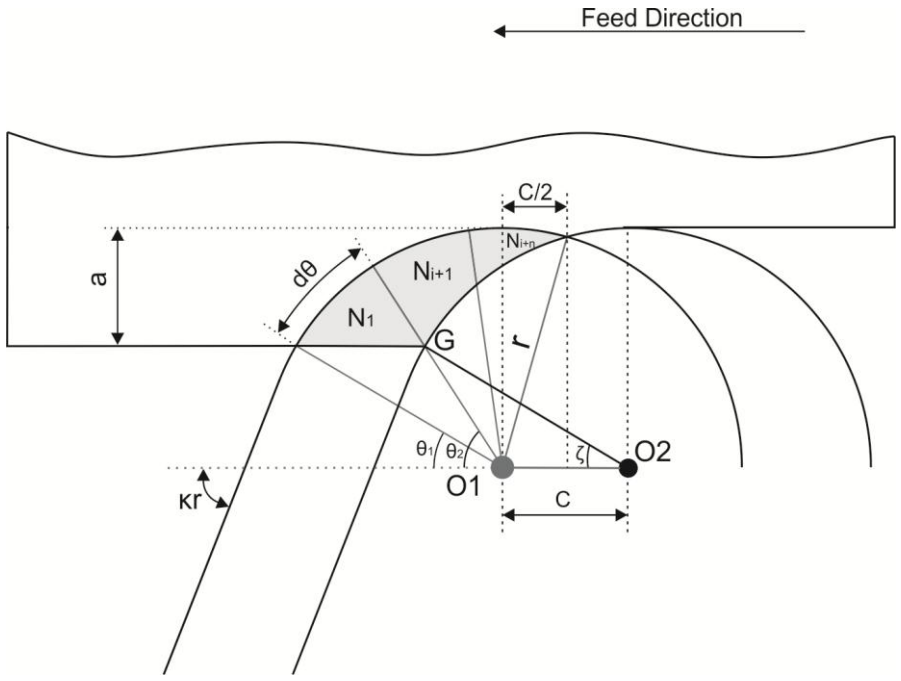

Figure 3-9 Schematic of a Turning Tool Engaged with a Workpiece When $\boldsymbol{a < r.(1 - \cos(kr))}$

After calculations, differential force components are transformed to cartesian coordinate frame. Then, total forces are figured out in x, y, z directions by summation of differential force components.

$$dFx = dF_{feed}.\sin\left(\psi^*\right) + dF_{radial}.\cos\left(\psi^*\right) \tag{3.70}$$

$$dFy = dF_{tangent} \tag{3.71}$$

$$dFz = dF_{feed}.\cos\left(\psi^*\right) - dF_{radial}.\sin\left(\psi^*\right) \tag{3.72}$$

$$Fx = \sum_{i=1}^{i=N_{main}} dFx_{main} + \sum_{j=1}^{j=N_{radial}} dFx \tag{3.73}$$

$$Fy = \sum_{i=1}^{i=N_{main}} dFy_{main} + \sum_{j=1}^{j=N_{radial}} dFy \tag{3.74}$$

$$Fz = \sum_{i=1}^{i=N_{main}} dFz_{main} + \sum_{j=1}^{j=N_{radial}} dFz \tag{3.75}$$

It should be noticed that depending on the engagement situation main cutting edge forces are taken in to account.

In temperature calculations, determination of tool chip contact locations is an important issue. In order that, finding a global chip flow direction is vital. However, each element along nose radius has different chip flow directions due to utilized approach in oblique cutting mechanics model. Therefore, frictional force vectors of all elements are summed in order to find a global chip flow direction.

$$F_I = \sum_{i=1}^{i=N_{main}+N_{radial}} \mathrm{F_{u,i}}.\cos(\eta_{c,i} + \varepsilon_{c,i}) \tag{3.76}$$

$$F_{II} = \sum_{i=1}^{i=N_{main}+N_{radial}} \mathrm{F_{u,i}}.\sin(\eta_{c,i} + \varepsilon_{c,i}) \tag{3.77}$$

$$\eta_{global} = \tan^{-1}(\frac{F_{II}}{F_I}) \tag{3.78}$$

ε_c is angle between main cutting edge and any other element in above equations; it is measured on rake face [55].

$$\varepsilon_c = \cot^{-1}(\cos(\alpha_n).\sec(\lambda_s).(\cot(\varepsilon_r) - \sin(\lambda_s).\tan(\alpha_n))) \tag{3.79}$$

Chapter 4: Thermal Analysis

In this chapter, modelling of temperature fields in oblique machining is presented. Temperature field for tool, chip and workpiece is modelled using finite difference based approach. In presented approach, two heat sources are taken in to account. First one is due to shearing on shear plane. Second one is due to friction between tool and chip on rake face. Tool, chip and workpiece geometries are discretized in to multiple blocks in order to represent complex cutting geometry. Solutions are separately carried out for each block by considering boundary conditions between them. Then, repetitive solutions are continued until preset convergence criterion is met for all solution blocks.

4.1 Heat Balance Equations

Heat conduction analysis is performed in order to determine temperature fields. Initially, heat balance equations are written based on first law of thermodynamics at rate basis (equation (4.1)). Those equations are written for a control volume. Input heat rate values in x, y and z orthogonal directions are represented by using q_x, q_y, q_z terms. Output heat rate values at facing surfaces are represented by using q_{x+dx}, q_{y+dy}, q_{z+dz} terms. Schematic of a control volume can be seen in Figure 4-1.

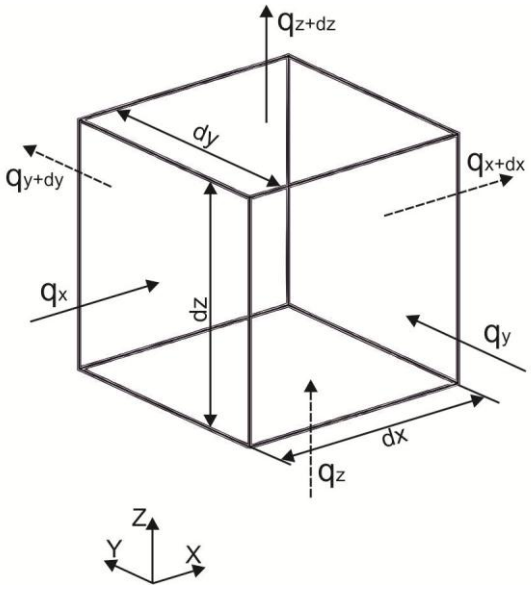

Figure 4-1 Schematic of a Control Volume in Cartesian Coordinates

$$\dot{E}_{in} + \dot{E}_{generated} - \dot{E}_{out} = \dot{E}_{stored} \tag{4.1}$$

Then, output flux terms are rewritten by utilizing taylor series expansion. Note that second and higher order terms are neglected.

$$q_{x+dx} = q_x + \frac{\delta q_x}{\delta x}.dx \tag{4.2}$$

$$q_{y+dy} = q_y + \frac{\delta q_y}{\delta y}.dy \tag{4.3}$$

$$q_{z+dz} = q_z + \frac{\delta q_z}{\delta z}.dz \tag{4.4}$$

Volumetric heat generation rate ($\dot{E}_{generated}$) is expressed as;

$$\dot{E}_{generated} = \dot{q}.dx.dy.dz \tag{4.5}$$

Stored energy ($\dot{E}_{stored}$) term is written by assuming that there is no phase change in solid medium.

$$\dot{E}_{stored} = \rho.C_p.\frac{\partial T}{\partial t}.dx.dy.dz \tag{4.6}$$

After definition of the above expressions first law of thermodynamics is written in following form;

$$\begin{aligned} & q_x + q_y + q_z - q_{x+dx} - q_{y+dy} - q_{z+dz} + \dot{q}.dx.dy.dz = \rho.C_p.\frac{\partial T}{\partial t}.dx.dy.dz \\ & \overset{yields}{\rightarrow} \quad -\frac{\delta q_x}{\delta x}.dx - \frac{\delta q_y}{\delta y}.dy - \frac{\delta q_z}{\delta z}.dz + \dot{q}.dx.dy.dz = \rho.C_p.\frac{\partial T}{\partial t}.dx.dy.dz \end{aligned} \tag{4.7}$$

For an inner control volume element, equation (4.7) can be rewritten by introducing Fourier's law for heat rate expressions. Note that heat conduction is assumed constant and equal in all directions. In addition, heat conduction coefficient change with temperature is neglected in the analyses.

$$q_x = -k.\frac{\partial T}{\partial x}.dy.dz \tag{4.8}$$

$$q_y = -k.\frac{\partial T}{\partial y}.dx.dz \tag{4.9}$$

$$q_z = -k.\frac{\partial T}{\partial z}.dx.dy \tag{4.10}$$

$$\frac{\delta^2 T}{\delta x^2} + \frac{\delta^2 T}{\delta y^2} + \frac{\delta^2 T}{\delta z^2} + \frac{\dot{q}}{k} = \frac{\rho.C_p}{k}.\frac{\partial T}{\partial t} \tag{4.11}$$

4.2 Transformation of Heat Transfer Equations

Mathematical modelling of a physical problem is developed using basic principles of heat transfer. Formulations are derived according to assumptions that are related to physical problem. In the proposed heat transfer problem, mathematical modelling leads to a partial differential equation system. In order to solve that system in equation (4.11), a numerical solution method is utilized; because analytical solution is not possible due to complexity of geometry. Among numerical methods, there are

possible methods such as finite difference and finite element method. In this study, finite difference method is utilized. It is a powerful method for solving heat transfer equations. In this method, solution domain is discretized in to finite number of control volumes and temperature values are calculated for those volumes. Partial differential equations turn in to algebraic equations using finite difference approximations.

Normally, finite difference approximations require a rectangular computational domain and it is straight forward to derive finite difference equations for physically rectangular domains. However, oblique cutting process has a complicated geometry. Therefore, derivation of numerical approximations is cumbersome for complex geometries due to unequally spaced grid distribution and non-uniform boundaries. Furthermore, application of boundary conditions becomes problematic in this case. In order to overcome the problems related to geometric complexity, physical space is transformed into rectangular computational space. This transformation is carried out by using a generalized coordinate system for computational space [56].

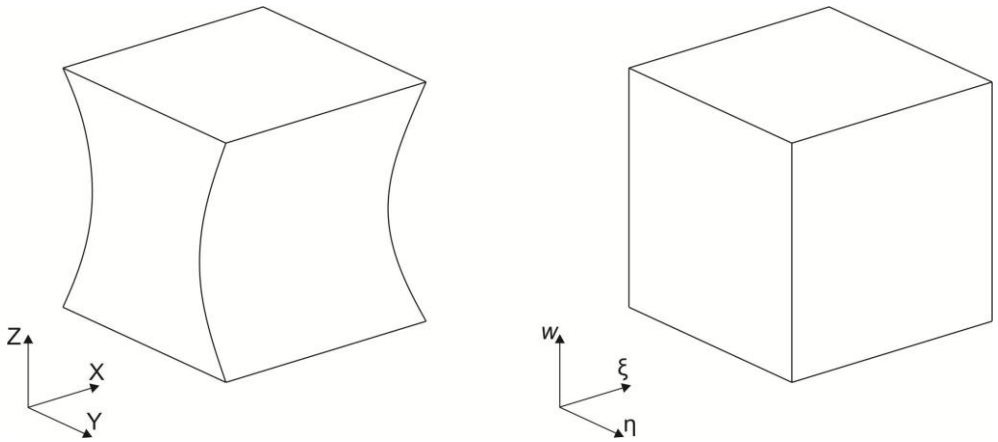

Figure 4-2 Physical (left hand side) and Computational (right hand side) Domains

Interrelation between physical and computational spaces can be defined using following expressions;

$$\epsilon = \epsilon(x, y, z)$$

$$n = n(x, y, z)$$

$$w = w(x, y, z)$$

Note that after transformation partial differential equation type stays same as original partial differential equation in physical space. Heat balance equation in Cartesian coordinates (equation (4.11)) is transformed into computational space in equation (4.18) by using following expressions;

$$\frac{\partial \epsilon}{\partial x} = \epsilon_x, \frac{\partial \epsilon}{\partial y} = \epsilon_y, \frac{\partial \epsilon}{\partial z} = \epsilon_z, \frac{\partial^2 \epsilon}{\partial x^2} = \epsilon_{xx}, \frac{\partial^2 \epsilon}{\partial y^2} = \epsilon_{yy}, \frac{\partial^2 \epsilon}{\partial z^2} = \epsilon_{zz}$$

$$, \frac{\partial n}{\partial x} = n_x, \frac{\partial n}{\partial y} = n_y, \frac{\partial n}{\partial z} = n_z, \frac{\partial^2 n}{\partial x^2} = n_{xx}, \frac{\partial^2 n}{\partial y^2} = n_{yy}, \frac{\partial^2 n}{\partial z^2} = n_{zz},$$

$$\frac{\partial w}{\partial x} = w_x, \frac{\partial w}{\partial y} = w_y, \frac{\partial w}{\partial z} = w_z, \frac{\partial^2 w}{\partial x^2} = w_{xx}, \frac{\partial^2 w}{\partial y^2} = w_{yy}, \frac{\partial^2 w}{\partial z^2} = w_{zz}$$

$$\frac{\partial^2 T}{\partial x^2} = \frac{\partial^2 T}{\partial n^2}.\left(n_x\right)^2 + 2.\frac{\partial^2 T}{\partial n.\partial w}.n_x.w_x + \frac{\partial^2 T}{\partial w^2}.\left(w_x\right)^2 + 2.\frac{\partial^2 T}{\partial \epsilon.\partial w}.\epsilon_x.w_x + 2.\frac{\partial^2 T}{\partial \epsilon.\partial n}.\epsilon_x.n_x + \frac{\partial T}{\partial \epsilon}.\epsilon_{xx} + \frac{\partial T}{\partial n}.n_{xx} + \frac{\partial T}{\partial w}.w_{xx} + \frac{\partial^2 T}{\partial \epsilon^2}.\left(\epsilon_x\right)^2 \quad (4.12)$$

$$\frac{\partial^2 T}{\partial y^2} = \frac{\partial^2 T}{\partial n^2}.\left(n_y\right)^2 + 2.\frac{\partial^2 T}{\partial n.\partial w}.n_y.w_y + \frac{\partial^2 T}{\partial w^2}.\left(w_y\right)^2 + 2.\frac{\partial^2 T}{\partial \epsilon.\partial w}.\epsilon_y.w_y + 2.\frac{\partial^2 T}{\partial \epsilon.\partial n}.\epsilon_y.n_y + \frac{\partial T}{\partial \epsilon}.\epsilon_{yy} + \frac{\partial T}{\partial n}.n_{yy} + \frac{\partial T}{\partial w}.w_{yy} + \frac{\partial^2 T}{\partial \epsilon^2}.\left(\epsilon_y\right)^2 \quad (4.13)$$

$$\frac{\partial^2 T}{\partial z^2} = \frac{\partial^2 T}{\partial n^2}.\left(n_z\right)^2 + 2.\frac{\partial^2 T}{\partial n.\partial w}.n_z.w_z + \frac{\partial^2 T}{\partial w^2}.\left(w_z\right)^2 + 2.\frac{\partial^2 T}{\partial \epsilon.\partial w}.\epsilon_z.w_z + 2.\frac{\partial^2 T}{\partial \epsilon.\partial n}.\epsilon_z.n_z + \frac{\partial T}{\partial \epsilon}.\epsilon_{zz} + \frac{\partial T}{\partial n}.n_{zz} + \frac{\partial T}{\partial w}.w_{zz} + \frac{\partial^2 T}{\partial \epsilon^2}.\left(\epsilon_z\right)^2 \quad (4.14)$$

$$\frac{\partial T}{\partial x} = \frac{\partial T}{\partial \epsilon}.\epsilon_x + \frac{\partial T}{\partial n}.n_x + \frac{\partial T}{\partial w}.w_x \quad (4.15)$$

$$\frac{\partial T}{\partial y} = \frac{\partial T}{\partial \epsilon}.\epsilon_y + \frac{\partial T}{\partial n}.n_y + \frac{\partial T}{\partial w}.w_y \quad (4.16)$$

$$\frac{\partial T}{\partial z}=\frac{\partial T}{\partial \epsilon}.\epsilon_z+\frac{\partial T}{\partial n}.n_z+\frac{\partial T}{\partial w}.w_z \tag{4.17}$$

$$\begin{aligned}
&\frac{\partial^2 T}{\partial n^2}.\left(n_x\right)^2+2.\frac{\partial^2 T}{\partial n.\partial w}.n_x.w_x+\frac{\partial^2 T}{\partial w^2}.\left(w_x\right)^2+2.\frac{\partial^2 T}{\partial \epsilon.\partial w}.\epsilon_x.w_x+2.\frac{\partial^2 T}{\partial \epsilon.\partial n}.\epsilon_x.n_x+\\
&\frac{\partial T}{\partial \epsilon}.\epsilon_{xx}+\frac{\partial T}{\partial n}.n_{xx}+\frac{\partial T}{\partial w}.w_{xx}+\frac{\partial^2 T}{\partial \epsilon^2}.\left(\epsilon_x\right)^2+\frac{\partial^2 T}{\partial n^2}.\left(n_y\right)^2+2.\frac{\partial^2 T}{\partial n.\partial w}.n_y.w_y+\\
&\frac{\partial^2 T}{\partial w^2}.\left(w_y\right)^2+2.\frac{\partial^2 T}{\partial \epsilon.\partial w}.\epsilon_y.w_y+2.\frac{\partial^2 T}{\partial \epsilon.\partial n}.\epsilon_y.n_y+\frac{\partial T}{\partial \epsilon}.\epsilon_{yy}+\frac{\partial T}{\partial n}.n_{yy}+\\
&\frac{\partial T}{\partial w}.w_{yy}+\frac{\partial^2 T}{\partial \epsilon^2}.\left(\epsilon_y\right)^2+\frac{\partial^2 T}{\partial n^2}.\left(n_z\right)^2+2.\frac{\partial^2 T}{\partial n.\partial w}.n_z.w_z+\frac{\partial^2 T}{\partial w^2}.\left(w_z\right)^2+\\
&2.\frac{\partial^2 T}{\partial \epsilon.\partial w}.\epsilon_z.w_z+2.\frac{\partial^2 T}{\partial \epsilon.\partial n}.\epsilon_z.n_z+\frac{\partial T}{\partial \epsilon}.\epsilon_{zz}+\frac{\partial T}{\partial n}.n_{zz}+\frac{\partial T}{\partial w}.w_{zz}+\frac{\partial^2 T}{\partial \epsilon^2}.\left(\epsilon_z\right)^2+\\
&\frac{\dot{q}}{k}=\frac{\rho.C_p}{k}.\begin{bmatrix}\left(\frac{\partial T}{\partial \epsilon}.\epsilon_x+\frac{\partial T}{\partial n}.n_x+\frac{\partial T}{\partial w}.w_x\right).\frac{\partial x}{\partial t}+\\ \left(\frac{\partial T}{\partial \epsilon}.\epsilon_y+\frac{\partial T}{\partial n}.n_y+\frac{\partial T}{\partial w}.w_y\right).\frac{\partial y}{\partial t}+\\ \left(\frac{\partial T}{\partial \epsilon}.\epsilon_z+\frac{\partial T}{\partial n}.n_z+\frac{\partial T}{\partial w}.w_z\right).\frac{\partial z}{\partial t}\end{bmatrix}
\end{aligned} \tag{4.18}$$

As can be seen from above expressions, there is trade off regarding the resulting equations complexity as a result of transformations. It should be noticed that time derivative of temperature is written based on velocities in equation (4.18); in order to simplify the numerical solution procedure. Some of those terms correspond to chip and cutting velocity in simulations of chip and workpiece.

All transformations are derived for three dimensional cases in order to constitute a base for structured grid generation in the future. However, two dimensional grid structuring is found adequate for creating rectangular computational domain in this thesis. In order to solve heat balance equation, derivative terms should be identified.

$$\begin{bmatrix}d\epsilon\\ dn\end{bmatrix}=\begin{bmatrix}\epsilon_x & \epsilon_y\\ n_x & n_y\end{bmatrix}.\begin{bmatrix}dx\\ dy\end{bmatrix} \tag{4.19}$$

$$\begin{bmatrix} dx \\ dy \end{bmatrix} = \begin{bmatrix} x_\epsilon & x_n \\ y_\epsilon & y_n \end{bmatrix} . \begin{bmatrix} d\epsilon \\ dn \end{bmatrix} \tag{4.20}$$

According to equations, (4.19) and (4.20) derivative terms can be identified as follows;

$$\epsilon_x = J . y_n \tag{4.21}$$

$$n_x = -J . y_\epsilon \tag{4.22}$$

$$\epsilon_y = -J . x_n \tag{4.23}$$

$$n_y = J . x_\epsilon \tag{4.24}$$

J term is called Jacobian of the transformation. Depending on the situation, it can be defined as ratio of areas in computational space to physical space (in two dimensional case) or ratio of volumes in computational space to physical space (in three dimensional case).

$$J = \left(det \begin{bmatrix} x_\epsilon & x_n \\ y_\epsilon & y_n \end{bmatrix} \right)^{-1} = \frac{1}{y_n . x_\epsilon - x_n . y_\epsilon} \tag{4.25}$$

Second order derivative terms for transformed domain are identified by simply taking derivatives of the above first order expressions.

$$\epsilon_{xx} = \epsilon_x . \frac{\partial \epsilon_x}{\partial \epsilon} + n_x . \frac{\partial \epsilon_x}{\partial n} \tag{4.26}$$

$$n_{xx} = \epsilon_x . \frac{\partial n_x}{\partial \epsilon} + n_x . \frac{\partial n_x}{\partial n} \tag{4.27}$$

$$\epsilon_{yy} = \epsilon_y . \frac{\partial \epsilon_y}{\partial \epsilon} + n_y . \frac{\partial \epsilon_y}{\partial n} \tag{4.28}$$

$$n_{yy} = \epsilon_y . \frac{\partial n_y}{\partial \epsilon} + n_y . \frac{\partial n_y}{\partial n} \tag{4.29}$$

As can be seen from the above expressions, derivative terms for computational space are identified by using physical space coordinates. Generation of coordinates in physical space is discussed in "Grid Generation Procedure" section.

4.3 Grid Generation Procedure

Grid generation is an essential step in numerical solution of differential equations. Proper grid generation affects solution quality and accuracy. There are two main groups of grid generation techniques. First group is structured grid generation and the second one is unstructured grid generation. These two groups are differed at grid point organization. In structured grids, distribution of grid points is determined according to a general rule. In unstructured grids, connection between grid points differs from point to point. Both grid generation groups contain various subgroups and methods which have their own advantages and disadvantages. However this is out of scope of this thesis. Further information about grid generation can be found in literature [57], [58].

In the presented modelling approach, elliptic grid generation method is utilized for discretizing the physical domain. This method is classified as a structured grid generation method. In this method, a differential equation system is solved in order to figure out grid point locations in physical space. Using elliptic equation system results in smooth grid patterns. Moreover, transformation between physical and computational space is one to one. Lastly, elliptic grid generation method allows selecting boundary coordinate points [57].

Physical space coordinates are determined by solving two differential equations in form of Laplace's equation. First, grid points on boundaries are specified. Then, differential equation system is solved to find interior grid point locations. In order to generate grids following equation system is solved;

$$\epsilon_{xx} + \epsilon_{yy} = 0 \tag{4.30}$$

$$n_{xx} + n_{yy} = 0 \tag{4.31}$$

Above equations is rewritten using expressions (4.21) to (4.24) and (4.26) to (4.29). Equation (4.30) becomes;

$$J^3.\left(x_n.\left(a.y_{\epsilon\epsilon}-2.b.y_{\epsilon n}+c.y_{nn}\right)-y_n.\left(a.x_{\epsilon\epsilon}-2.b.x_{\epsilon n}+c.x_{nn}\right)\right)=0 \tag{4.32}$$

Equation (4.31) becomes;

$$J^3.\left(y_\epsilon.\left(a.x_{\epsilon\epsilon}-2.b.x_{\epsilon n}+c.x_{nn}\right)-x_\epsilon.\left(a.y_{\epsilon\epsilon}-2.b.y_{\epsilon n}+c.y_{nn}\right)\right)=0 \tag{4.33}$$

Where;

$$a=x^2{}_n+y^2{}_n \tag{4.34}$$

$$b=x_\epsilon.x_n+y_\epsilon.y_n \tag{4.35}$$

$$c=x^2{}_\epsilon+y^2{}_\epsilon \tag{4.36}$$

Further simplification results in following two equations;

$$a.y_{\epsilon\epsilon}-2.b.y_{\epsilon n}+c.y_{nn}=0 \tag{4.37}$$

$$a.x_{\epsilon\epsilon}-2.b.x_{\epsilon n}+c.x_{nn}=0 \tag{4.38}$$

Physical space coordinates are found by iteratively solving equations (4.37) and (4.38). Finite difference approach is utilized in order to solve the equation system. If equations (4.37) and (4.38) are rewritten by applying finite difference approximations to derivative terms, they take the following form;

$$\begin{aligned} &a.\frac{y(i+1,j)-2.y(i,j)+y(i-1,j)}{\Delta\epsilon^2}- \\ &b.\frac{y(i-1,j-1)-y(i-1,j+1)-y(i+1,j-1)+y(i+1,j+1)}{2.\Delta\epsilon.\Delta n}+ \\ &c.\frac{y(i,j+1)-2.y(i,j)+y(i,j-1)}{\Delta n^2}=0 \end{aligned} \tag{4.39}$$

$$a.\frac{x(i+1,j)-2.x(i,j)+x(i-1,j)}{\Delta\epsilon^2}- \\ b.\frac{x(i-1,j-1)-x(i-1,j+1)-x(i+1,j-1)+x(i+1,j+1)}{2.\Delta\epsilon.\Delta n}+ \\ c.\frac{x(i,j+1)-2.x(i,j)+x(i,j-1)}{\Delta n^2}=0 \tag{4.40}$$

Coefficients in (4.39) and (4.40) are listed below;

$$a=\left(\frac{x(i,j+1)-x(i,j-1)}{2.\Delta n}\right)^2+\left(\frac{y(i,j+1)-y(i,j-1)}{2.\Delta n}\right)^2 \tag{4.41}$$

$$b=\frac{x(i+1,j)-x(i-1,j)}{2.\Delta\epsilon}.\frac{x(i,j+1)-x(i,j-1)}{2.\Delta n}+ \\ \frac{y(i+1,j)-y(i-1,j)}{2.\Delta\epsilon}.\frac{y(i,j+1)-y(i,j-1)}{2.\Delta n} \tag{4.42}$$

$$c=\left(\frac{x(i+1,j)-x(i-1,j)}{2.\Delta\epsilon}\right)^2+\left(\frac{y(i+1,j)-y(i-1,j)}{2.\Delta\epsilon}\right)^2 \tag{4.43}$$

Since finite differences method is employed in grid point solution, initial physical coordinates should be supplied in order to start the solution procedure. Note that physical coordinates of boundary nodes stay unchanged during the solution procedure. In solutions, a, b, c coefficients are determined by using grid points that are calculated in the previous iteration cycle. Iterations are carried on until convergence criterion is met for both x and y coordinates. Sum of absolute difference between successive iteration results is selected as convergence criterion (equation (4.44) and (4.45)) [56].

$$DIFF_x=\sum_{i=1,\,j=1}^{i=Nx+1,\,j=Ny+1} abs[x^{k+1}(i,j)-x^k(i,j)] \tag{4.44}$$

$$DIFF_y=\sum_{i=1,\,j=1}^{i=Nx+1,\,j=Ny+1} abs[y^{k+1}(i,j)-y^k(i,j)] \tag{4.45}$$

k value in equations (4.44) and (4.45) represents iteration number.

4.4 Discretization of the Heat balance Equations

Discretization of heat balance equations is an important fundamental step in solution procedure. In former section, identification of differential operators is presented. In current section, discretized form of equation (4.18) is derived by utilizing volume integrals for each infinitesimal control volume. Since solution is carried out in computational domain, derivations are made for fictitious volumetric element. This procedure is also named as finite volume approach [59].

In finite volume approach, heat balance equation is brought in to a form which is applicable to volume in space. Every nodal point in generated mesh represents a control volume in this approach. Control volume size may change depending on position of the nodes (corner node, side wall node etc.). However, control volumes should not be overlapping. Derivations of the equations are accomplished by integrating heat balance equation in computational space for each control volume. Note that conservation law applies to any control volume shape and there is no assumptions regarding to control volume shape. Thus, volumetric approach is also applicable to unstructured meshes from this point of view.

Finite difference form of heat balance equation for an internal node is presented here to exemplify the procedure. Derivations for corner nodes, side walls and side lines are not included here; because, procedure is same for those nodes with slight differences. For an internal grid point finite volume representation is written as follows;

$$\int_{k-\frac{1}{2}}^{k+\frac{1}{2}}\int_{j-\frac{1}{2}}^{j+\frac{1}{2}}\int_{i-\frac{1}{2}}^{i+\frac{1}{2}}\frac{\partial^2 T}{\partial n^2}.\left(n_x\right)^2.d\epsilon.dn.dw+\int_{k-\frac{1}{2}}^{k+\frac{1}{2}}\int_{j-\frac{1}{2}}^{j+\frac{1}{2}}\int_{i-\frac{1}{2}}^{i+\frac{1}{2}}\frac{\partial^2 T}{\partial w^2}.\left(w_x\right)^2.d\epsilon.dn.dw+$$

$$\int_{k-\frac{1}{2}}^{k+\frac{1}{2}}\int_{j-\frac{1}{2}}^{j+\frac{1}{2}}\int_{i-\frac{1}{2}}^{i+\frac{1}{2}}2.\frac{\partial^2 T}{\partial\epsilon.\partial w}.\epsilon_x.w_x.d\epsilon.dn.dw+\int_{k-\frac{1}{2}}^{k+\frac{1}{2}}\int_{j-\frac{1}{2}}^{j+\frac{1}{2}}\int_{i-\frac{1}{2}}^{i+\frac{1}{2}}\frac{\partial T}{\partial\epsilon}.\epsilon_{xx}.d\epsilon.dn.dw+\int_{k-\frac{1}{2}}^{k+\frac{1}{2}}\int_{j-\frac{1}{2}}^{j+\frac{1}{2}}\int_{i-\frac{1}{2}}^{i+\frac{1}{2}}\frac{\partial T}{\partial n}.n_{xx}.d\epsilon.dn.dw+$$

$$\int_{k-\frac{1}{2}}^{k+\frac{1}{2}}\int_{j-\frac{1}{2}}^{j+\frac{1}{2}}\int_{i-\frac{1}{2}}^{i+\frac{1}{2}}\frac{\partial T}{\partial w}.w_{xx}.d\epsilon.dn.dw+\int_{k-\frac{1}{2}}^{k+\frac{1}{2}}\int_{j-\frac{1}{2}}^{j+\frac{1}{2}}\int_{i-\frac{1}{2}}^{i+\frac{1}{2}}\frac{\partial^2 T}{\partial\epsilon^2}.\left(\epsilon_x\right)^2.d\epsilon.dn.dw+\int_{k-\frac{1}{2}}^{k+\frac{1}{2}}\int_{j-\frac{1}{2}}^{j+\frac{1}{2}}\int_{i-\frac{1}{2}}^{i+\frac{1}{2}}\frac{\partial^2 T}{\partial n^2}.\left(n_y\right)^2.d\epsilon.dn.dw+$$

$$\int_{k-\frac{1}{2}}^{k+\frac{1}{2}}\int_{j-\frac{1}{2}}^{j+\frac{1}{2}}\int_{i-\frac{1}{2}}^{i+\frac{1}{2}}2.\frac{\partial^2 T}{\partial n.\partial w}.n_y.w_y.d\epsilon.dn.dw+\int_{k-\frac{1}{2}}^{k+\frac{1}{2}}\int_{j-\frac{1}{2}}^{j+\frac{1}{2}}\int_{i-\frac{1}{2}}^{i+\frac{1}{2}}\frac{\partial^2 T}{\partial w^2}.\left(w_y\right)^2.d\epsilon.dn.dw+$$

$$\int_{k-\frac{1}{2}}^{k+\frac{1}{2}}\int_{j-\frac{1}{2}}^{j+\frac{1}{2}}\int_{i-\frac{1}{2}}^{i+\frac{1}{2}}2.\frac{\partial^2 T}{\partial\epsilon.\partial n}.\epsilon_y.n_y.d\epsilon.dn.dw+\int_{k-\frac{1}{2}}^{k+\frac{1}{2}}\int_{j-\frac{1}{2}}^{j+\frac{1}{2}}\int_{i-\frac{1}{2}}^{i+\frac{1}{2}}\frac{\partial T}{\partial\epsilon}.\epsilon_{yy}.d\epsilon.dn.dw+\int_{k-\frac{1}{2}}^{k+\frac{1}{2}}\int_{j-\frac{1}{2}}^{j+\frac{1}{2}}\int_{i-\frac{1}{2}}^{i+\frac{1}{2}}\frac{\partial T}{\partial n}.n_{yy}.d\epsilon.dn.dw+$$

$$\int_{k-\frac{1}{2}}^{k+\frac{1}{2}}\int_{j-\frac{1}{2}}^{j+\frac{1}{2}}\int_{i-\frac{1}{2}}^{i+\frac{1}{2}}\frac{\partial T}{\partial w}.w_{yy}.d\epsilon.dn.dw+\int_{k-\frac{1}{2}}^{k+\frac{1}{2}}\int_{j-\frac{1}{2}}^{j+\frac{1}{2}}\int_{i-\frac{1}{2}}^{i+\frac{1}{2}}\frac{\partial^2 T}{\partial\epsilon^2}.\left(\epsilon_y\right)^2.d\epsilon.dn.dw+\int_{k-\frac{1}{2}}^{k+\frac{1}{2}}\int_{j-\frac{1}{2}}^{j+\frac{1}{2}}\int_{i-\frac{1}{2}}^{i+\frac{1}{2}}\frac{\partial^2 T}{\partial n^2}.\left(n_z\right)^2.d\epsilon.dn.dw+$$

$$\int_{k-\frac{1}{2}}^{k+\frac{1}{2}}\int_{j-\frac{1}{2}}^{j+\frac{1}{2}}\int_{i-\frac{1}{2}}^{i+\frac{1}{2}}2.\frac{\partial^2 T}{\partial n.\partial w}.n_z.w_z.d\epsilon.dn.dw+\int_{k-\frac{1}{2}}^{k+\frac{1}{2}}\int_{j-\frac{1}{2}}^{j+\frac{1}{2}}\int_{i-\frac{1}{2}}^{i+\frac{1}{2}}\frac{\partial^2 T}{\partial w^2}.\left(w_z\right)^2.d\epsilon.dn.dw+$$

$$\int_{k-\frac{1}{2}}^{k+\frac{1}{2}}\int_{j-\frac{1}{2}}^{j+\frac{1}{2}}\int_{i-\frac{1}{2}}^{i+\frac{1}{2}}2.\frac{\partial^2 T}{\partial\epsilon.\partial w}.\epsilon_z.w_z.d\epsilon.dn.dw+\int_{k-\frac{1}{2}}^{k+\frac{1}{2}}\int_{j-\frac{1}{2}}^{j+\frac{1}{2}}\int_{i-\frac{1}{2}}^{i+\frac{1}{2}}2.\frac{\partial^2 T}{\partial\epsilon.\partial n}.\epsilon_z.n_z.d\epsilon.dn.dw+$$

$$\int_{k-\frac{1}{2}}^{k+\frac{1}{2}}\int_{j-\frac{1}{2}}^{j+\frac{1}{2}}\int_{i-\frac{1}{2}}^{i+\frac{1}{2}}\frac{\partial T}{\partial\epsilon}.\epsilon_{zz}.d\epsilon.dn.dw+\int_{k-\frac{1}{2}}^{k+\frac{1}{2}}\int_{j-\frac{1}{2}}^{j+\frac{1}{2}}\int_{i-\frac{1}{2}}^{i+\frac{1}{2}}\frac{\partial T}{\partial n}.n_{zz}.d\epsilon.dn.dw+\int_{k-\frac{1}{2}}^{k+\frac{1}{2}}\int_{j-\frac{1}{2}}^{j+\frac{1}{2}}\int_{i-\frac{1}{2}}^{i+\frac{1}{2}}\frac{\partial T}{\partial w}.w_{zz}.d\epsilon.dn.dw+$$

$$\int_{k-\frac{1}{2}}^{k+\frac{1}{2}}\int_{j-\frac{1}{2}}^{j+\frac{1}{2}}\int_{i-\frac{1}{2}}^{i+\frac{1}{2}}\frac{\partial^2 T}{\partial\epsilon^2}.\left(\epsilon_z\right)^2.d\epsilon.dn.dw+\frac{\dot{q}}{k}=$$

$$\frac{\rho.C_p}{k}.\left[\begin{array}{l}\left(\int_{k-\frac{1}{2}}^{k+\frac{1}{2}}\int_{j-\frac{1}{2}}^{j+\frac{1}{2}}\int_{i-\frac{1}{2}}^{i+\frac{1}{2}}\frac{\partial T}{\partial\epsilon}.\epsilon_x.d\epsilon.dn.dw+\int_{k-\frac{1}{2}}^{k+\frac{1}{2}}\int_{j-\frac{1}{2}}^{j+\frac{1}{2}}\int_{i-\frac{1}{2}}^{i+\frac{1}{2}}\frac{\partial T}{\partial n}.n_x.d\epsilon.dn.dw+\int_{k-\frac{1}{2}}^{k+\frac{1}{2}}\int_{j-\frac{1}{2}}^{j+\frac{1}{2}}\int_{i-\frac{1}{2}}^{i+\frac{1}{2}}\frac{\partial T}{\partial w}.w_x.d\epsilon.dn.dw\right).\frac{\partial x}{\partial t}+\\ \left(\int_{k-\frac{1}{2}}^{k+\frac{1}{2}}\int_{j-\frac{1}{2}}^{j+\frac{1}{2}}\int_{i-\frac{1}{2}}^{i+\frac{1}{2}}\frac{\partial T}{\partial\epsilon}.\epsilon_y.d\epsilon.dn.dw+\int_{k-\frac{1}{2}}^{k+\frac{1}{2}}\int_{j-\frac{1}{2}}^{j+\frac{1}{2}}\int_{i-\frac{1}{2}}^{i+\frac{1}{2}}\frac{\partial T}{\partial n}.n_y.d\epsilon.dn.dw+\int_{k-\frac{1}{2}}^{k+\frac{1}{2}}\int_{j-\frac{1}{2}}^{j+\frac{1}{2}}\int_{i-\frac{1}{2}}^{i+\frac{1}{2}}\frac{\partial T}{\partial w}.w_y.d\epsilon.dn.dw\right).\frac{\partial y}{\partial t}\\ +\left(\int_{k-\frac{1}{2}}^{k+\frac{1}{2}}\int_{j-\frac{1}{2}}^{j+\frac{1}{2}}\int_{i-\frac{1}{2}}^{i+\frac{1}{2}}\frac{\partial T}{\partial\epsilon}.\epsilon_z.d\epsilon.dn.dw+\int_{k-\frac{1}{2}}^{k+\frac{1}{2}}\int_{j-\frac{1}{2}}^{j+\frac{1}{2}}\int_{i-\frac{1}{2}}^{i+\frac{1}{2}}\frac{\partial T}{\partial n}.n_z.d\epsilon.dn.dw+\int_{k-\frac{1}{2}}^{k+\frac{1}{2}}\int_{j-\frac{1}{2}}^{j+\frac{1}{2}}\int_{i-\frac{1}{2}}^{i+\frac{1}{2}}\frac{\partial T}{\partial w}.w_z.d\epsilon.dn.dw\right).\frac{\partial z}{\partial t}\end{array}\right] \quad (4.46)$$

$\pm\frac{1}{2}$ value in equation (4.46) represents half way between grid points. As pointed out before, control volumes are not over lapping. After defining integrals, resulting differential operators are extended to finite difference approximations. After simple manipulations, equations turn into following form;

$$
\begin{aligned}
&\frac{\Delta n.\Delta w.T(i-1,j,k).\begin{pmatrix}2.\epsilon_x^2+\epsilon_x.Hx.\Delta\epsilon-\epsilon_{xx}.\Delta\epsilon+2.\epsilon_y^2+\epsilon_y.Hy.\Delta\epsilon-\epsilon_{yy}.\Delta\epsilon+2.\epsilon_z^2\\+\epsilon_z.Hz.\Delta\epsilon-\epsilon_{zz}.\Delta\epsilon\end{pmatrix}}{2.\Delta\epsilon}+\\
&\frac{\Delta n.\Delta w.T(i+1,j,k).\begin{pmatrix}2.\epsilon_x^2-\epsilon_x.Hx.\Delta\epsilon+\epsilon_{xx}.\Delta\epsilon+2.\epsilon_y^2-\epsilon_y.Hy.\Delta\epsilon+\epsilon_{yy}.\Delta\epsilon+2.\epsilon_z^2\\-\epsilon_z.Hz.\Delta\epsilon+\epsilon_{zz}.\Delta\epsilon\end{pmatrix}}{2.\Delta\epsilon}-\\
&\frac{1}{\Delta\epsilon.\Delta n.\Delta w}.2.T(i,j,k).\begin{pmatrix}\epsilon_x^2.\Delta n^2.\Delta w^2+\epsilon_y^2.\Delta n^2.\Delta w^2+\epsilon_z^2.\Delta n^2.\Delta w^2+n_x^2.\Delta\epsilon^2.\Delta w^2+n_y^2.\Delta\epsilon^2.\Delta w^2\\+n_z^2.\Delta\epsilon^2.\Delta w^2+w_x^2.\Delta\epsilon^2.\Delta n^2+w_y^2.\Delta\epsilon^2.\Delta n^2+w_z^2.\Delta\epsilon^2.\Delta n^2\end{pmatrix}+\\
&\frac{1}{2}.\Delta w.T(i-1,j-1,k).(\epsilon_x.n_x+\epsilon_y.n_y+\epsilon_z.n_z)-\frac{1}{2}.\Delta w.T(i-1,j+1,w).(\epsilon_x.n_x+\epsilon_y.n_y+\epsilon_z.n_z)-\\
&\frac{1}{2}.\Delta w.T(i+1,j-1,k).(\epsilon_x.n_x+\epsilon_y.n_y+\epsilon_z.n_z)+\frac{1}{2}.\Delta w.T(i+1,j+1,k).(\epsilon_x.n_x+\epsilon_y.n_y+\epsilon_z.n_z)+\\
&\frac{1}{2}.\Delta n.T(i-1,j,k-1).(\epsilon_x.w_x+\epsilon_y.w_y+\epsilon_z.w_z)-\frac{1}{2}.\Delta n.T(i-1,j,k+1).(\epsilon_x.w_x+\epsilon_y.w_y+\epsilon_z.w_z)-\\
&\frac{1}{2}.\Delta n.T(i+1,j,k-1).(\epsilon_x.w_x+\epsilon_y.w_y+\epsilon_z.w_z)+\frac{1}{2}.\Delta n.T(i+1,j,k+1).(\epsilon_x.w_x+\epsilon_y.w_y+\epsilon_z.w_z)+\\
&\frac{\Delta\epsilon.\Delta w.T(i,j-1,k).\begin{pmatrix}Hx.n_x.\Delta n+Hy.n_y.\Delta n+Hz.n_z.\Delta n+2.n_x^2-n_{xx}.\Delta n+2.n_y^2\\-n_{yy}.\Delta n+2.n_z^2-n_{zz}.\Delta n\end{pmatrix}}{2\Delta n}+\\
&\frac{\Delta\epsilon.\Delta w.T(i,j+1,k)\begin{pmatrix}-Hx.n_x.\Delta n-Hy.n_y.\Delta n-Hz.n_z.\Delta n+2.n_x^2+n_{xx}.\Delta n+2.n_y^2\\+n_{yy}.\Delta n+2.n_z^2+n_{zz}.\Delta n\end{pmatrix}}{2\Delta n}+\\
&\frac{\Delta\epsilon.\Delta n.T(i,j,k-1).\begin{pmatrix}Hx.w_x.\Delta w+Hy.w_y.\Delta w+Hz.w_z.\Delta w+2.w_x^2-w_{xx}.\Delta w+2.w_y^2\\-w_{yy}.w\ \Delta w+2.w_z^2-w_{zz}.\Delta w\end{pmatrix}}{2.\Delta w}+\\
&\frac{\Delta\epsilon.\Delta n.T(i,j,k+1).\begin{pmatrix}-Hx.w_x.\Delta w-Hy.w_y.\Delta w-Hz.w_z.\Delta w+2.w_x^2+w_{xx}.\Delta w\\+2.w_y^2+w_{yy}.\Delta w+2.w_z^2+w_{zz}.\Delta w\end{pmatrix}}{2.\Delta w}+\\
&\frac{1}{2}.\Delta\epsilon.T(i,j-1,k-1).(n_x.w_x+n_y.w_y+n_z.w_z)-\frac{1}{2}.\Delta\epsilon.T(i,j-1,k+1).(n_x.w_x+n_y.w_y+n_z.w_z)-\\
&\frac{1}{2}.\Delta\epsilon.T(i,j+1,k-1).(n_x.w_x+n_y.w_y+n_z.w_z)+\frac{1}{2}.\Delta\epsilon.T(i,j+1,k+1).(n_x.w_x+n_y.w_y+n_z.w_z)=0
\end{aligned}
\tag{4.47}
$$

Where, Hx, Hy, Hz terms are expressed as;

$$Hx = \frac{V_x}{\alpha}, Hy = \frac{V_y}{\alpha}, Hz = \frac{V_z}{\alpha} \tag{4.48}$$

α in equation (4.48) represents thermal diffusivity. Some velocity terms become zero depending on the simulated part (workpiece and chip). Coordinate systems are selected to use only one velocity component. However, formulations are written in a general way for being more flexible.

4.5 Chip Temperature Model

In modelling of chip temperatures, whole chip is splitted into smaller parallel parts that are defined by local oblique cutting geometries. This splitting approach is chosen in order to simplify the mesh geometry. A complex geometry is represented with simpler subparts by this way and grid point calculation time becomes distinctly shorter when compared to meshing of entire geometry. Furthermore, this procedure allows parallel processing in different computer CPUs.

Creating chip segment and grid generation is the first step in chip formulations. Simplified geometry of a chip is showed in Figure 4-4. Coordinate system directions are showed in Figure 4-4. x direction is selected parallel to chip flow direction. y direction is selected perpendicular to chip flow direction. z direction is selected perpendicular to tool chip interface.

Chip geometry has two sides that are parallel to chip flow direction and these sides are in contact with neighbouring elements. A detail of sample layout of segments is shown in Figure 4-3. In calculations, temperature values from neighbouring faces are used as boundary condition and finite difference equations are written accordingly. Length of consecutive faces is taken equal for simplicity. Thus, element numbers along chip flow direction can be selected same for all chip parts.

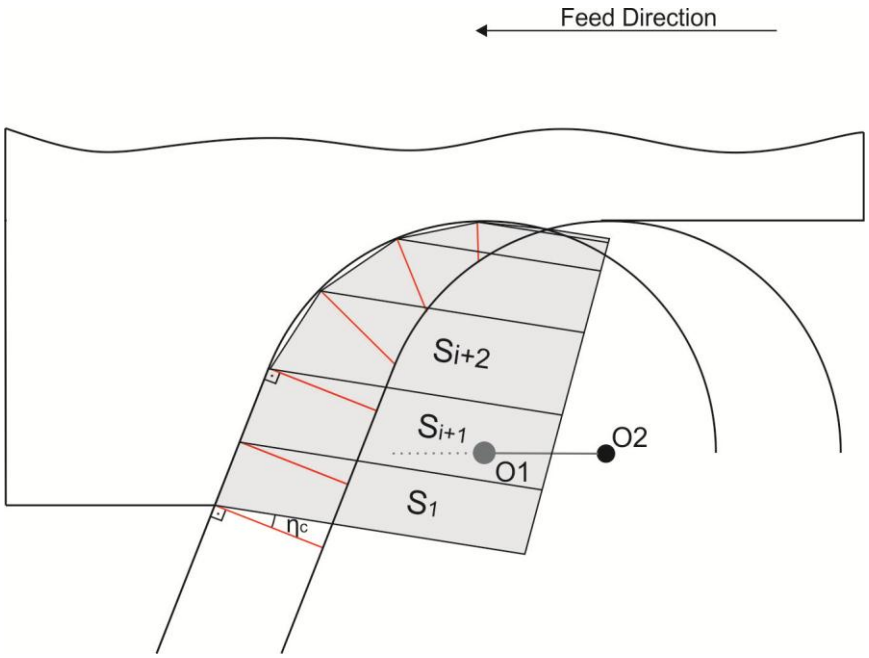

Figure 4-3 Layout of Chip Segments

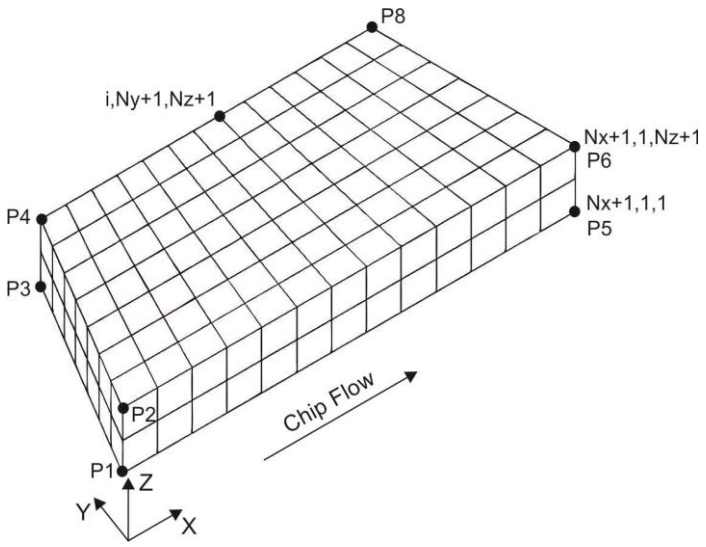

Figure 4-4 Simplified Schematic of a General Chip Part

Depending on the chip flow direction, two different type of chip segments are used in chip geometry creation. Section of them is seen in Figure 4-5. Chip geometries are

chosen with flat back face; because this geometry allows more stable grid generation. It reduces mesh skewness and probability of interferences in mesh.

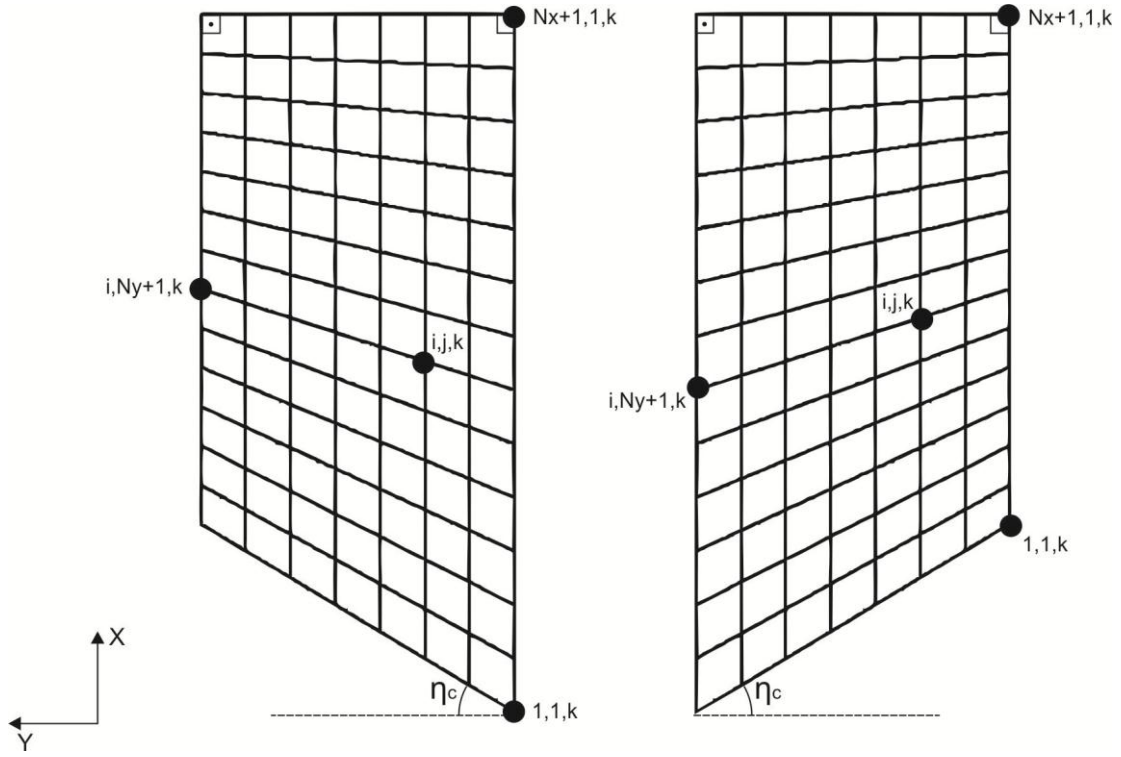

Figure 4-5 Top Face of a Chip Segment

Each chip part geometry is created by using local oblique cutting geometry. Distance between P1 and P3 is equal to differential cutting edge length for chip blocks that are engaged with main cutting edge. P1-P3 distance is equal to $|P3P4|_{tool}$ in Figure 4-7 for chip blocks that are engaged with nose radius part of tool. Distance between P1 and P2 is equal to chip thickness. Normally, chip thickness varies in each chip part; however, an average chip thickness value is used in calculations for simplicity. Segment length in x direction is defined with respect to neighbouring elements. First segment length is selected arbitrarily; consecutive segment lengths are calculated with respect to this value by using geometric interrelationship between segments.

Grid generation procedure is next step after defining the geometry. First, element numbers along x ,y, and z directions are determined as Nx, Ny and Nz. Then

according to these numbers, initial gird point distribution is supplied. After this step, new grid point positions are calculated by utilizing elliptic grid generation procedure. Note that element numbers in x direction is equal for all chip blocks.

Each part is modelled using three dimensional heat and one dimensional mass transfer. Heat loss due to convection and radiation is neglected in the analysis. Chip is assumed as a moving rigid body. As pointed out before, it is assumed that all chip parts are flowing in one direction and there is no movement perpendicular to chip flow direction. Thus, chip flow direction is selected as mass transfer direction. It should be noticed that time derivative of y and z are equal to zero in equation (4.18).

$$\frac{\partial y}{\partial t} = 0 \, and \, \frac{\partial z}{\partial t} = 0$$

Two heat sources are used in simulations. First heat source is due to friction between tool and chip. Second heat source is due to shearing on shear plane. Frictional heat flux is imposed to elements that are in contact with tool. Normally, contact length between tool and chip continuously changes along nose radius depending on the position. However, contact length for each segment is taken constant in utilized approach. Thus, increasing the number of elements along nose radius has positive effect on the approximation to real contact geometry. Note that uniform frictional heat generation is assumed. Finite difference formulation of flux terms is defined for boundary nodes as follows;

$$Q_{friction}(j,i) = w_z.\Delta\epsilon.\Delta n.\frac{P_{friction}(CN)}{k_{chip}.A_{contact}(CN)}.\left(1 - Bi\{TN\}(j,i)\right) \qquad (4.49)$$

$Bi\{TN\}(j,i)$ is proportion of frictional heat flux that flows in to tool. It is solved by carrying out an iterative solution. Solution procedure is discussed in latter section. TN denotes tool segment number. $A_{contact}$ is contact area between tool and chip. $P_{friction}(CN)$ is frictional power generated between tool and chip. CN in parenthesis denotes chip segment number.

Heat source from shear plane is incorporated in analysis by calculating average shear plane temperature. Then this value is used as boundary condition for points between P2 to P4. Average temperatures are calculated from Loewen and Shaw's model [6].

$$R = \left[1 + 1.328. \left(\frac{k.\gamma}{\rho.C_{workpiece}.V.h} \right)^{\frac{1}{2}} \right]^{-1} \tag{4.50}$$

$$T_{P2P4} = \frac{R.P_{shear}}{\rho.C_{workpiece}.V.h.b} + T_{room} \tag{4.51}$$

After defining heat generation terms and boundary conditions. Equilibrium equation (4.47) for all control volumes is written in compact form. Then, system of equations is solved for considered chip segment.

$$[A].[T_c] = [C] \tag{4.52}$$

In above equation, T_c is chip temperature array which is to be solved. A is square coefficient matrix and C is heat source array.

4.6 Tool Temperature Model

In modelling of tool temperatures, cutting edge is divided in to consecutive segments as in chip temperature modelling. Whole tool is not considered in the analysis. Engaged part of the tool and neighbouring parts are modelled. Layout of tool segments is presented in Figure 4-6. Each segment is created by using local geometric properties of the tool. Firstly, tool geometry is created and grid generation procedure is applied in order to start tool formulation. Then, equilibrium equations are written in discrete form for each node to begin solution.

Different kinds of simplified geometries are used in order to model tool shape. Rectangular blocks are used represent main cutting edge and secondary edge (left hand

side in Figure 4-7). Nose radius of the tool is modelled by using multiple linear edged segments (right hand side in Figure 4-7). Those geometries and coordinate directions are showed in Figure 4-7. y direction is along cutting edge. x direction is opposite to depth of cut motion. z direction is perpendicular to rake face. Lengths of consecutive tool faces are taken equal as in chip solution. This approach eases solution procedure. In addition, each chip segment has same length in z direction.

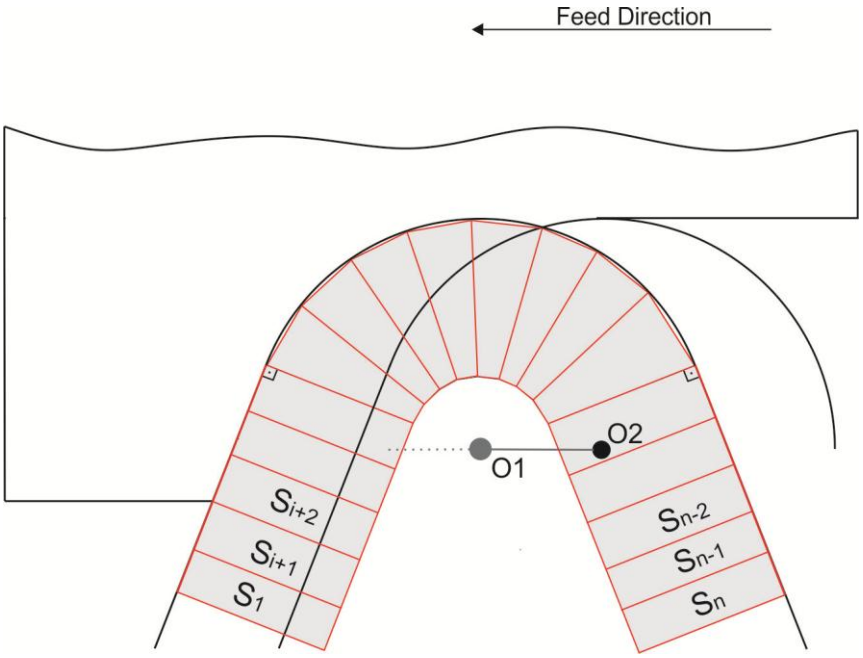

Figure 4-6 Layout of Tool Segments

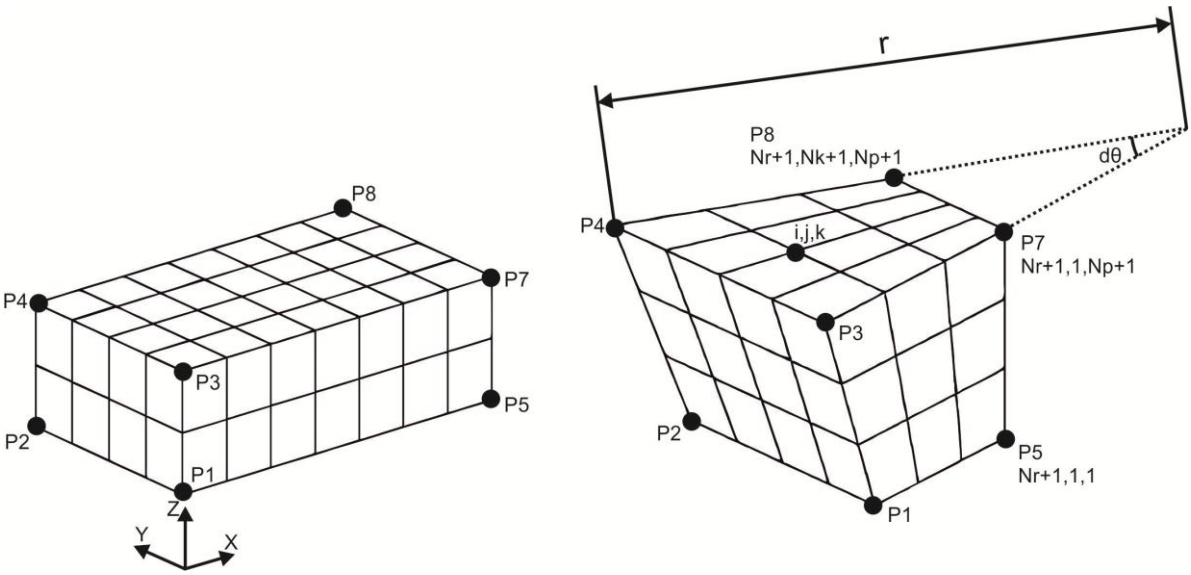

Figure 4-7 Schematic of Different Tool Segments

In proposed tool geometry modelling approach, tool segment length in x direction is always taken below nose radius of tool; because radius center creates singularity in mesh generation. Concurrently, segment length in x direction should be longer than maximum tool chip contact length. Moreover, segment thickness is selected according to boundary conditions. Distance between P3 and P4 is equal to differential cutting edge length for main cutting edge and for secondary edge.

$$\left|P3P4\right|_{tool} = \Delta l_{main} \quad for\ main\ cutting\ edge\ and\ secondary\ edge \tag{4.53}$$

P3-P4 distance is calculated by using right hand side geometry in Figure 4-7 for nose radius blocks as follows;

$$\left|P3P4\right|_{tool} = 2.r.\sin\left(\frac{d\theta}{2}\right) for\ nose\ radius\ part \tag{4.54}$$

Note that unengaged part of the nose radius discretized separately; thus, a new $d\theta$ value is calculated for that part.

After defining the segment geometry, mesh generation procedure is applied. First, initial grid point distribution is assigned. Then, grid point locations are calculated

by using elliptic grid generation scheme. Element numbers along x, y and z directions are showed in Figure 4-7 as Nr, Nk, Np respectively. It should be noticed that Nr and Np values are same for all tool blocks.

Tool heat balance equations are written for steady state condition. Thus, time derivative terms are equal to zero in equation (4.18).

$$\frac{\partial x}{\partial t} = 0, \frac{\partial y}{\partial t} = 0 \, and \, \frac{\partial z}{\partial t} = 0$$

Convection and radiation effects are neglected as in chip temperature modelling. Tool is assumed perfectly sharp in the analysis. Hence, wear land heat generation is not considered. Only rake face heat source is incorporated in tool temperature model. Heat source is applied to elements that are in contact with chip segments. Thus, tool and chip contact map should be determined via simple geometric calculation procedure. Since chip flow has an orientation, each tool block may have contact with multiple chip segments. Therefore, frictional heat fluxes from different chip blocks are applied to rake face depending on the contact map. Finite difference formulation of rake face heat source is written in to formulation as follows;

$$Q_{friction}(j,i) = w_z.\Delta\epsilon.\Delta n.\frac{P_{friction}(CN)}{k_{tool}.A_{contact}(CN)}.Bi\{TN\}(j,i) \tag{4.55}$$

After defining flux terms on rake face other boundary conditions are given. First, tool temperature values from neighbouring segments are applied to interface nodes that are between two consecutive segments. Second, room temperature is imposed to bottom face of the each tool segment. Moreover, room temperature is imposed to left side of the first tool segment (S_1 in Figure 4-6) and to right side of the last tool segment (S_n in Figure 4-6).

Solution procedure for tool temperature analysis starts with writing equilibrium equation (4.47) in compact form for all control volumes. Then, system of equations is solved for considered tool segment.

$$[D].[T_t] = [E] \tag{4.56}$$

In above equation, T_t is tool temperature array which is to be solved. D is square coefficient matrix and E is heat source array.

4.7 Workpiece Temperature Model

Workpiece is modelled segment by segment as in tool and chip temperature modelling. Tool workpiece engagement zone and neighbouring regions are modelled in the analysis. Layout of workpiece segments is illustrated (light grey zones named with $S_1, S_{i+1} \ldots . S_n$) in Figure 4-8. First, each workpiece block is created according to local oblique cutting geometry. After defining the geometries, grid generation procedure is employed.

Sample workpiece block and coordinate directions for a workpiece block are showed in Figure 4-8 and Figure 4-9. Each workpiece blocks' z direction is parallel to cutting velocity. x direction is opposite to feed direction. y direction is in radial direction. General dimensions of workpiece blocks are determined according to engagement profile. Length between P7 and P8 is equal to$|P3P4|_{tool}$. Length of neighbouring faces in z direction is taken equal to each other. $|P3P4|_{workpiece}$ of workpiece segment is written by using local inclination angle as follows;

$$\left|P3P4\right|_{workpiece} = \left|P7P8\right|.\cos(\lambda_s) \tag{4.57}$$

P2 and P1 length is written as;

$$\left|P1P2\right|_{workpiece} = \left|P3P4\right|_{workpiece}.\sin(\frac{\pi}{2} - \kappa r + \xi_r) \tag{4.58}$$

Workpiece block depth in y direction is selected regarding the boundary conditions. Furthermore, segment length in z direction is chosen arbitrarily.

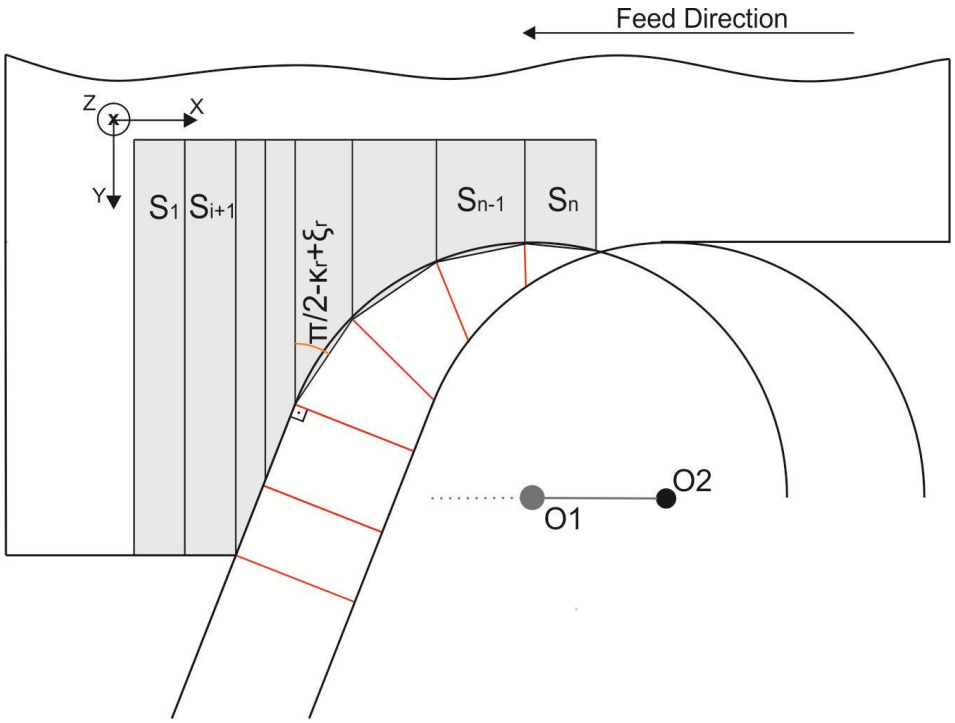

Figure 4-8 Layout of Workpiece Segments

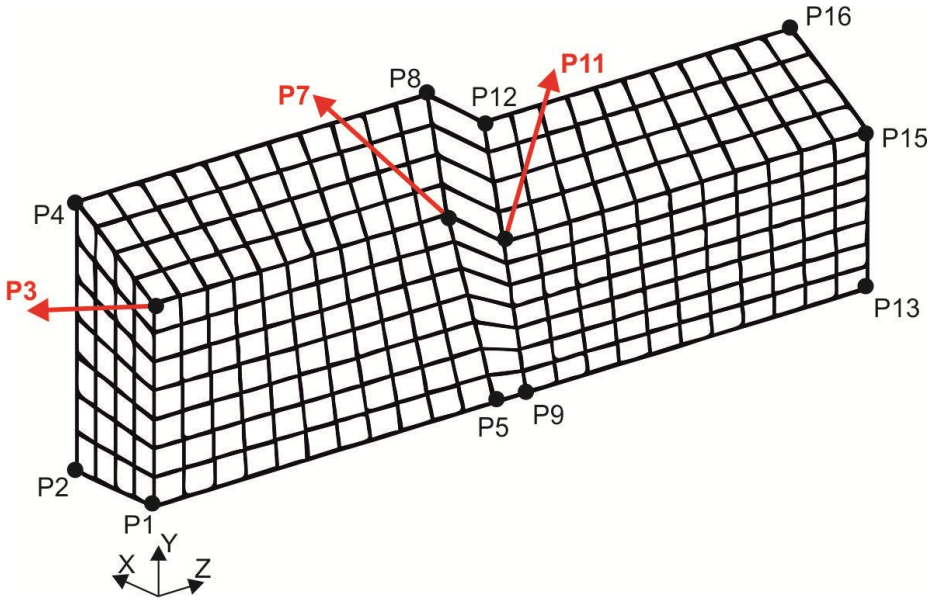

Figure 4-9 General Workpiece Block

After defining the workpiece block geometry, mesh generation procedure is applied. First, initial grid point distribution is determined. Then, grid point locations are

calculated by using elliptic grid generation scheme. As can be seen in Figure 4-9, workpiece section is variable in Z direction. Therefore, two dimensional grid generation scheme is applied for each different section along Z direction. Element numbers along x, y and z directions are showed in Figure 4-9 as Nu, Nv, Nw respectively. Note that Nw and Nv numbers are equal for every block. In addition, Nu is equal to Ny.

Each block is modelled using three dimensional heat and one dimensional mass transfer. Convection and radiation effects are neglected in the analysis. Since z direction is coincident with cutting velocity vector, it becomes mass transfer direction. It should be noticed that time derivative of x and y are equal to zero in equation (4.18).

$$\frac{\partial x}{\partial t} = 0 \, and \, \frac{\partial y}{\partial t} = 0$$

Heat source from shear plane is incorporated in analysis by calculating average shear plane temperature. Shear plane temperatures of chip are given as boundary condition to shear plane zone in engaged workpiece blocks. Moreover, room temperature is given to bottom face of each workpiece segment. Lastly, temperature values from neighbouring blocks are imposed. After defining heat generation terms and boundary conditions, equilibrium equation (4.47) for all control volumes is written in compact form. Then, system of equations is solved for considered workpiece block.

$$[R].[T_w] = [S] \tag{4.59}$$

In above equation, T_t is chip temperature array which is to be solved. R is square coefficient matrix and S is heat source array.

4.8 Working of the Model

In this subsection of the text, solution procedure for whole system is presented. As described previously whole geometry is splitted in to smaller sub-segments. Each sub segment is solved by considering the interrelationship between neighbouring

segments. Solution procedure starts with calculation of turning mechanics. In this part of the procedure, contact lengths, shear plane areas, power inputs, local geometric properties are calculated. After completion of the first step, iterative calculation procedure is started in order to calculate the temperature distributions.

Thermal solution procedure can be divided in to two main steps. First step is preparation to solution procedure and Second step is iterative solution procedure. In the first step, fixed parts of the solution algorithm are defined. This step starts with generation of local geometries and grid points. Then, coefficient matrixes are created for each segment. Since, coefficient matrixes are not changing, they are created for once in order to ease the procedure. After creation of geometric properties, tool and chip contact pattern is determined. Determination of the contact pattern is critical to apply heat generation boundary condition between tool and chip interface. Contact map is calculated for one time and then used in successive iterations.

Determination procedure for tool and chip contact map is carried out by simple distance calculations. First, positions of chip nodes at tool-chip interface are calculated. Then, distances between chip and tool nodes on rake face are calculated for all segments that may contact with related chip segment. Series of coordinate transformations are written in order to write chip coordinates in terms of benchmarked tool segment coordinate frame. At the end, nearest node is selected as reciprocal node for related chip node.

Before starting the second step, preconditioning matrixes are created. The reason behind preconditioning is to create a linear equation system that has lower condition number with respect to original one. Preconditioning accelerates the convergence rate of the numerical solution. In addition, it increases calculation precision in direct operations.

Heat balance equations are solved in second step. Solutions are carried out until maximum temperature difference between reciprocal nodes of tool and chip decreases below specified value for all blocks. Convergence is reached by adjusting the frictional

heat flux input to tool and chip in each iteration. Thus, determination of unique heat partition values for each nodal point that are in tool chip contact zone comes into prominence. Partition values are not known initially. Hence, solutions are started with initial value assignments to partition values. Initial assignments have constant values between 0 and 1 for all nodes. After each cycle, heat partition values are updated by using the difference measure between reciprocal nodes. Difference measure is defined as;

$$dBi = \frac{T_c\{CN\}(CEN) - T_t\{TN\}(TEN)}{\left(\frac{T_c\{CN\}(CEN) + T_t\{TN\}(TEN)}{2}\right)} \tag{4.60}$$

TEN and CEN are tool and chip element numbers respectively in above equation. After each solution cycle, maximum absolute value of difference measure is checked. If it is below previously set value, iterations are stopped. If it is not, partition values are updated for each node in contact and solution is carried on. Partitions are updated for related nodes by using below expression;

$$Bi\{TN\}(TEN) = Bi\{TN\}(TEN) + Gain.dBi \tag{4.61}$$

Gain value is used to adjust convergence behaviour. Sometimes temperature difference between reciprocal nodes can be high. In that kind of situation, gain values between 0 and 1 can be assigned for convergence. Moreover, convergence rate can be increased by using gains that are higher than 1 if it is suitable.

As stated previously, each segment uses neighbouring faces' temperature values as boundary condition. Those boundary conditions are applied by imposing preceding cycle's temperature history in solutions. Thus, preset difference measure should be sufficiently low in order to neglect temperature distribution difference between successive iterations.

Chapter 5: Validations

In this section of the thesis, temperature model validations are presented. Validations are carried out for AISI 4140 workpiece material and Kennametal SPG-422 K313 uncoated carbide insert couple by using the data available in Leshock and Shin' s study [1]. They used tool-work thermocouple technique in order to monitor temperature values. This method is one of the most popular methods for determining interface temperatures. Measurement technique is based on the principle that different emf values are generated at different interface temperatures. Normally, measured average interface emf value does not correspond to average interfacial temperature [1], [60]. However, Stephenson [60] concluded that tool-work thermocouple technique gives average temperatures with small error (less than % 5) for carbide tools with common materials. This behaviour is due to carbide tools' linear temperature and emf relation [61]. Therefore, measured values are taken as average interfacial temperatures in this section of the thesis.

Validations were carried out for nine cases that are available in reference [1]. Three level of cutting speeds, two level of feed rate and depth of cut was simulated. Simulation conditions are listed in Table 5-1. Thermal material properties were taken at room temperature in the simulations. They are listed in Table 5-2. Tool geometry for Kennametal SPG-422 K313 tool is listed in Table 5-3. Orthogonal data base is confidential and it belongs to Manufacturing Automation Laboratories Inc.. Therefore, data base was not given in this text.

Table 5-1 Simulation Conditions

Case Number #	Cutting Speed (m/s)	Feedrate (mm/rev)	Depth of Cut (mm)
1	1.295	0.175	1.27
2	1.91	0.175	1.27
3	2.49	0.175	1.27
4	1.295	0.175	0.762
5	1.91	0.175	0.762
6	2.49	0.175	0.762
7	1.295	0.124	0.762
8	1.91	0.124	0.762
9	2.49	0.124	0.762

Table 5-2 Thermal Properties of Workpiece and Tool Materials

	Tool [62]	Workpiece
Conductivity (W/m.K)	79	42.6
Specific heat capacity (J/kg.K)	138	473
Density (kg/m^3)	14900	7850

Table 5-3 Tool Geometric Properties

Geometric Properties of Kennametal SPG-422 K313 insert [1]	
Nose Radius (mm)	0.8
Included angle (degrees)	90
Side rake angle (degrees)	5
Back rake angle (degrees)	0
κr **(degrees)**	75

5.1 Simulation Results

In this part, results for tool and chip are presented. Since workpiece solution is based on shear plane temperatures in chip, workpiece simulations were done only for two cases. In grid generation procedure, nominal differential element length is taken equal to 10 micron for all directions in all simulations. In chip simulations, element numbers are equal to each other in x direction and element numbers in this direction are determined according to longest chip segment. Therefore, differential element length in x direction becomes smaller for other chip segments. Simulations are stopped when maximum temperature difference between reciprocal nodes becomes below seven percent.

Results for Case 1;

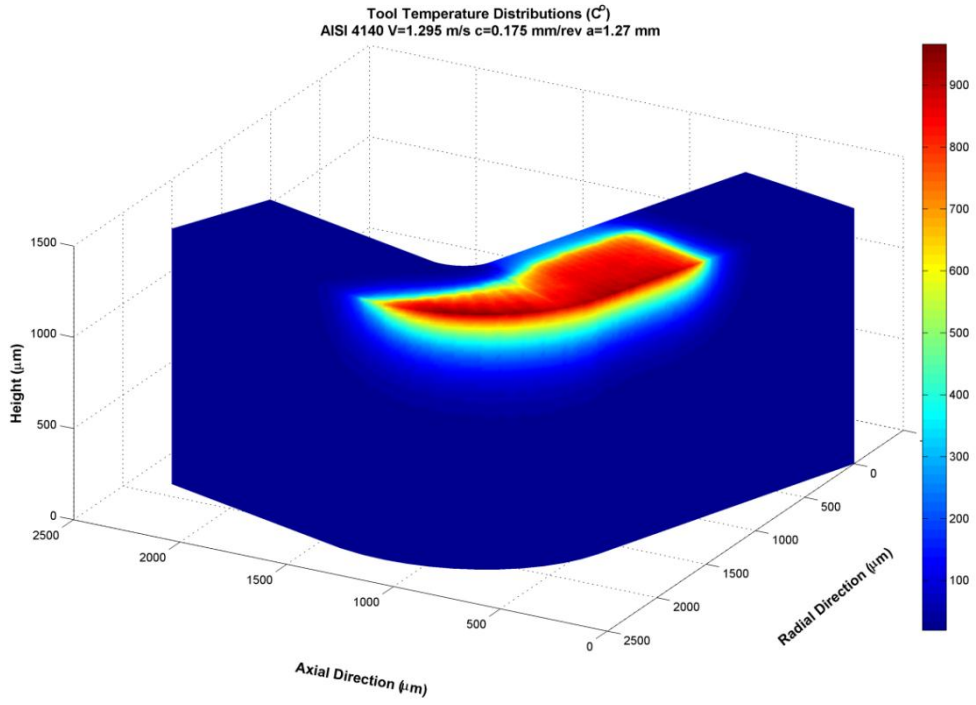

Figure 5-1 Three Dimensional Tool Temperature Distributions for AISI 4140 V=1.295 m/s c=0.175 mm/rev and a=1.27 mm

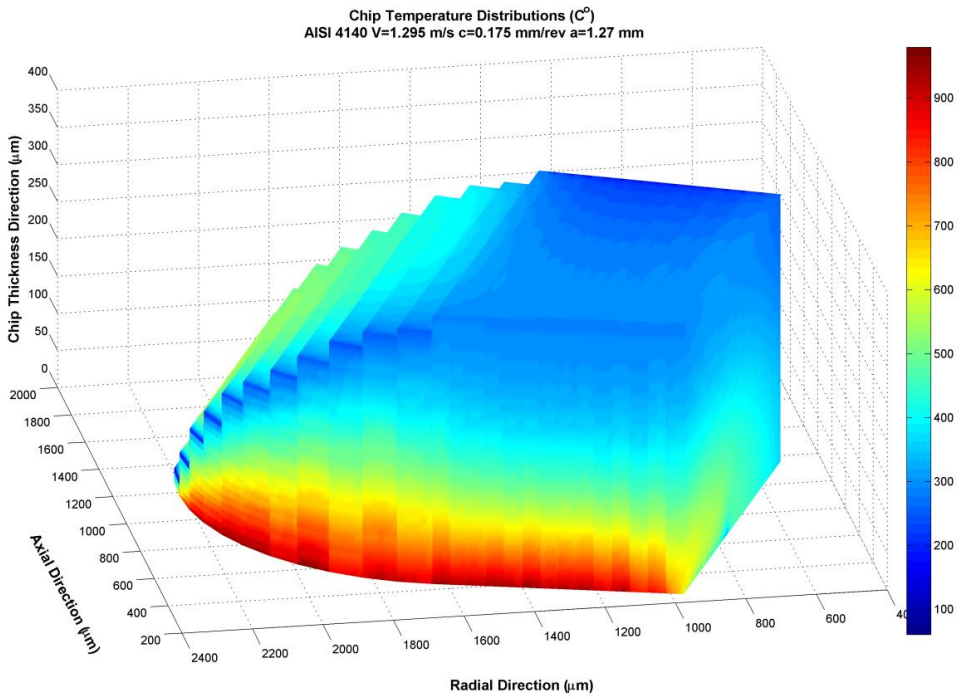

Figure 5-2 Three Dimensional Chip Temperature Distributions for AISI 4140 V=1.295 m/s c=0.175 mm/rev and a=1.27 mm

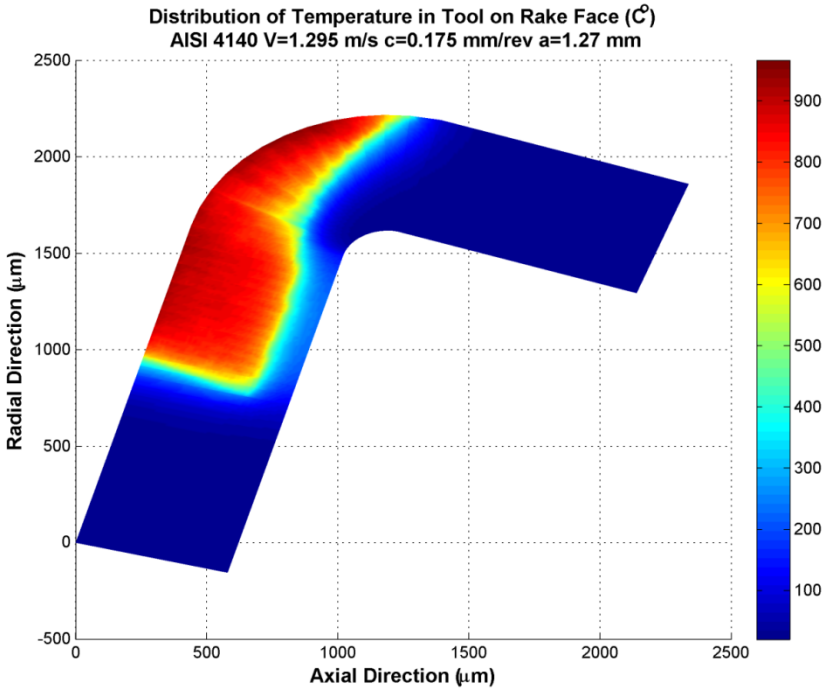

Figure 5-3 Rake Face Temperature Distributions for AISI 4140 V=1.295 m/s c=0.175 mm/rev and a=1.27 mm

Results Case 2;

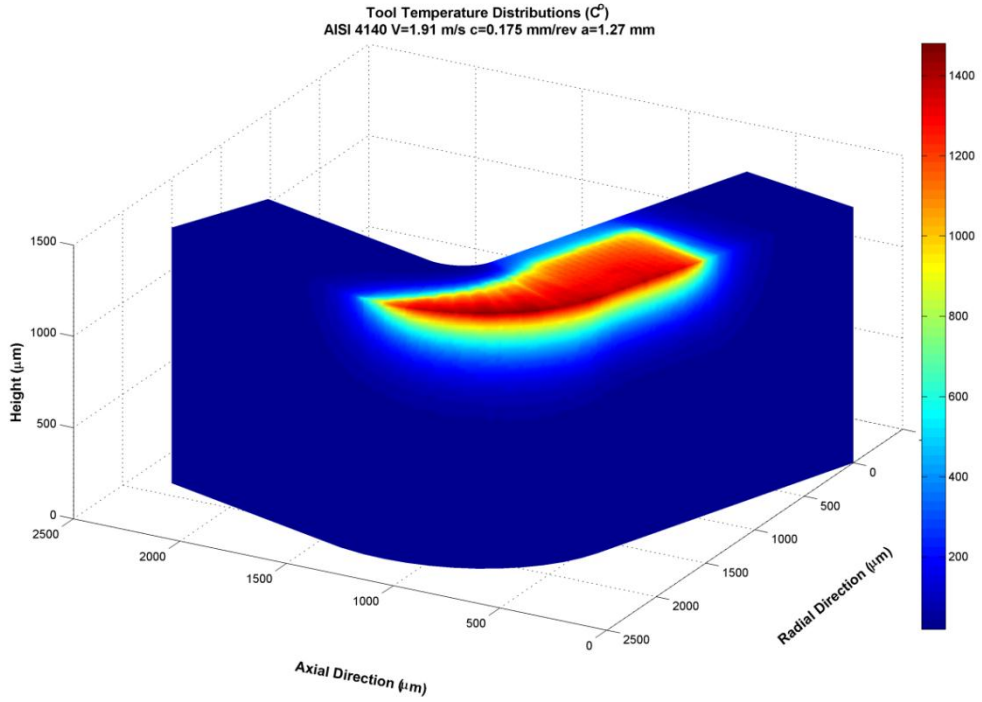

Figure 5-4 Three Dimensional Tool Temperature Distributions for AISI 4140 V=1.91 m/s c=0.175 mm/rev and a=1.27 mm

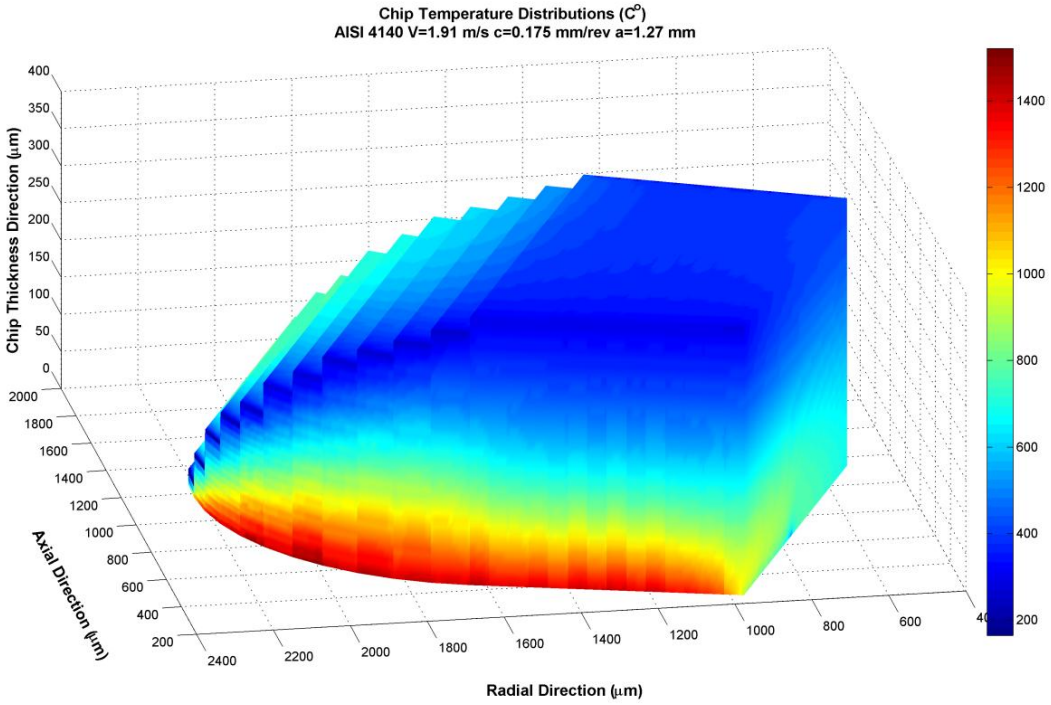

Figure 5-5 Three Dimensional Chip Temperature Distributions for AISI 4140 V=1.91 m/s c=0.175 mm/rev and a=1.27 mm

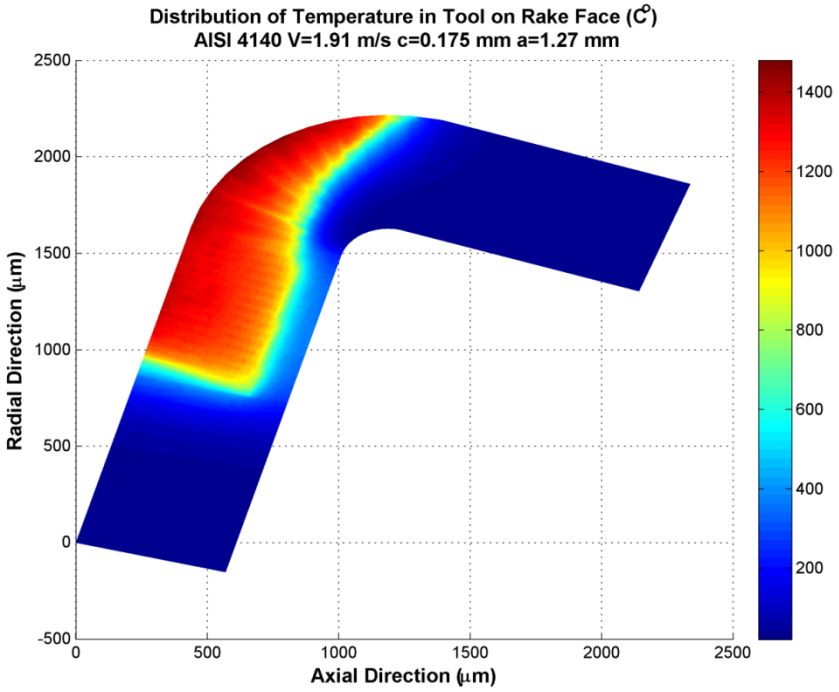

Figure 5-6 Rake Face Temperature Distributions for AISI 4140 V=1.91 m/s c=0.175 mm/rev and a=1.27 mm

Results for Case 3;

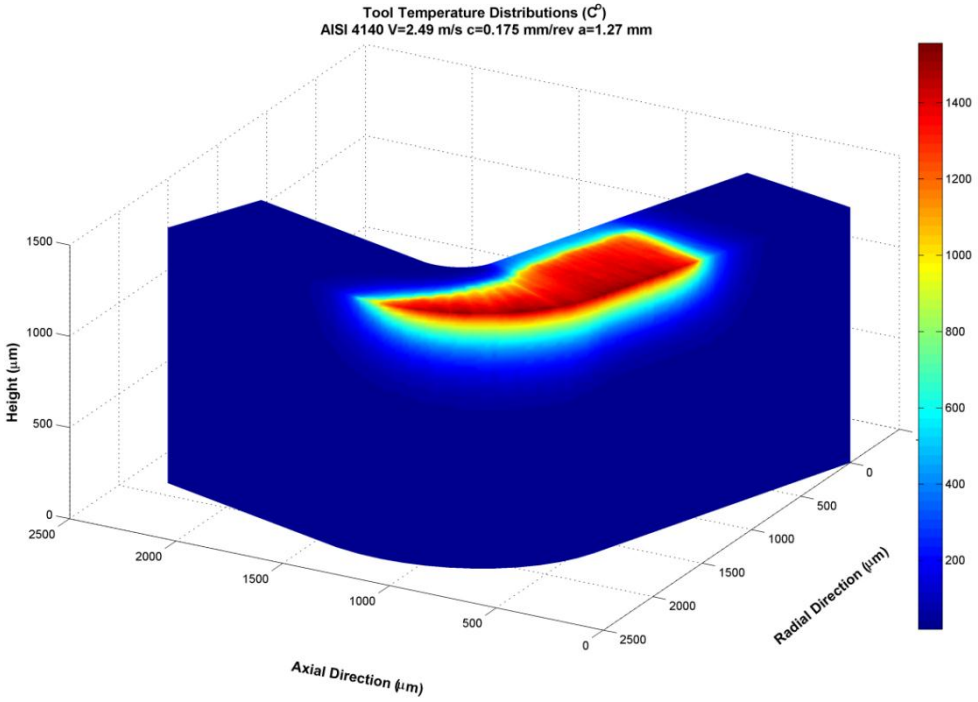

Figure 5-7 Three Dimensional Tool Temperature Distributions for AISI 4140 V=2.49 m/s c=0.175 mm/rev and a=1.27 mm

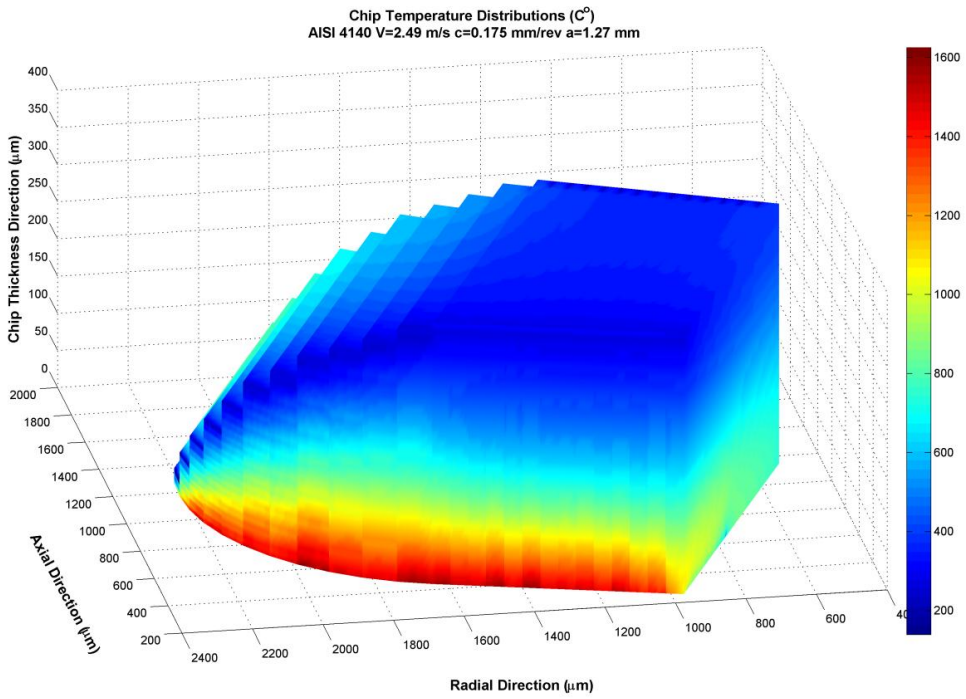

Figure 5-8 Three Dimensional Chip Temperature Distributions for AISI 4140 V=2.49 m/s c=0.175 mm/rev and a=1.27 mm

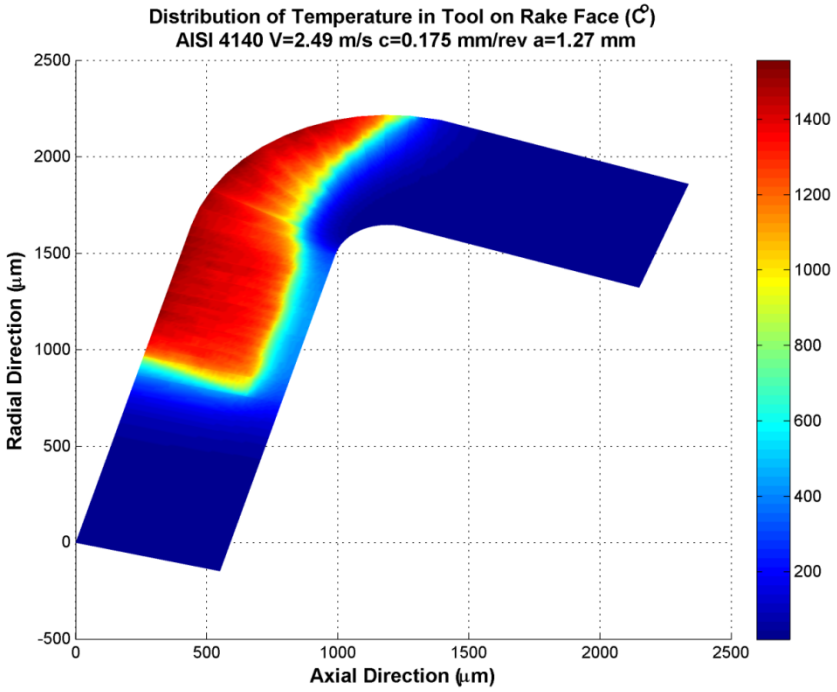

Figure 5-9 Rake Face Temperature Distributions for AISI 4140 V=2.49 m/s c=0.175 mm/rev and a=1.27 mm

Results for Case 4;

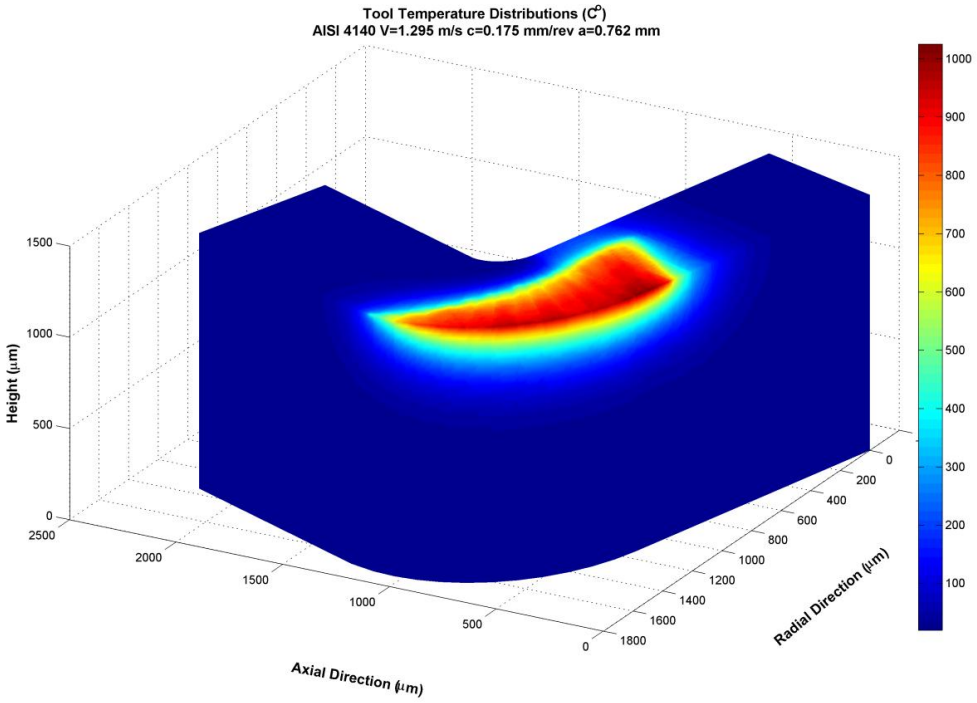

Figure 5-10 Three Dimensional Tool Temperature Distributions for AISI 4140 V=1.295 m/s c=0.175 mm/rev and a=0.762 mm

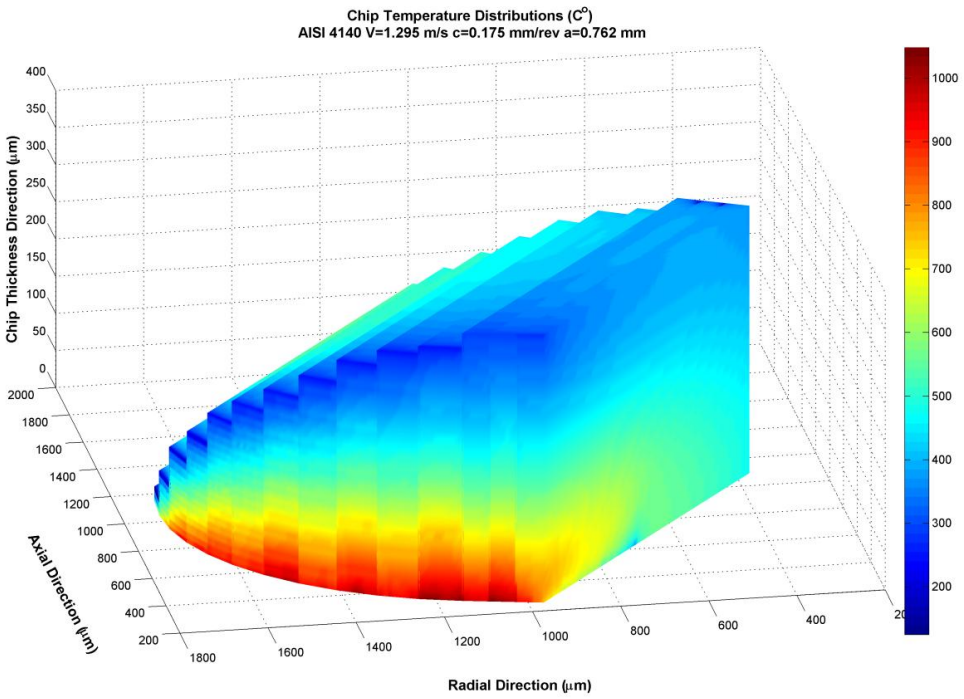

Figure 5-11 Three Dimensional Chip Temperature Distributions for AISI 4140 V=1.295 m/s c=0.175 mm/rev and a=0.762 mm

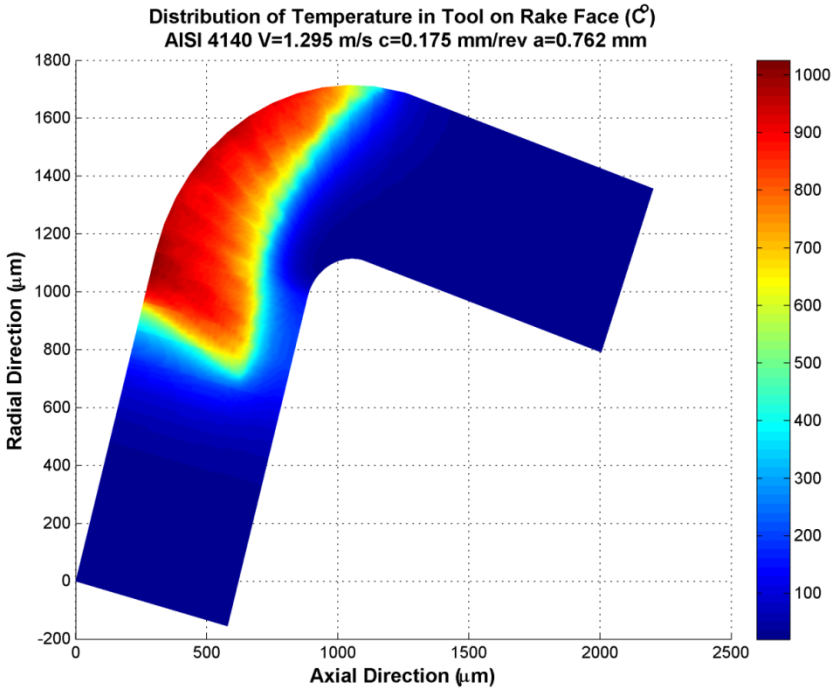

Figure 5-12 Rake Face Temperature Distributions for AISI 4140 V=1.295 m/s c=0.175 mm/rev and a=0.762 mm

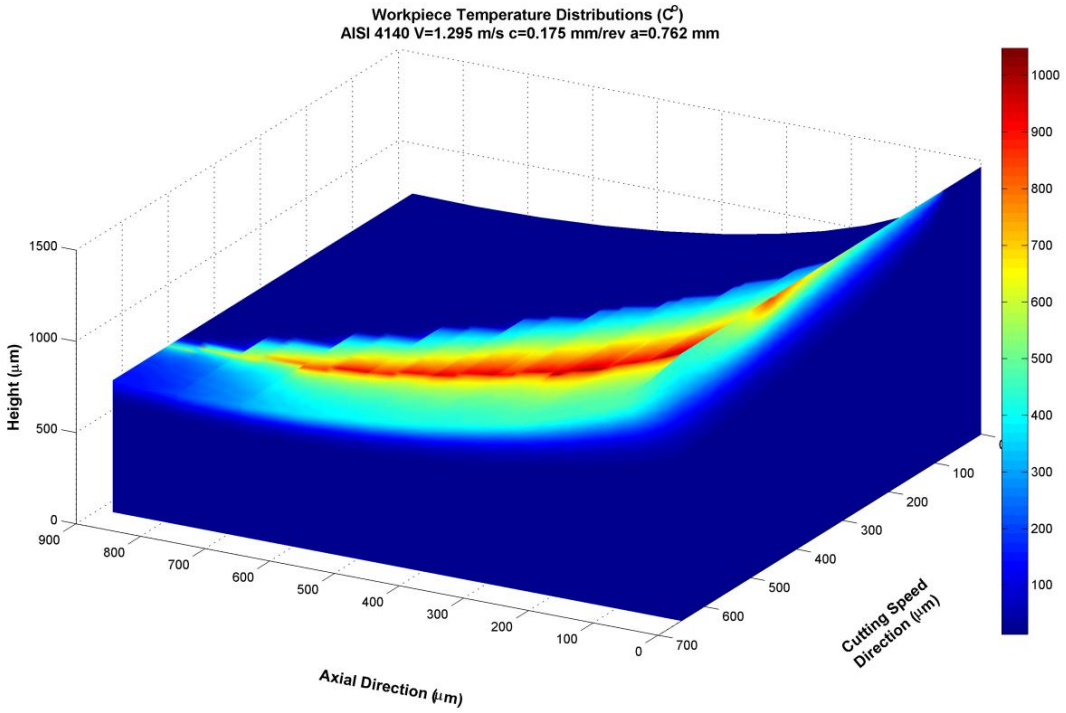

Figure 5-13 Workpiece Temperature Distributions for AISI 4140 V=1.295 m/s c=0.175 mm/rev and a=0.762 mm

Results for Case 5;

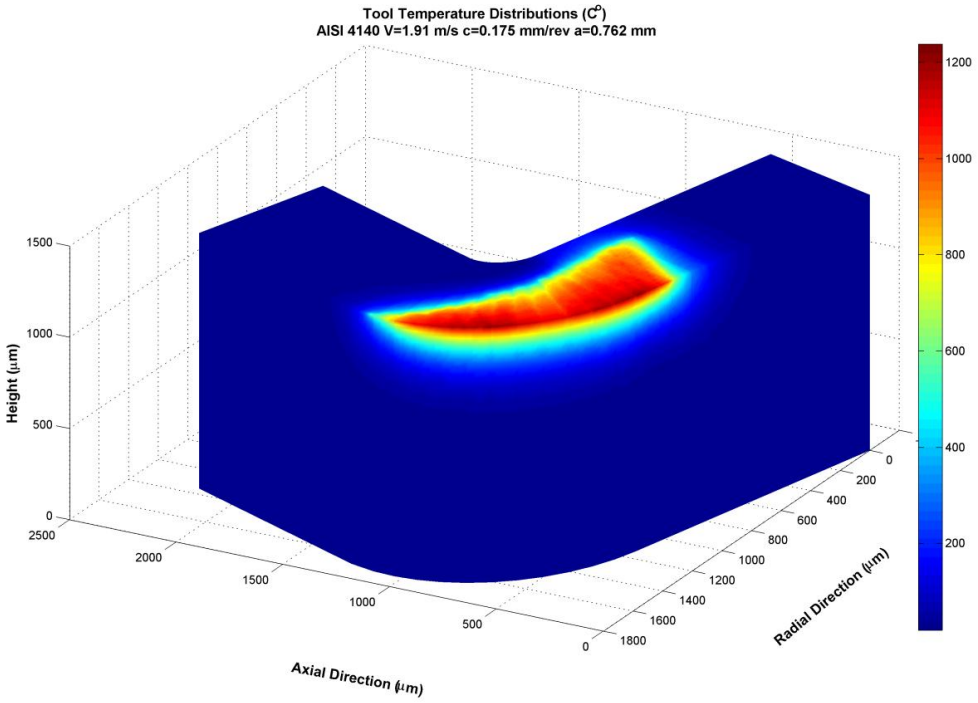

Figure 5-14 Three Dimensional Tool Temperature Distributions for AISI 4140 V=1.91 m/s c=0.175 mm/rev and a=0.762 mm

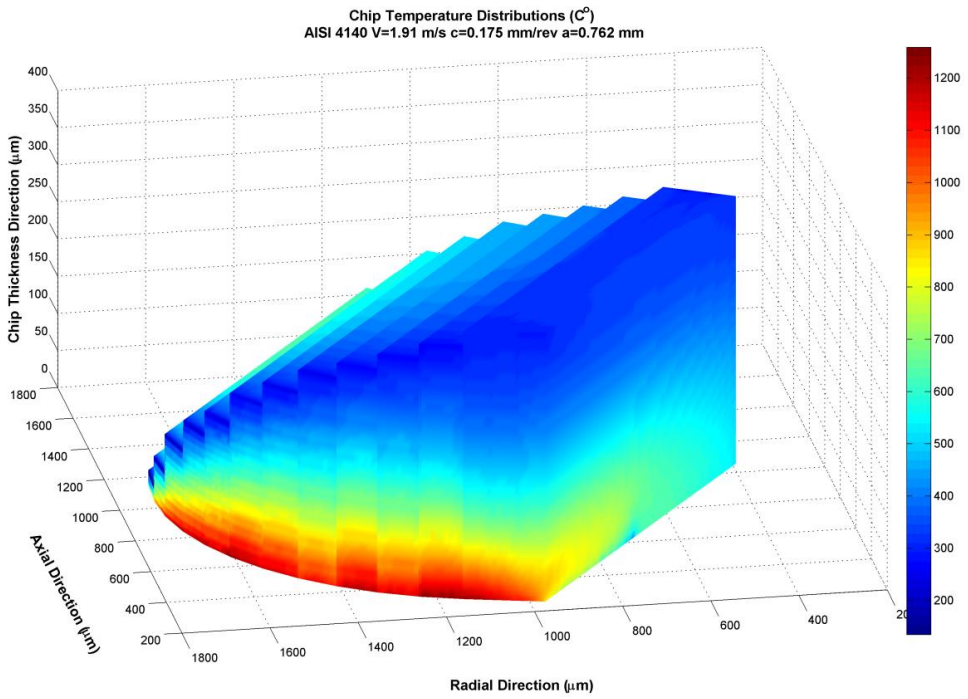

Figure 5-15 Three Dimensional Chip Temperature Distributions for AISI 4140 V=1.91 m/s c=0.175 mm/rev and a=0.762 mm

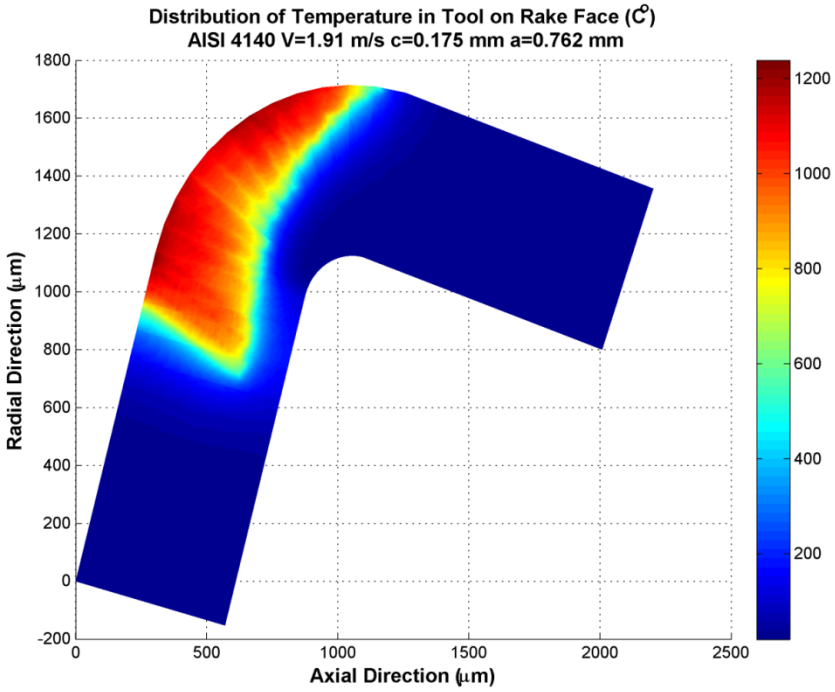

Figure 5-16 Rake Face Temperature Distributions for AISI 4140 V=1.91 m/s c=0.175 mm/rev and a=0.762 mm

Results for Case 6;

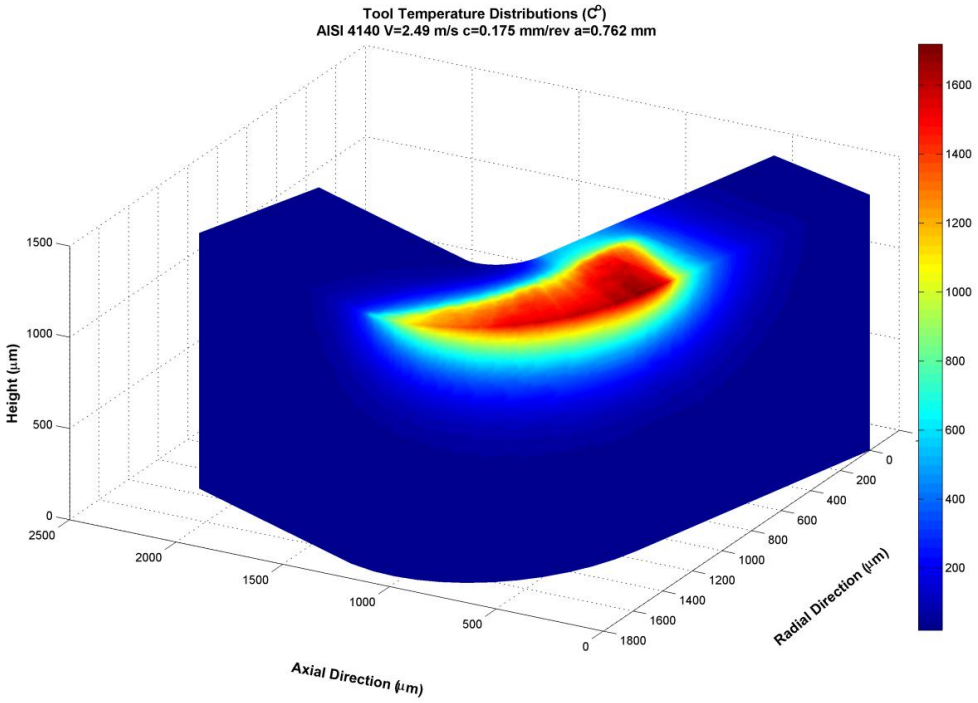

Figure 5-17 Three Dimensional Tool Temperature Distributions for AISI 4140 V=2.49 m/s c=0.175 mm/rev and a=0.762 mm

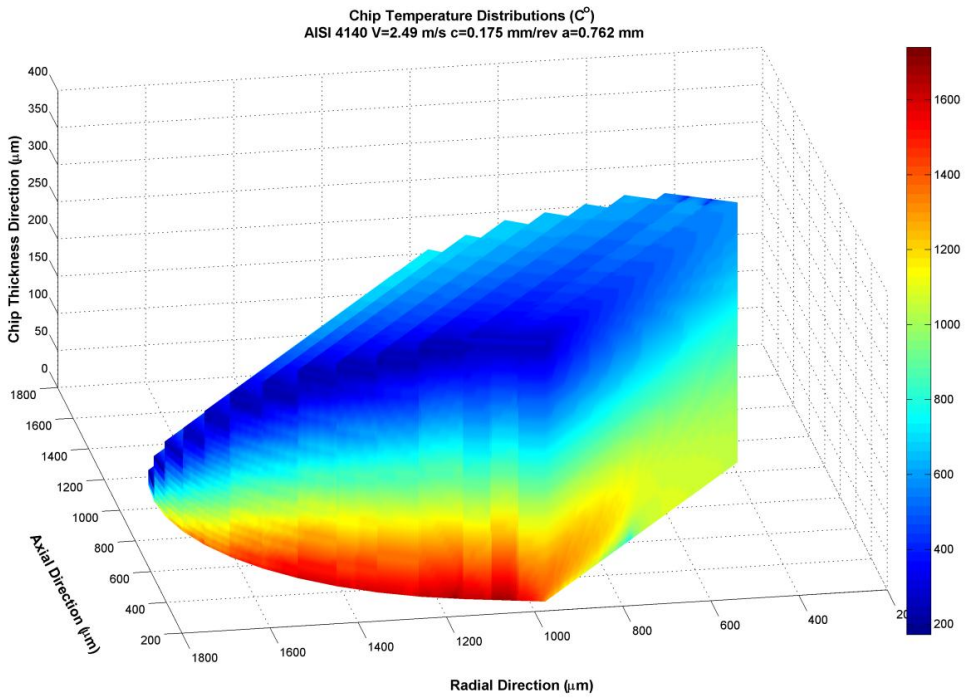

Figure 5-18 Three Dimensional Chip Temperature Distributions for AISI 4140 V=2.49 m/s c=0.175 mm/rev and a=0.762 mm

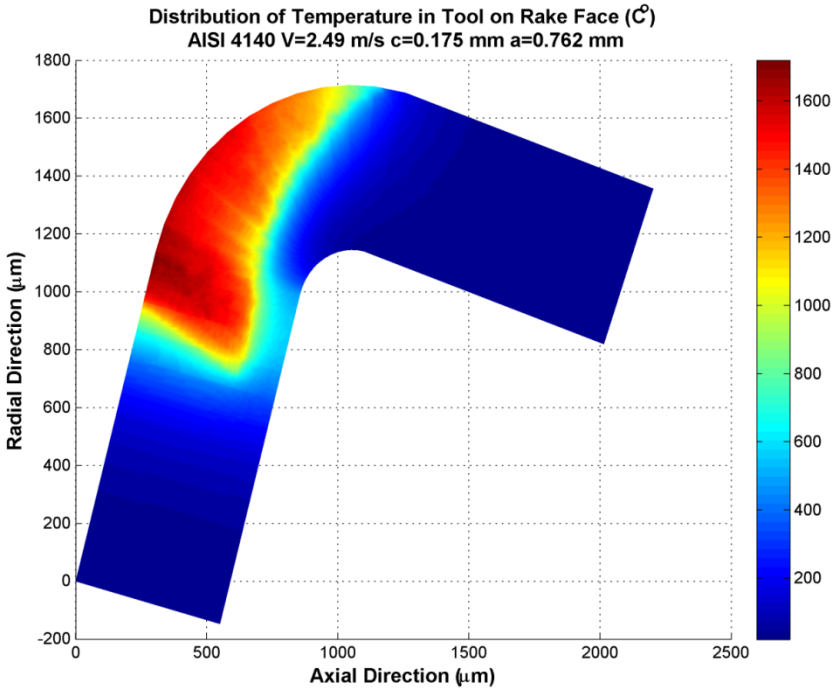

Figure 5-19 Rake Face Temperature Distributions for AISI 4140 V=2.49 m/s c=0.175 mm/rev and a=0.762 mm

Results for Case 7;

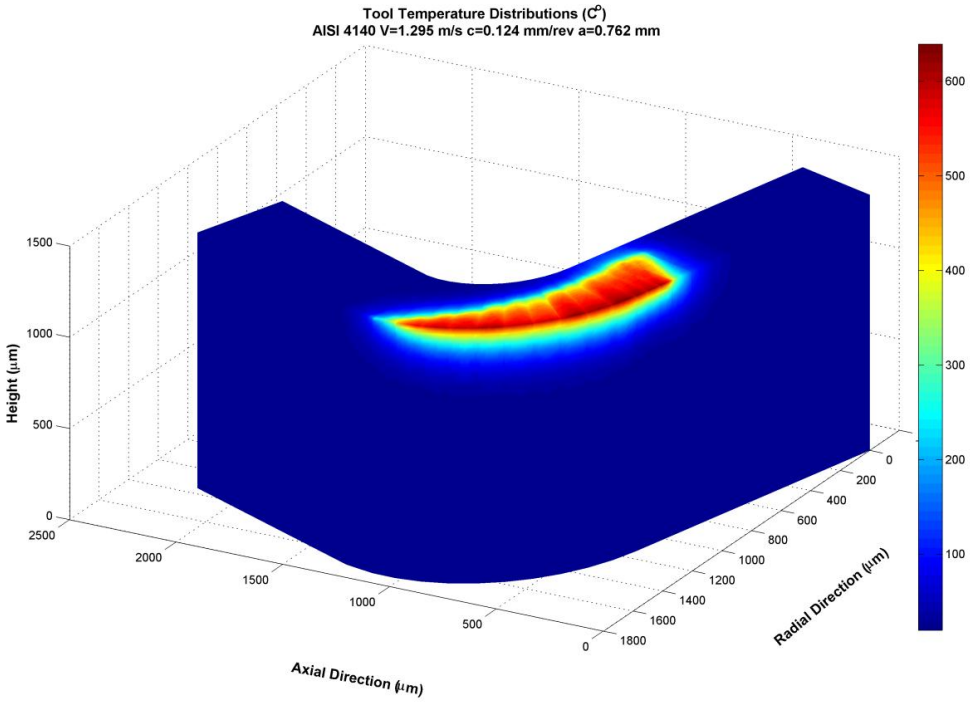

Figure 5-20 Three Dimensional Tool Temperature Distributions for AISI 4140 V=1.295 m/s c=0.124 mm/rev and a=0.762 mm

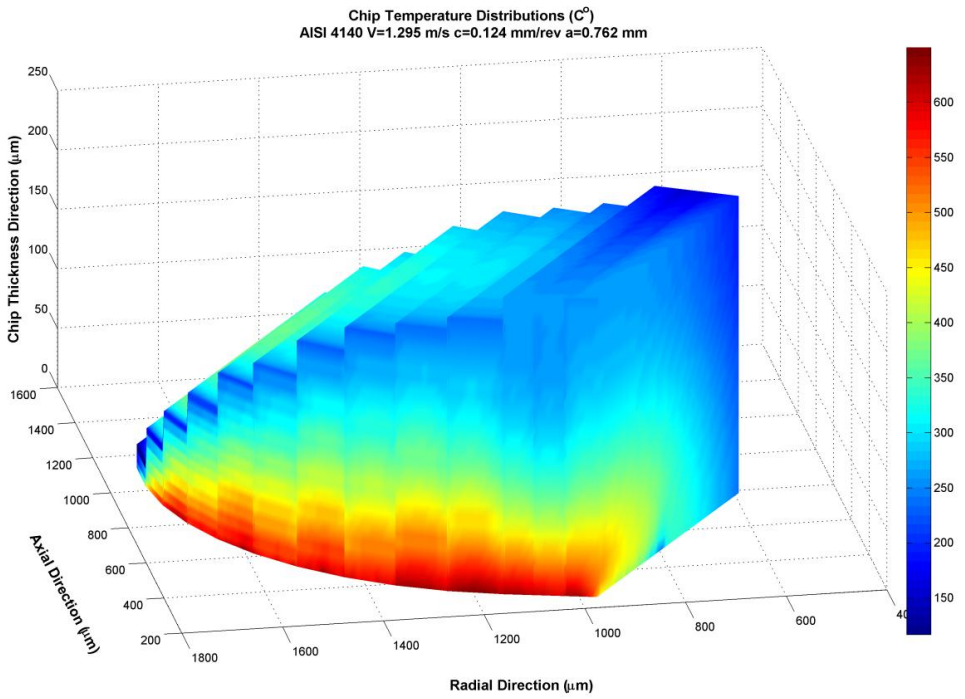

Figure 5-21 Three Dimensional Chip Temperature Distributions for AISI 4140 V=1.295 m/s c=0.124 mm/rev and a=0.762 mm

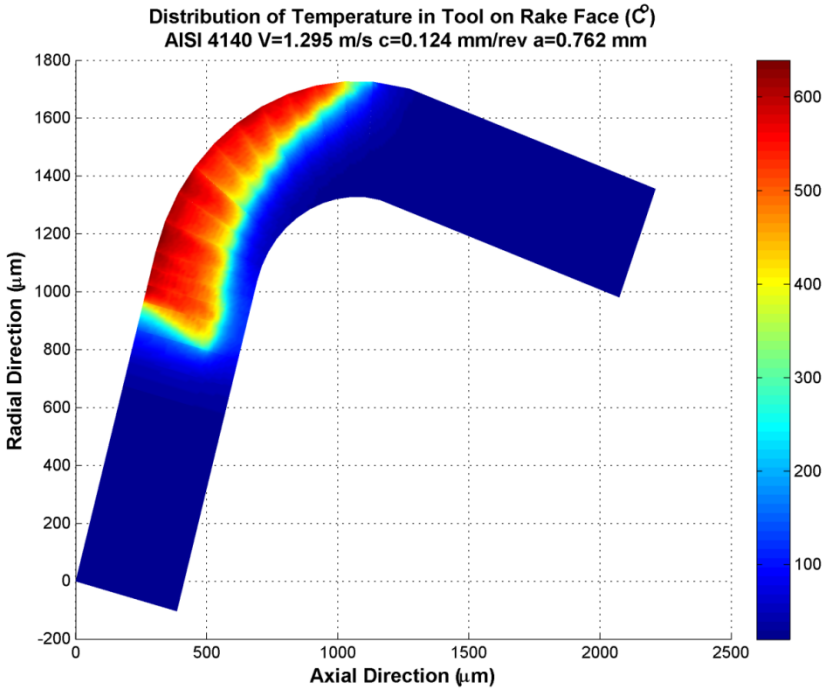

Figure 5-22 Rake Face Temperature Distributions for AISI 4140 V=1.295 m/s c=0.124 mm/rev and a=0.762 mm

Results for Case 8;

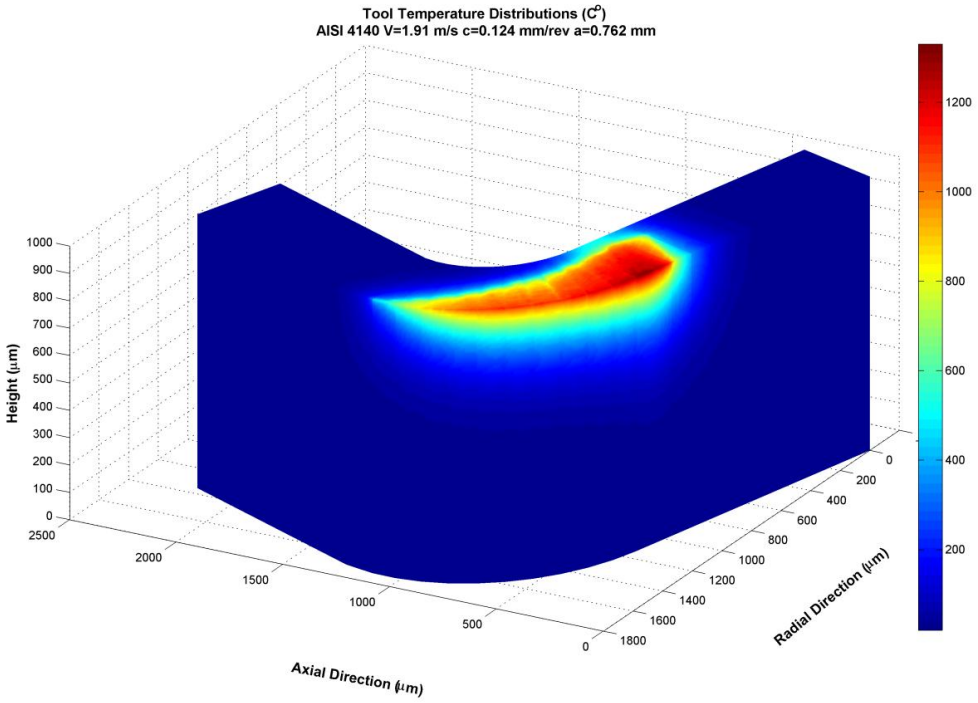

Figure 5-23 Three Dimensional Tool Temperature Distributions for AISI 4140 V=1.91 m/s c=0.124 mm/rev and a=0.762 mm

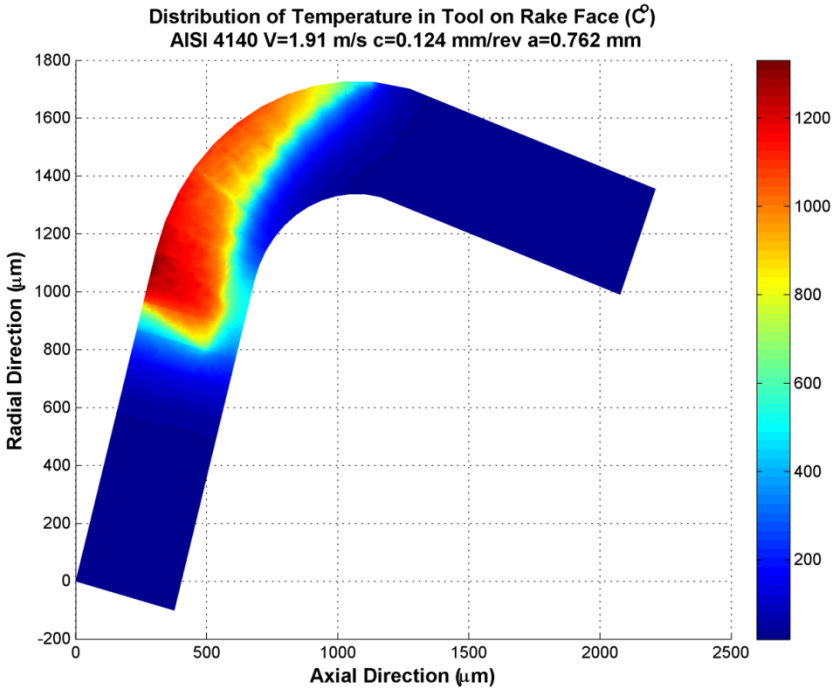

Figure 5-24 Rake Face Temperature Distributions for AISI 4140 V=1.91 m/s c=0.124 mm/rev and a=0.762 mm

Results for Case 9;

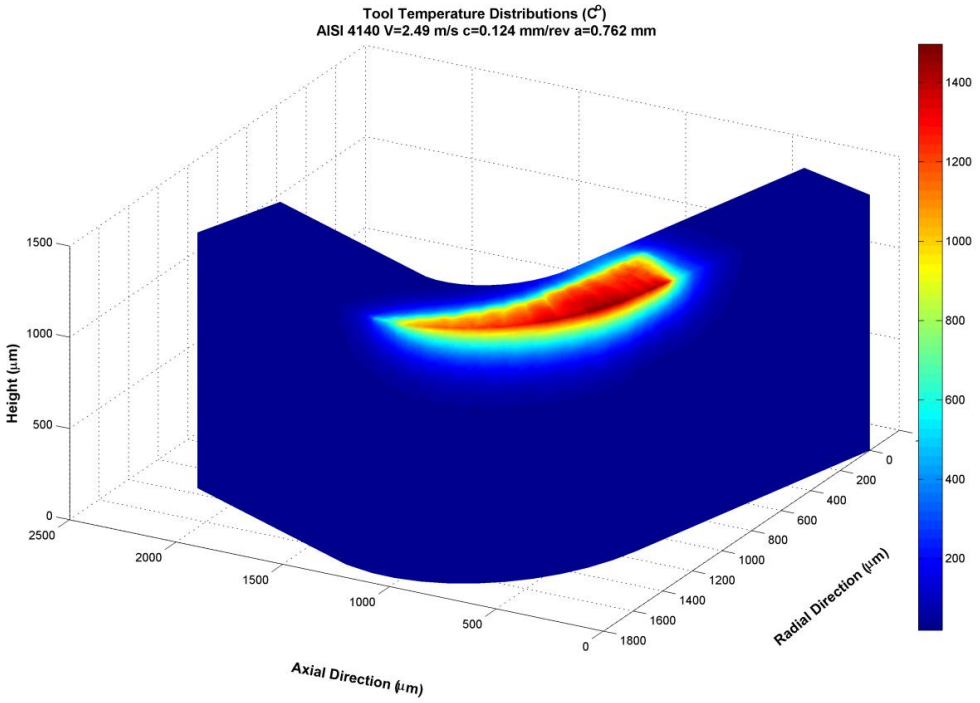

Figure 5-25 Three Dimensional Tool Temperature Distributions for AISI 4140 V=2.49 m/s c=0.124 mm/rev and a=0.762 mm

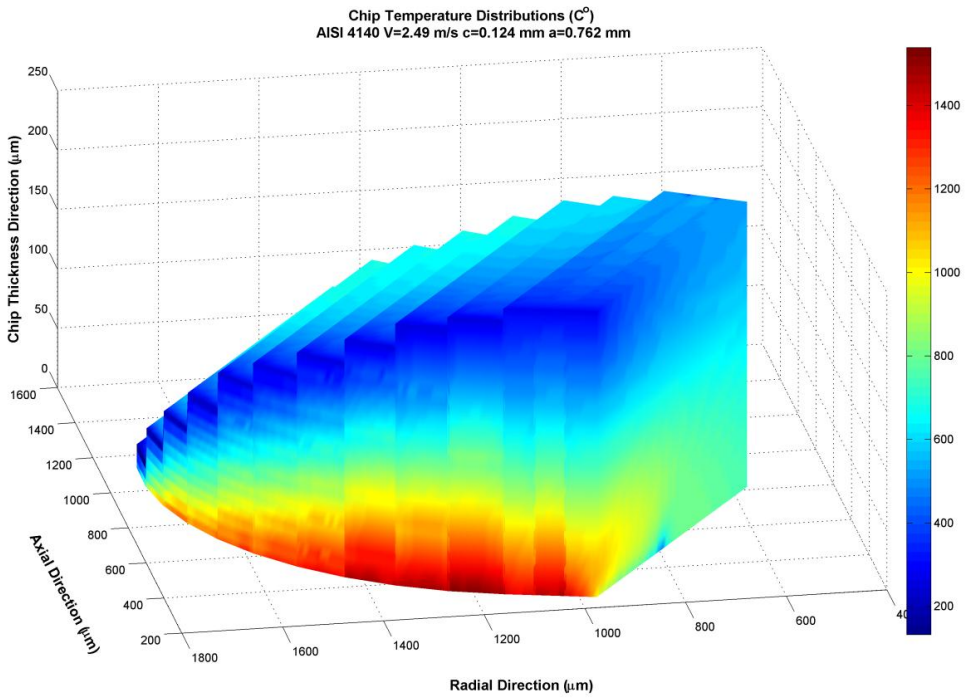

Figure 5-26 Three Dimensional Chip Temperature Distributions for AISI 4140 V=2.49 m/s c=0.124 mm/rev and a=0.762 mm

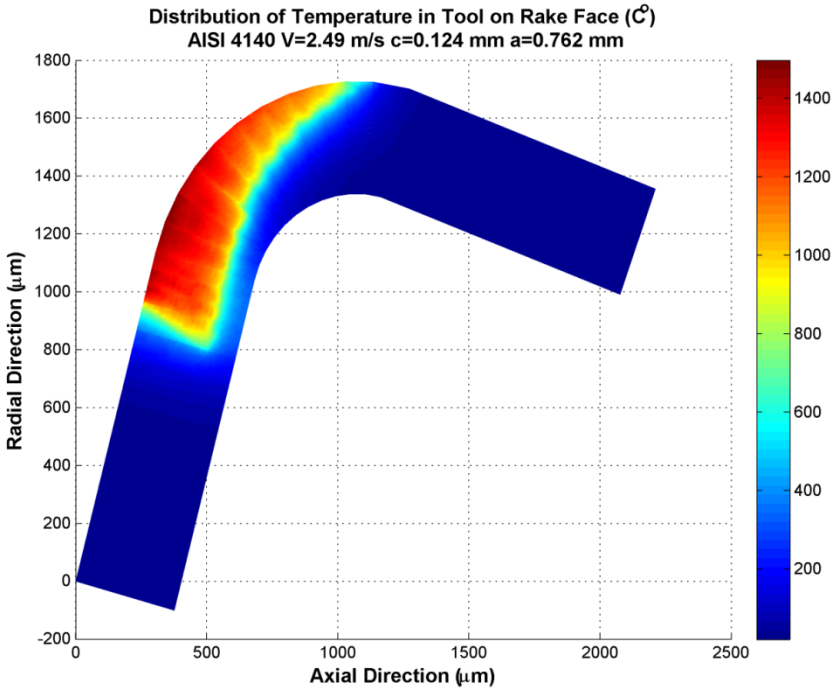

Figure 5-27 Rake Face Temperature Distributions for AISI 4140 V=2.49 m/s c=0.124 mm/rev and a=0.762 mm

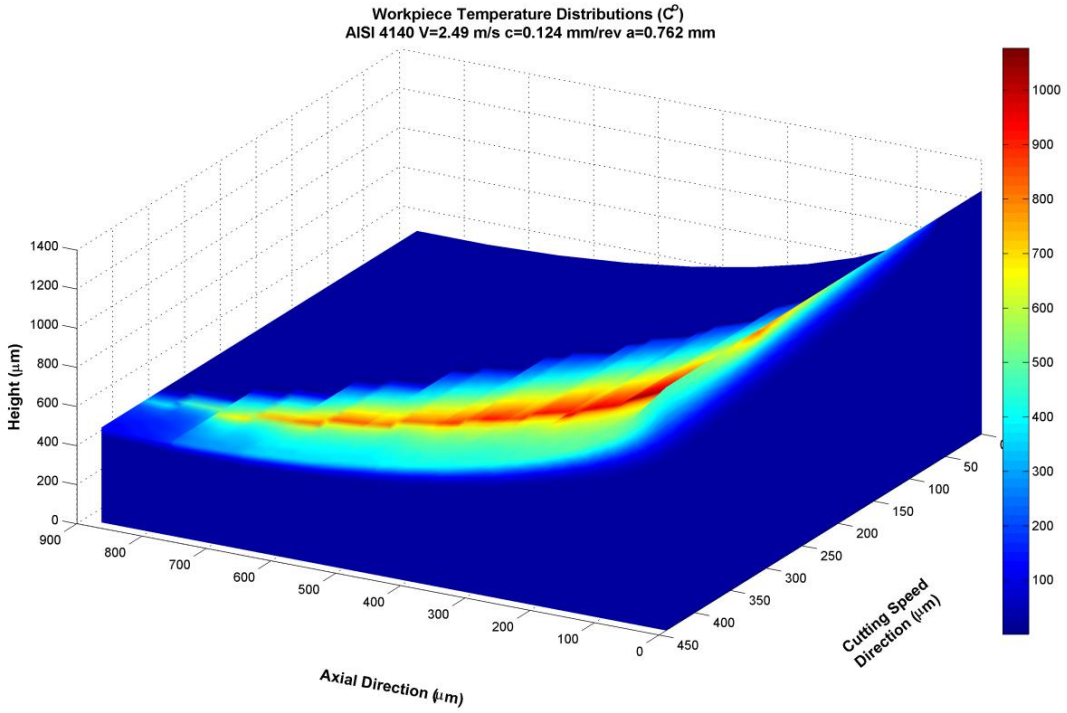

Figure 5-28 Workpiece Temperature Distributions for AISI 4140 V=2.49 m/s c=0.124 mm/rev and a=0.762 mm

5.2 Benchmarks

Graphical records from Leshock and Shin's [1] article are listed below. Approximate values of data points (depending on the correlation equation (5.1) in [1]) are listed in Table 5-4 with simulation results. Note that correlation equation results in higher values compared to Figure 5-29, Figure 5-30 and Figure 5-31.

$$T_{mean}(^{o}C) = 1700.V^{0.5}.a^{0.2}.c^{0.4} \quad (5.1)$$

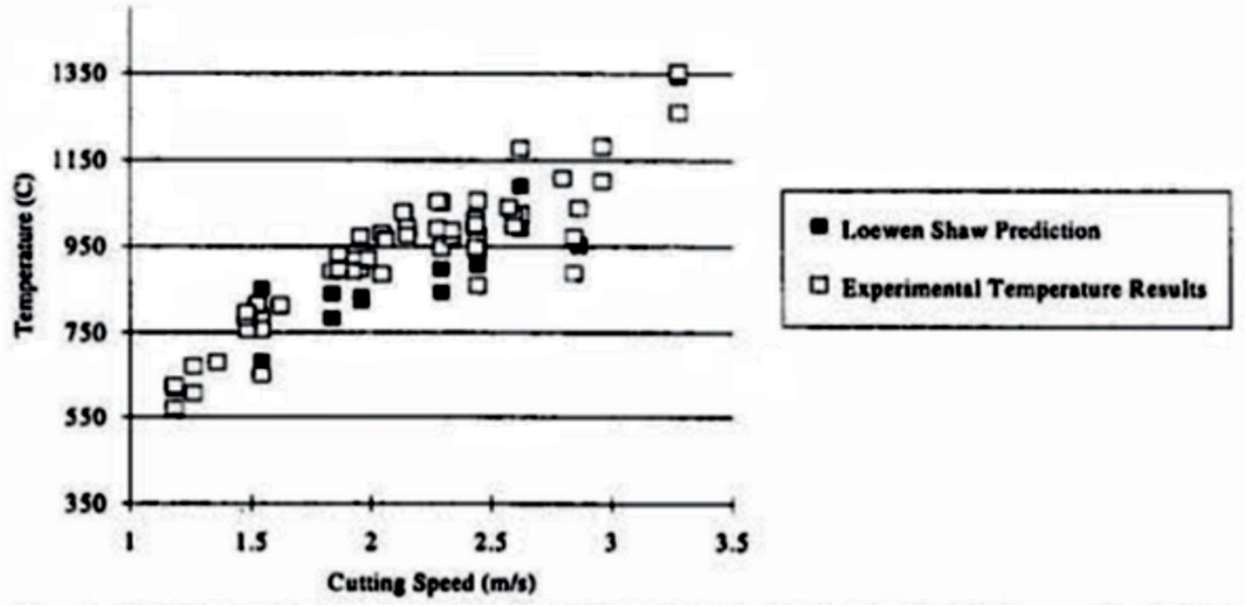

Figure 5-29 Temperature vs. Cutting Speed from [1] for a=0.762 mm and c=0.124 mm/rev

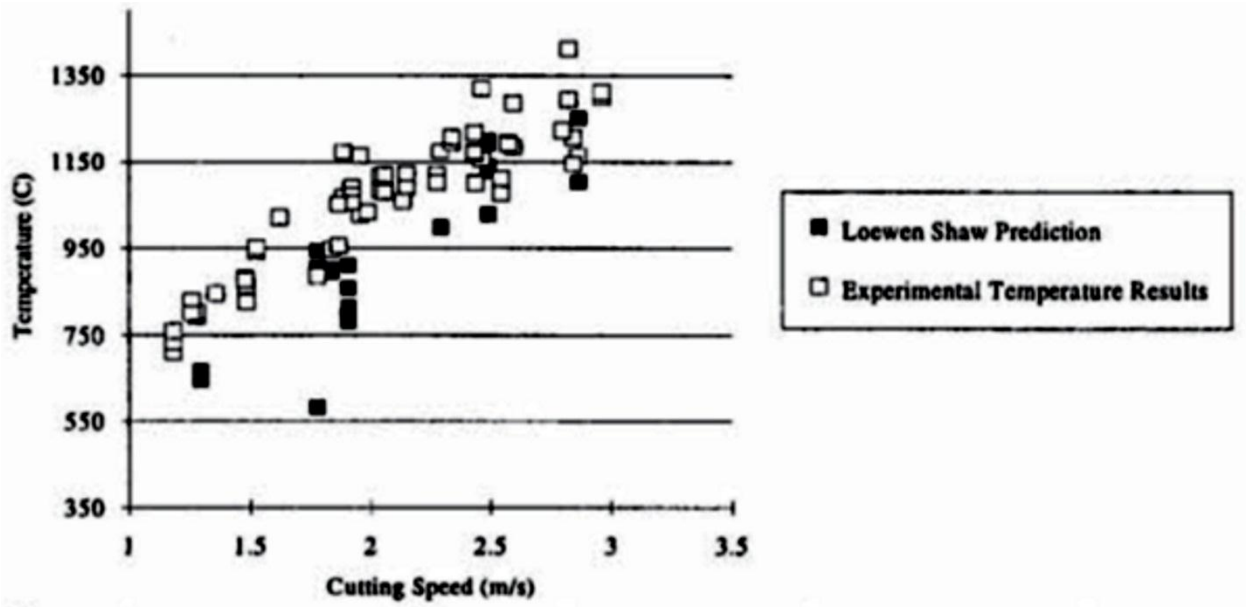

Figure 5-30 Temperature vs. Cutting Speed from [1] for a=0.762 mm and c=0.175 mm/rev

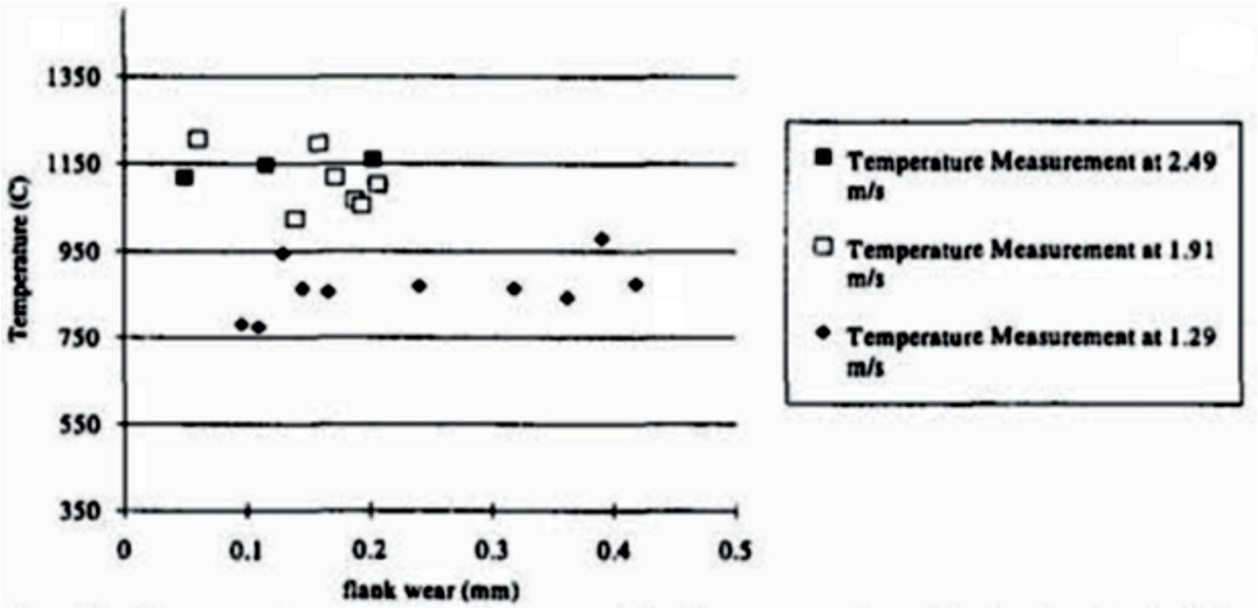

Figure 5-31 Temperature vs. Flank wear from [1] for V=1.295, 1.91, 2.49 m/s a=1.27 mm and c=0.175 mm/rev

Table 5-4 Mean Interface Temperatures According to Simulations and Correlation Equation

Case Number #	**Simulated T_{mean} (^oC)**	**Correlation Equation (5.1) T_{mean} (^oC)**
1	858	1010
2	1286	1227
3	1403	1401
4	859	912
5	1022	1108
6	1427	1265
7	526	790
8	1002	965
9	1082	1102

As can be seen from above results, simulations are in acceptable agreement with results in the Figure 5-29, Figure 5-30 and Figure 5-31. Average interface temperatures increases with increasing cutting velocity as expected. Except case 7 simulated average temperature values are higher than experimental ones. This behaviour can be due to neglected convection effects.

In case 7 reason behind lower prediction can be due to orthogonal data base calibration limits. Moreover, tool-work thermocouple technique measurements are very sensitive to calibration of the experimental setup. There can be some errors related to calibration.

The highest temperature values are generally observed at places that are close to cutting edge for all cases. This behaviour is probably due to localization of heat due to surrounding gradient. Moreover, High temperature values generally where chip load is relatively high compared to neighbouring segments.

Temperature gradient fluctuations were observed in chip temperature distributions for all cases. It was experimented that using lower convergence criteria (below seven percent) can solve this behaviour.

Chapter 6: Conclusion & Future Work

The aim of this thesis was the development of a novel temperature prediction model that is applicable to oblique cutting processes in variable cutting conditions. Temperature prediction is still one of the most complex problems in machining research community. High strain rates, temperatures, complex tool-workpiece and tool-chip contact bring lots of difficulties in terms of predictive modelling. Therefore, predicting cutting temperatures is still a big challenge.

Developed model uses orthogonal to oblique transformation in order to calculate mechanical and geometrical inputs to thermal solution procedure. Then, tool, chip and workpiece temperatures are calculated. Since shear plane heat generation input was not included in the analysis, workpiece temperature calculations were only done for demonstration purpose with simplified geometry for two cases. Secondary zone heat source was modelled as uniform intensity heat source over the contact area. As expressed before, elliptic structural grid generation method was used in the analysis without using forcing functions. Simulation results showed that average temperatures on rake face are in good agreement with experimental results. Proposed solution method can be utilized in selecting optimum processing parameters, tool geometry and tool material in order to avoid excessive tool temperatures.

Proposed methodology is flexible compared to available machining temperature models in literature. Representing different oblique cutting geometries is straightforward using this approach. In developed model, finite difference method is selected in order to solve heat transfer problem. Since resulting equation system is algebraic and does not require additional numerical calculations, finite difference method is computationally less intensive compared to finite element method for current problem. In addition, defining deformation behaviour of material and frictional behaviour at tool-chip interface are still problematic in finite element method based approaches.

Since, proposed approach is based on oblique cutting geometry, it can be extended to other oblique cutting processes like face milling. Nowadays, usage of coated tools is widespread. Therefore, prediction method should be extended to coated tools. Rubbing is another important heat source and affects workpiece temperatures substantially. As a result, wear land heat sources can be included in the analysis in the future. In developed model, surfaces open to environment assumed as adiabatic; hence, predicted temperatures are a little bit higher compared to experimental measurements. Addition of convection heat losses to the model will result in more accurate predictions. In addition, temperature dependency of the thermal properties of the tool and workpiece materials can be added to analyses.

Mesh generation is another vital part that affects numerical solution accuracy. Therefore, application of different mesh generation strategies can be beneficial. In this work, a structured mesh generation scheme is applied. However, current mesh generation scheme can be improved by using forcing functions or trying different kinds of structured grid generation methods. Moreover, a model that uses unstructured mesh generation procedure can be developed in order to represent cutting geometry more precisely.

Workpiece temperature gradient affects part surface integrity; for this reason, accurate modelling of workpiece temperature distributions is very important. As stated previously, workpiece temperature prediction was presented only for demonstration purpose. Shear plane heat generation should be added to model (as internal volumetric heat generation) in order to make more accurate predictions on workpiece side.

Development of an in house experiment set up can be beneficial in order to further validate and improve the model. Since it can give more flexibility, a radiation thermometry based measurement technique can be a suitable choice for that setup.

Bibliography

[1] C.E. Leshock, Y.C. Shin, Investigation on Cutting Temperature in Turning by a Tool-Work Thermocouple Technique, Journal of Manufacturing Science and Engineering, 119 (1997) 502-508.
[2] I. Lazoglu, Y. Altintas, Prediction of tool and chip temperature in continuous and interrupted machining, International Journal of Machine Tools and Manufacture, 42 (2002) 1011-1022.
[3] F.W. Taylor, On the art of cutting metals, Transactions of ASME, 28 (1907) 31-248.
[4] K. Trigger, B. Chao, An Analytical Evaluation of Metal Cutting Temperature, Transactions of ASME, 73 (1951) 57-68.
[5] B. Chao, K. Trigger, The Significance of Thermal Number in Metal Machining, Transactions of ASME, 75 (1953) 109-120.
[6] E.G. Loewen, M.C. Shaw, On the Analysis of Cutting Tool Temperatures, Transactions of ASME, 76 (1954) 217-231.
[7] J.H. Weiner, Shear Plane Temperature Distribution in Orthogonal Cutting, Transactions of ASME, 76 (1954) 1331-1341.
[8] P.K. Venuvinod, W.S. Lau, Estimation of rake temperatures in free oblique cutting, International Journal of Machine Tool Design and Research, 26 (1986) 1-14.
[9] H. Blok, Theoretical study of temperature rise at surfaces of actual contact under oiliness lubricating conditions, Proceedings of the General Discussion on Lubrication and Lubricants, 2 (1937) 222–235.
[10] E.M. Berliner, V.P. Krainov, Analytic calculations of the temperature field and heat flows on the tool surface in metal cutting due to sliding friction, Wear, 143 (1991) 379-395.
[11] D.A. Stephenson, A. Ali, Tool temperatures in interrupted metal cutting, Journal of engineering for industry, 114 (1992) 127-136.
[12] H.T. Young, T.L. Chou, Modelling of tool/chip interface temperature distribution in metal cutting, International Journal of Mechanical Sciences, 36 (1994) 931-943.
[13] R. Radulescu, S.G. Kapoor, An Analytical Model for Prediction of Tool Temperature Fields during Continuous and Interrupted Cutting, Journal of Engineering for Industry, 116 (1994) 135-143.
[14] D.A. Stephenson, T.C. Jen, A.S. Lavine, Cutting Tool Temperatures in Contour Turning: Transient Analysis and Experimental Verification, Journal of Manufacturing Science and Engineering, 119 (1997) 494-501.
[15] T.-C. Jen, A.U. Anagonye, An Improved Transient Model of Tool Temperatures in Metal Cutting, Journal of Manufacturing Science and Engineering, 123 (2001) 30-37.
[16] V. Ostafiev, A. Kharkevich, K. Weinert, S. Ostafiev, Tool Heat Transfer in Orthogonal Metal Cutting, Journal of Manufacturing Science and Engineering, 121 (1999) 541-549.
[17] R. Komanduri, Z.B. Hou, Thermal modeling of the metal cutting process Part I : Temperature rise distribution due to shear plane heat source, International Journal of Mechanical Sciences, 42 (2000) 1715-1752.
[18] R. Komanduri, Z.B. Hou, Thermal modeling of the metal cutting process Part II: temperature rise distribution due to frictional heat source at the tool–chip interface, International Journal of Mechanical Sciences, 43 (2001) 57-88.

[19] R. Komanduri, Z.B. Hou, Thermal modeling of the metal cutting process Part III: temperature rise distribution due to the combined effects of shear plane heat source and the tool–chip interface frictional heat source, International Journal of Mechanical Sciences, 43 (2001) 89-107.
[20] Y.K. Chou, H. Song, Thermal modeling for white layer predictions in finish hard turning, International Journal of Machine Tools and Manufacture, 45 (2005) 481-495.
[21] Y. Huang, S.Y. Liang, Modelling of the cutting temperature distribution under the tool flank wear effect, Proceedings of the Institution of Mechanical Engineers, Part C: Journal of Mechanical Engineering Science, 217 (2003) 1195-1208.
[22] K.-M. Li, S.Y. Liang, Modeling of Cutting Temperature in Near Dry Machining, Journal of Manufacturing Science and Engineering, 128 (2006) 416-424.
[23] D.J. Richardson, M.A. Keavey, F. Dailami, Modelling of cutting induced workpiece temperatures for dry milling, International Journal of Machine Tools and Manufacture, 46 (2006) 1139-1145.
[24] A.C. Rapier, A theoretical investigation of the temperature distribution in the metal cutting process, British Journal of Applied Physics, 5 (1954) 400-405.
[25] R.P. Dutt, R.C. Brewer, On The Theoretical Determination of The Temperature Field in Orthogonal Machining, International Journal of Production Research, 4 (1965) 91 - 114.
[26] E.K. Levy, C.L. Tsai, M.P. Groover, Analytical Investigation of the Effect of Tool Wear on the Temperature Variations in a Metal Cutting Tool, Journal of Engineering for Industry, 98 (1976) 251-257.
[27] J.F.W. Bishop, An Approximate Method for Determining The Temperatures Reached in Steady Motion Problems of Plane Plastic Strain, The Quarterly Journal of Mechanics and Applied Mathematics, 9 (1956) 236-246.
[28] E. Usui, T. Shirakashi, T. Kitagawa, Analytical prediction of three dimensional cutting process, part 3: cutting temperature and crater wear of carbide tool, Journal of Engineering for Industry, 100 (1978) 236-243.
[29] A. Smith, E. Armarego, Temperature Prediction in Orthogonal Cutting with a Finite Difference Approach, CIRP Annals - Manufacturing Technology, 30 (1981) 9-13.
[30] B. Chao, K. Trigger, Temperature distribution at the tool chip interface in metal cutting, Transactions of ASME, 77 (1955) 1107-1121.
[31] P.L.B. Oxley, The mechanics of machining : an analytical approach to assessing machinability, E. Horwood ; Halsted Press, 1989.
[32] D. Ulutan, I. Lazoglu, C. Dinc, Three-dimensional temperature predictions in machining processes using finite difference method, Journal of Materials Processing Technology, 209 (2009) 1111-1121.
[33] W. Grzesik, Finite difference analysis of the thermal behaviour of coated tools in orthogonal cutting of steels, International Journal of Machine Tools and Manufacture, 44 (2004) 1451-1462.
[34] A.O. Tay, M.G. Stevenson, G.D.V. Davis, Using the finite element method to determine temperature distributions in orthogonal machining, ARCHIVE: Proceedings of the Institution of Mechanical Engineers 1847-1982 (vols 1-196), 188 (1974) 627-638.
[35] M.G. Stevenson, P.L.B. Oxley, An experimental investigation of the influence of strain-rate and temperature on the flow stress properties of a low carbon steel using a machining test, ARCHIVE: Proceedings of the Institution of Mechanical Engineers 1847-1982 (vols 1-196), 185 (1970) 741-754.

[36] A.O. Tay, M.G. Stevenson, G. de Vahl Davis, P.L.B. Oxley, A numerical method for calculating temperature distributions in machining, from force and shear angle measurements, International Journal of Machine Tool Design and Research, 16 (1976) 335-349.
[37] P.D. Muraka, G. Barrow, S. Hinduja, Influence of the process variables on the temperature distribution in orthogonal machining using the finite element method, International Journal of Mechanical Sciences, 21 (1979) 445-456.
[38] M.G. Stevenson, P.K. Wright, J.G. Chow, Further Developments in Applying the Finite Element Method to the Calculation of Temperature Distributions in Machining and Comparisons With Experiment, Journal of Engineering for Industry, 105 (1983) 149-154.
[39] P.R. Dawson, S. Malkin, Inclined Moving Heat Source Model for Calculating Metal Cutting Temperatures, Journal of Engineering for Industry, 106 (1984) 179-186.
[40] J.S. Strenkowski, K.-J. Moon, Finite Element Prediction of Chip Geometry and Tool/Workpiece Temperature Distributions in Orthogonal Metal Cutting, Journal of Engineering for Industry, 112 (1990) 313-318.
[41] Z.C. Lin, S.Y. Lin, A Coupled Finite Element Model of Thermo-Elastic-Plastic Large Deformation for Orthogonal Cutting, Journal of Engineering Materials and Technology, 114 (1992) 218-226.
[42] A.J. Shih, Finite Element Simulation of Orthogonal Metal Cutting, Journal of Engineering for Industry, 117 (1995) 84-93.
[43] J.-S. Wu, O.W. Dillon, W.-Y. Lu, Thermo-Viscoplastic Modeling of Machining Process Using a Mixed Finite Element Method, Journal of Manufacturing Science and Engineering, 118 (1996) 470-482.
[44] E. Ng, D.K. Aspinwall, D. Brazil, J. Monaghan, Modelling of temperature and forces when orthogonally machining hardened steel, International Journal of Machine Tools and Manufacture, 39 (1999) 885-903.
[45] E. Ceretti, P. Fallböhmer, W.T. Wu, T. Altan, Application of 2D FEM to chip formation in orthogonal cutting, Journal of Materials Processing Technology, 59 (1996) 169-180.
[46] T. Özel, T. Altan, Process simulation using finite element method — prediction of cutting forces, tool stresses and temperatures in high-speed flat end milling, International Journal of Machine Tools and Manufacture, 40 (2000) 713-738.
[47] G.M. Pittalà, M. Monno, A new approach to the prediction of temperature of the workpiece of face milling operations of Ti-6Al-4V, Applied Thermal Engineering, 31 (2011) 173-180.
[48] A. Moufki, Thermoviscoplastic modelling of oblique cutting: forces and chip flow predictions, International Journal of Mechanical Sciences, 42 (2000) 1205-1232.
[49] V.R. Marinov, Hybrid analytical-numerical solution for the shear angle in orthogonal metal cutting -- Part I: theoretical foundation, International Journal of Mechanical Sciences, 43 (2001) 399-414.
[50] A. Moufki, A. Devillez, D. Dudzinski, A. Molinari, Thermomechanical modelling of oblique cutting and experimental validation, International Journal of Machine Tools and Manufacture, 44 (2004) 971-989.
[51] E. Shamoto, Y. Altintas, Prediction of Shear Angle in Oblique Cutting with Maximum Shear Stress and Minimum Energy Principles, Journal of Manufacturing Science and Engineering, 121 (1999) 399-407.
[52] G.V. Stabler, The fundamental geometry of cutting tools, ARCHIVE: Proceedings of the Institution of Mechanical Engineers 1847-1982 (vols 1-196), 165 (1951) 14-26.
[53] R.H. Brown, E.J.A. Armarego, Oblique machining with a single cutting edge, International Journal of Machine Tool Design and Research, 4 (1964) 9-25.

[54] M. Kaymakci, Generalized Modeling of Metal Cutting Mechanics, in: Mechanical Engineering, University of British Columbia, Vancouver, 2009, pp. 137.
[55] A. Molinari, A. Moufki, A new thermomechanical model of cutting applied to turning operations. Part I. Theory, International Journal of Machine Tools and Manufacture, 45 (2005) 166-180.
[56] K.A. Hoffmann, S.T. Chiang, Computational Fluid Dynamics, Engineering Education System, 2000.
[57] V.D. Liseikin, Grid Generation Methods, 2 ed., Springer, 2010.
[58] J.E. Thompson, Z.U.A. Warsi, C.W. Mastin, Numerical Grid Generation Foundations and Applications, Elsevier Science Publishing 1985.
[59] J. Tannehill, D. Anderson, R. Pletcher, Computational Fluid Mechanics and Heat Transfer, Taylor & Francis, 1997.
[60] D.A. Stephenson, Tool-Work Thermocouple Temperature Measurements---Theory and Implementation Issues, Journal of Engineering for Industry, 115 (1993) 432-437.
[61] C. Bus, N.A.L. Touwen, P.C. Veenstra, A.C.H. Van Der Wolf, Thermoelectric characteristics of carbides, in: MTDR, machine tool design and research: 12th international conference, Manchester, September 1971/Ed. F. Koeningsberger, Pergamon, 1971, pp. 397-400.
[62] M. Nasr, E.G. Ng, M. Elbestawi, Effects of workpiece thermal properties on machining-induced residual stresses - thermal softening and conductivity, Proceedings of the Institution of Mechanical Engineers, Part B: Journal of Engineering Manufacture, 221 (2007) 1387-1400.

Vita

Coşkun İslam was born in December 1986, in Istanbul. He graduated from Kabataş Erkek Lisesi (high school) in 2004. Then, He received Bachelor of Science in Manufacturing Engineering from Istanbul Technical University in 2008 (ranked 2nd of his class in the Manufacturing Engineering Department). Since 2008, He has been going on his studies under M.Sc. in Mechanical Engineering program at Koç University as a research and teaching assistant. He is holder of The Scientific and Technological Research Council of Turkey (TUBITAK) scholarship for his M.Sc. studies. Coşkun İslam is co-author of one international journal article and one conference paper.